Powerline Communication in Automotive Battery Management Systems: Channel Characterization and Physical Layer Performance

Zur Erlangung des akademischen Grades einer

DOKTORIN DER INGENIEURWISSENSCHAFTEN
(Dr.-Ing.)

von der KIT-Fakultät für
Elektrotechnik und Informationstechnik
des Karlsruher Instituts für Technologie (KIT)

angenommene

DISSERTATION

von

Dipl.-Ing. (Univ.) Ichraf Ouannes

Tag der mündlichen Prüfung: 01.02.2022
Hauptreferent: Prof. Dr.-Ing. habil. Klaus Dostert
Korreferent: Prof. Dr.-Ing. Martin Doppelbauer

Zusammenfassung

Diese Arbeit ist im Rahmen vom öffentlich geförderten Projekt IntLiIon [1] entstanden. Die Förderung durch das deutsche Bundesministerium für Bildung und Forschung (BMBF) ist Teil der Maßnahme *Energieeffiziente und sichere Elektromobilität (STROM 2)* im Programm *IKT 2020 – Forschung für Innovation*, mit dem Ziel, Qualitätseigenschaften zukünftiger Elektrofahrzeuge wie Reichweite, Komfort, Leistungsvermögen und Sicherheit zu optimieren.

Die Dissertation untersucht die Eignung der Powerline Kommunikation für den Einsatz in Batteriemanagementsystemen von Elektro- und Hybridfahrzeugen mit dem Fokus auf der Master-Slave Architektur. Gegenüber herkömmlichen Lösungen hat die Powerline Kommunikation einen signifikanten Kostenvorteil, dadurch dass die dedizierte Busverkabelung durch die ganze Batterie insbesondere mit ihren teuren fahrzeugtauglichen Steckern komplett entfallen kann. Das erarbeitete Kommunikationskonzept beruht darauf, dass die Batteriezellen einzeln überwacht und angesteuert werden. Die Zellüberwachungsknoten werden deshalb an die Pole der Batteriezellen angeschlossen. Zelldaten wie Spannung, Temperatur und Druck werden über die Stromleitungen an das zentrale Batteriesteuergerät übertragen. Die Dezentralisierung der Datenerfassungsknoten bis hinunter auf Zellebene ermöglicht die Steigerung der Messgenauigkeit für eine Vielzahl kritischer Messgrößen und deshalb auch eine Erhöhung der Sicherheit bei gleichzeitiger Steigerung der Batterieenergiedichte. Darüber hinaus kann eine höhere Reichweite durch ein intelligentes Management der begrenzten elektrischen Energie erreicht werden.

Im Rahmen der Dissertation wurden grundlegende Untersuchungen zur technischen Machbarkeit und der Realisierung vom Kommunikationssystem durch-

[1] Intelligente Datenbuskonzepte für Lithium-Ionen Batterien in Elektro- und Hybridfahrzeugen

geführt. Im Mittelpunkt der Untersuchungen stehen die Kanaleigenschaften im Frequenzbereich von 1 MHz bis 100 MHz und die Eignung von herkömmlichen Übertragungstechniken und Algorithmen des Physical Layer für eine robuste Datenübertragung mit Datenraten weit über 1 Mbit/s.

Die mindesterforderliche Datenrate hängt vom Kanalzugriffsverfahren ab und lässt sich in Abhängigkeit von der Anzahl der Batteriezellen, der Datenmenge pro Zelle und der Datenerfassungsrate ermitteln. Zwecks der Kanalcharakterisierung wurden in einem ersten Schritt die elektrischen Eigenschaften von Batteriezellen im Hochfrequenzbereich gemessen. Daraufhin wurde ein Modell für einzelne Batteriezellen basierend auf RLC-Schaltungen und semiempirischer Parameterermittlung erstellt. In einem Folgeschritt wurden die Übertragungseigenschaften vom Kanal anhand einer Batterie mit insgesamt 96 in Reihe geschalteten Zellen messtechnisch ermittelt, charakteristische Kanalgrößen wie das Signal-Rausch-Verhältnis und die Kanallaufzeit abgeleitet und ein Kanalmodell für die Physical Layer Simulationen festgelegt. Zur Bewertung der Eignung der ausgewählten Übertragungstechniken wurde die Bitfehlerrate verwendet. Einzel- und Mehrträgermodulationsverfahren, lineare und nicht lineare Kanalentzerrungsalgorithmen sowie Block- und Faltungscodes wurden im Hinblick auf Komplexität und Robustheit bewertet. Die Ergebnisse zeigen, dass sich Einzelträgermodulationsverfahren kombiniert mit nichtlinearer Kanalentzerrung und Blockkodierung für eine robuste Datenübertragung am besten eignen.

Acknowledgement

The dissertation at hand evolved from my research activities at Robert Bosch GmbH in Renningen. I would like to express my deepest appreciation to Prof. Dr.-Ing. habil. Klaus Dostert, from the Institute of Industrial Information Technology (IIIT) at the Karlsruhe Institute of Technology (KIT), for giving me the opportunity to work under his supervision. I also had the pleasure to work with Dr.-Ing. Patrick Nickel and I gratefully acknowledge his valuable assistance. Special thanks go also to Prof. Dr.-Ing. Martin Doppelbauer for his genuine interest in this thesis and for agreeing to act as second examiner. Finally, I would like to extend my deepest gratitude to my family and closest friends for their encouragement and moral support.

Contents

Abbreviations

AC	**a**lternating **c**urrent
ACF	**a**uto**c**orrelation **f**unction
ADC	**a**nalog-to-**d**igital **c**onverter
AFE	**a**nalog **f**ront-**e**nd
ASK	**a**mplitude **s**hift **k**eying
AWGN	**a**dditive **w**hite **G**aussian **n**oise
BCH	**B**ose-**C**haudhuri-**H**ocquenghem
BCJR	**B**ahl-**C**ocke-**J**elinek-**R**aviv
BDU	**b**attery **d**isconnect **u**nit
BER	**b**it **e**rror **r**ate
BPSK	**b**inary **p**hase **s**hift **k**eying
BMS	**b**attery **m**anagement **s**ystem
CAN	**c**ontroller **a**rea **n**etwork
CC	**c**ommunication **c**ontroller
CDMA	**c**ode **d**ivision **m**ultiple **a**ccess
CFR	**c**hannel **f**requency **r**esponse
CID	**c**ircuit **i**nterrupt **d**evice
CIR	**c**hannel **i**mpulse **r**esponse
CMU	**c**ell **m**onitoring **u**nit
CP	**c**yclic **p**refix

CPFSK	**c**ontinuous **p**hase **f**requency **s**hift **k**eying
CSC	**c**ell **s**upervision **c**ircuit
DFE	**d**ecision **f**eedback **e**qualization
DMC	**d**iscrete **m**emoryless **c**hannel
DPSK	**d**ifferential **p**hase **s**hift **k**eying
DC	**d**irect **c**urrent
DUT	**d**evice **u**nder **t**est
DSSS	**d**irect **s**equence **s**pread **s**pectrum
EV	**e**lectric **v**ehicle
FDD	**f**requency **d**ivision **d**uplexing
FDMA	**f**requency **d**ivision **m**ultiple **a**ccess
FEM	**f**inite **e**lement **m**ethod
FHSS	**f**requency **h**opping **s**pread **s**pectrum
FIR	**f**inite **i**mpulse **r**esponse
FLOP	**f**loating-**p**oint **o**peration
FMT	**f**iltered **m**ultitone
FSK	**f**requency **s**hift **k**eying
GMSK	**G**aussian **m**inimum **s**hift **k**eying
HF	**h**igh **f**requency
HV	**h**igh **v**oltage
HEV	**h**ybrid **e**lectric **v**ehicle
HMM	**h**idden **M**arkov **m**odel
ICI	**i**nter**c**arrier **i**nterference
i.i.d.	**i**ndependent and **i**dentically **d**istributed
IFT	**i**nverse **F**ourier **t**ransform

ISI	**i**nter**s**ymbol **i**nterference
LE	**l**inear **e**qualization
LMS	**l**east **m**ean **s**quares
LSE	**l**east **s**quares **e**stimation
LTI	**l**inear **t**ime-**i**nvariant
MAC	**m**edia **a**ccess **c**ontrol
MF	**m**atched **f**ilter
ML	**m**aximum **l**ikelihood
MLSE	**m**aximum **l**ikelihood **s**equence **e**stimation
MSE	**m**ean **s**quare **e**rror
MSK	**m**inimum **s**hift **k**eying
MMSE	**m**inimum **m**ean **s**quare **e**rror
MMU	**m**odule **m**anagement **u**nit
OCV	**o**pen **c**ircuit **v**oltage
OFDM	**o**rthogonal **f**requency **d**ivision **m**ultiplexing
OQAM	**o**ffset **q**uadrature **a**mplitude **m**odulation
OQPSK	**o**ffset **q**uadrature **p**hase **s**hift **k**eying
OSI	**o**pen **s**ystem **i**nterconnection
PAM	**p**ulse **a**mplitude **m**odulation
PAPR	**p**eak-to-**a**verage **p**ower **r**atio
PHEV	**p**lug-in **h**ybrid **e**lectric **v**ehicle
PLC	**p**ower**l**ine **c**ommunication
PMU	**p**ack **m**anagement **u**nit
PRIME	**p**owerline **i**ntelligent **m**etering **e**volution
PSD	**p**ower **s**pectral **d**ensity

PSK	**p**hase **s**hift **k**eying
PTC	**p**ositive **t**emperature **c**oefficient
QAM	**q**uadrature **a**mplitude **m**odulation
QPSK	**q**uadrature **p**hase **s**hift **k**eying
RF	**r**adio **f**requency
RMS	**r**oot **m**ean **s**quare
RC	**r**aised-**c**osine
RRC	**r**oot-**r**aised-**c**osine
RS	**R**eed-**S**olomon
RLS	**r**ecursive **l**east **s**quares
SC-FDE	**s**ingle-**c**arrier **f**requency **d**omain **e**qualization
SDR	**s**oftware-**d**efined **r**adio
SINR	**s**ignal-to-**i**nterference-plus-**n**oise **r**atio
SIR	**s**ignal-to-**i**nterference **r**atio
SoC	**s**tate-**o**f-**c**harge
SoH	**s**tate-**o**f-**h**ealth
SNR	**s**ignal-to-**n**oise **r**atio
SPI	**s**erial **p**eripheral **i**nterface
TDD	**t**ime **d**ivision **d**uplexing
TDMA	**t**ime **d**ivision **m**ultiple **a**ccess
VCU	**v**ehicle **c**ontrol **u**nit
VIA	**v**ector **i**mpedance **a**nalyzer
VNA	**v**ector **n**etwork **a**nalyzer
WMF	**w**hitened **m**atched **f**ilter

Chapter 1

Introduction

1.1 Motivation

Electric vehicles (EVs) are a cornerstone of sustainable mobility. The development of EVs strongly depends on the available battery technologies. Despite the significant technological progress, it is still a challenge for battery manufacturers to come up with a technology that satisfies all the demands of electric car makers. Traction batteries have to meet high safety and reliability standards. At the same time, they need to have a long durability in addition to a high energy density in order for the EVs to be economically viable and have a high driving range.

With the help of condition monitoring, battery management systems (BMSs) can ensure a safe and reliable operation of the battery. BMSs with a master-slave architecture are widely used in automotive applications. Such BMSs have a central battery pack management unit (PMU) and multiple module management units (MMUs). A battery module consists of multiple cells connected in series, parallel or series-parallel. The controller area network (CAN) is the bus system typically used for the communication between the MMUs and the PMU. Thus, a maximum data rate of 1 Mbit/s is possible. The MMU is primarily responsible for data acquisition. It measures the module temperature at different cold and hot spots. In addition, it measures the voltage and the pressure of every cell in the module. The MMUs can be connected in parallel to the PMU or they can be daisy-chained to each other and back to the PMU. In either case, a relatively high amount of data cables and connectors is

required.

Lithium-ion traction batteries have a relatively high energy density and allow enhancing the driving range of EVs, compared to other battery technologies. Hence, they are very much in demand on the EV market. Nevertheless, the trend goes towards higher energy densities. An increase in the energy density usually comes at the cost of an increased computational complexity. The computational overhead, which is required to ensure a safe operation of the battery, depends on the number of battery cells and the update rates of the cell data measurements. Furthermore, any loss of data accuracy adversely affects the battery longevity and performance. Thus, accurate measurements are very important in order to take advantage of the maximum battery capacity. As a result, in the case of large traction batteries, a large amount of highly accurate cell data needs to be transferred from the MMUs to the PMU, which makes a high-speed communication indispensable for automotive BMSs.

The need for a high-speed communication justifies the expected increase in the data rates. In order to be well-prepared for the upcoming challenges, new communication approaches need to be investigated. This work is conducted within the framework of the project IntLiIon[2] aiming to improve performance, safety and service life of electric and hybrid vehicles using smart battery management. The project initiated the idea of using the powerlines of the battery to exchange measurement data and control signals between the central battery control unit and the other BMS supervision and control units. The primary benefit of powerline communication (PLC) is the ability to use the existing infrastructure, thus saving space, weight and cost. This work is conducted to investigate the potential of PLC to be used in BMSs of lithium-ion traction batteries. By constantly monitoring each battery cell and controlling it individually, an optimum use of the battery's energy is expected. Since the focus is on high data rates, only the high frequency (HF) transfer properties of the battery powerlines are relevant for our work. More specifically, we choose the frequency range 1 MHz to 100 MHz to perform the measurements required

[2]Intelligent data bus concepts for lithium-ion batteries in electric and hybrid vehicles. Funded by Germany's Federal Ministry of Education and Research as part of the *Energy-efficient and safe Electromobility* initiative (STROM 2) within the funding program *ICT 2020 - Research for Innovation.*

for the characterization of the physical medium.

Automotive battery systems are usually customized to suit the needs of each electric car manufacturer. Therefore, the structural, mechanical and electrical design may differ from one battery system to another. For instance, modules can be stacked on top of each other or placed side by side. The battery cells of different battery systems may have different sizes and formats. Furthermore, the wiring concept may also be different. All these aspects should be considered when investigating the HF transfer characteristics of the battery powerlines.

Three-dimensional (3D) battery models and finite element method (FEM)-based simulations allow to better understand the physical medium transfer characteristics in case battery systems with different designs need to be considered. The accuracy of the simulation results depends on how accurate the 3D models are. This study does not deal with 3D modeling of battery systems. Instead, the physical medium characterization is performed using measurements.

1.2 Related work and contribution

Electrochemical modeling of lithium-ion traction batteries has been the subject of a lot of scientific publications and review articles. It is shown in [1] that advanced modeling and estimation techniques allow for an accurate range forecasting. In particular, the study reviews and discusses various battery modeling approaches including mathematical models, electrochemical models and electrical equivalent circuit models. In [2], the authors classify the electrochemical battery models into physical, empirical and abstract models and compare them with respect to accuracy and complexity. Furthermore, equivalent circuit models are represented and explained. Most, if not all, of the battery models described in the literature deal with the electrochemical behavior of battery cells at frequencies far below 1 MHz. Therefore, they are not of much use in the HF range, which is the frequency range of interest for our work.

In [3], the authors propose to use wireless sensors in order to monitor the battery cells individually by measuring the voltage and the temperature. The sensors are primarily developed for lead acid batteries and are intended to be

used in lithium-based traction batteries in the future. In [4], different types of antennas are used to conduct wireless channel measurements in different frequency ranges with the help of a simplified experimental setup. In [5], the authors investigate the wireless channel variations as a function of the position and the number of antennas. They also provide an analysis of the physical layer performance using quadrature phase shift keying (QPSK) modulation with data rates up to 2 Mbit/s. In [6], an enhanced testbed with planar inverted F-antennas is used for the channel measurements. Measurement and simulation results are presented and discussed. In a follow-up study, the authors discuss the implementation of the physical and media access control (MAC) layers of the wireless BMS using software-defined radio (SDR) platforms [7].
Another innovative wireless BMS based on a proprietary communication protocol called Wireless Battery Area Network protocol is introduced in [8]. The proposed wireless BMS uses a master module to collect and process data in addition to the many energy-autonomous micro-sensors mounted on the battery cells. Star topologies with up to a few thousands of sensors per master module are supported. The protocol defines the syntax, semantics and synchronization of the messages between the sensors and the master module.

In [9], the authors describe how to reduce the design effort related to BMSs by integrating monitoring circuits inside the battery cells. A contactless capacitive coupling mechanism is proposed and the robustness of the data transmission is investigated by means of simulations and experiments using battery systems with up to 100 smart battery cells. Frequency shift keying (FSK) modulation is used and the experimental results obtained with a prototypical implementation are presented, where data rates up to 500 kbit/s are supported.

As part of the project IntLiIon, the authors in [10] introduce an AC-signal coupling technique based on the rogowski-coil to be used for PLC in lithium-ion BMSs. Measurements are performed to characterize the transfer properties of the rogowski-coil for frequencies up to 600 MHz. In-vehicle noise measurements are conducted in the frequency range 1 MHz to 100 MHz. A performance comparison between orthogonal frequency division multiplexing (OFDM) and single-carrier frequency domain equalization (SC-FDE) is also included for carrier frequencies around 400 MHz and data rates up to 2 Mbit/s. The results show that SC-FDE is better suited for PLC than OFDM.

In this thesis, we focus on BMSs with a master-slave architecture. We assume that each battery cell is monitored and controlled individually, i.e. instead of using MMUs, each battery cell is supposed to have its own cell monitoring unit (CMU). The latter measures the cell voltage, temperature and pressure. We assume that the CMUs are connected in series to each other and to the PMU. Furthermore, we consider the frequency range 1 MHz to 100 MHz and address topics which have not yet been dealt with in the literature, such as

- characterizing the radio frequency (RF) properties of prismatic lithium-ion battery cells with a capacity of up to 60 Ah,
- modeling the battery cells in the HF range using lumped circuits and semi-empirical data fitting,
- characterizing the PLC channel in both time and frequency domains, based on real world channel measurements,
- modeling the PLC channel and analyzing the channel frequency selectivity, using the root mean square (RMS) delay spread,
- calculating the minimum required data rate, assuming a time division multiple access (TDMA)-based MAC protocol with time division duplexing (TDD) for the uplink (from the CMUs to the PMU) and downlink (from the PMU to the CMUs) data transmission,
- estimating the modulation-constrained channel capacity in addition to the required minimum signal-to-noise ratio (SNR),
- implementing the physical layer using single- and multi-carrier modulation, channel equalization and channel coding,
- and analyzing the bit error rate (BER) performance with symbol rates up to 20 MBaud.

1.3 Thesis outline

The rest of the dissertation is organized as follows. Chapter 2 is dedicated to the fundamentals. Section 2.1 addresses the lithium-ion battery technology.

It introduces the standard battery cell formats, illustrates how battery cells, modules and packs are designed and shows which saftey components are typically used at the cell level. Section 2.2 describes the common topologies of state-of-the-art BMSs. It also discusses some important aspects with regard to cell data acquisition and briefly presents some of the prevailing communication solutions for automotive BMSs. Section 2.3 deals with the PLC applications. It contains a short summary of the existing standards including the allocated frequency bands and the digital modulation schemes of the physical layer. It also discusses the in-vehicle PLC, which has not yet been adopted as a standard communication technology for automotive applications. Section 2.4 deals with single-carrier communication systems and focuses on digital modulation schemes and channel equalization. Finally, in Section 2.5, we talk about the MAC protocol and introduce some of the common multiple access schemes.
Chapter 3 is dedicated to the use of PLC in BMSs, where the focus is on master-slave architectures and individual monitoring of battery cells. Section 3.1 describes the system-related assumptions based on which this work is conducted. We show that TDMA/TDD can be used as a media access scheme for the PLC MAC protocol and calculate the required data rate as a function of the cell data update rate and the number of battery cells. Section 3.2 deals with the characterization of the RF properties of 40 Ah and 60 Ah lithium-ion battery cells. It briefly introduces some of the impedance measurement methods and shows that the auto-balancing bridge method is best suited for our application due to its high accuracy in the frequency range 1 MHz to 100 MHz. We disassemble dummy battery cells and measure the impedance of the individual components. Furthermore, we measure the impedance of single battery cells and that of multiple cells connected in series. We create lumped circuit models of the battery cells based on semi-empirical data fitting and show that modeling large battery packs in the HF range is quite challenging. Section 3.3 deals with the channel measurements. In the HF range, the channel transfer properties can be best characterized using the scattering parameters (S-parameters). The noise is measured and modeled in the time-domain, where different driving scenarios are considered. The PLC channel model is presented in Section 3.4. First, we derive the channel frequency response (CFR) from the measured S-parameters. We then use the obtained CFR to determine

the symbol rate-sampled equivalent baseband channel model. In addition, we analyze the frequency selectivity as a function of the allocated channel bandwidth and the carrier frequency by calculating the RMS delay spread. Section 3.5 is dedicated to the performance analysis of the physical layer. It includes numerically calculated results of the modulation-constrained channel capacity and the required minimum SNR. We compare the BER performance and the complexity of different physical layer implementations with data rates up to 20 Mbit/s using single-carrier modulation schemes, channel equalization and channel coding. We also compare the BER performance of single- and multi-carrier modulation using the example of OFDM and show that single-carrier modulation schemes outperform coded-OFDM within the limits of reasonable technical complexity.

Finally, the dissertation is concluded with a summary and an outlook.

Chapter 2

Fundamentals

2.1 Lithium-based battery technology

Lithium-ion batteries are widely used in EVs. They provide high voltage and their energy density is much higher than that of other battery technologies. They also have a lower self-discharge-rate and a good cycle performance. Lithium-ion battery cells typically operate between 3.2 V and 3.8 V (nominal voltage). The cell/battery capacity, measured in Ah, represents the amount of energy that can be stored, while the energy density is the energy given in kWh per unit mass or volume. High-energy batteries have an energy content ranging from 7.5 kWh to 80 kWh or even greater for very large applications. Safety components such as safety disconnect, high-voltage interlock loop system and orange cabling are used in large battery systems [11].

2.1.1 Standard cell formats

Lithium-ion battery cells are available in three basic formats: cylindrical, prismatic and pouch. Cylindrical cells are primarily used in hybrid electric vehicles (HEVs). They are known for structural stability and ease of manufacturing. They have a metal or a hard plastic cylindrical case and can withstand high internal pressure without deformation. Even though they do not make optimal use of the space in the case of side-by-side placement, they still have a higher energy density than prismatic or pouch cells. This compensates for the low packaging density. Besides, empty spaces can be used for cooling in order to improve the thermal management. A 18650 cell (18 mm diameter by

	PHEV1	**PHEV2**	**PHEV2+**	**EV1**	**EV2**	**HEV**
L (mm)	173	148	148	173	173	120
H (mm)	85	91	125	115	115	85
T (mm)	21	26.5	26.5	32	45	12.5

Table 2.1: VDA size standards of prismatic cells (L: length, H: height, T: thickness)

65 mm in length) has a capacity between 3.1 Ah and 3.9 Ah. The larger 26650 cell (26 mm in diameter) is less popular and is said to be harder to build due to its thickness [11].

Most plug-in hybrid electric vehicles (PHEVs) and EVs use large prismatic cells instead of cylindrical ones in order to reduce the total number of cells for the same voltage and energy requirements [11]. A reduced number of cells results in a simple system design and a higher mechanical and electrical reliability of the overall assembly. Table 2.1 shows the first set of standards around prismatic cell sizing as specified by the German association of the automotive industry (VDA)[3]. Six standard cell formats used for HEVs, PHEVs and EVs are mentioned[4]. Detailed information on the capacity and energy densities can be found in Table 2.2. Pouch cells have the highest packaging density among all cell formats. They are enclosed in a soft lightweight bag and are easily stackable. Nevertheless, provision must be made for swelling, especially in case of small cells.

2.1.2 Battery cell design

The battery cell is the smallest unit in a battery pack. A prismatic cell has an external case, a top cap and two terminals (plus and minus). In addition, it contains two current collectors, typically made from copper or aluminum and coated with the active materials of the cell electrodes (cathode and anode). The electrodes are kept separate using a thin sheet of polypropylene or polyethylene plastic. This sheet allows the lithium ions to pass between the anode and the cathode while preventing internal short circuits. The latter

[3] vda.de

[4] iso.org/standard/57871.html

Cell Type	**Volume** (**l**)	**Specific Capacity** (**Ah/l**)	**Specific Energy** (**Wh/l**)
PHEV1	0.309	65 – 81	243 – 292
PHEV2	0.357	62 – 76	255 – 275
PHEV2+	0.490	65 – 76	260 – 275
EV1	0.637	63	226
EV2	0.895	67	241
HEV	0.128	55	155 – 200

Table 2.2: Key parameters of prismatic cells

can occur due to dendrite or crystal growth on the electrodes. Overheating can also cause the separator to distort or melt resulting in short circuits. The electrodes together with the separator form the so called *jelly roll*. Without an electrolyte, the lithium ions cannot be transferred back and forth between the electrodes. Chemical inhibitors are often added to the electrolyte to make it self-extinguishing or flame-retarding in order to reduce the risk of fire or explosion in case a cell is physically damaged [11].

Graphite and carbon are often used as anode materials in lithium-ion cells due to their high thermal stability and electrical conductivity. For the cathode, the most common chemistry combinations include nickel manganese cobalt (NMC), nickel cobalt aluminum (NCA), lithium iron phosphate (LFP), lithium titanate (LTO), lithium manganese oxide (LMO) and lithium cobalt oxide (LCO). More reactive chemical combinations can be used to achieve higher energy densities. However, for safety reasons, battery manufacturers may compromise performance by using less reactive materials and mixes. For example, LCO provides a higher power density than LMO or LFP. However, since LMO and LFP are expected to be safer, they are more preferred for many applications [11].

2.1.3 Battery module design

The battery module is the basic building block of battery packs and can be regarded as a self-contained mechanical and electrical unit. It consists of several cells and provides a voltage typically below 60 V. Thus, modules can

be handled without extensive safety precautions [12]. The battery cells can be connected in series and/or in parallel. Connecting cells in parallel increases the battery capacity and improves the system failure rate. However, the assembly process and the cell interconnection system are more complex compared to simple series-connections [12].

The cell interconnection system of a module consists of the cell connectors and the wiring harness used for data acquisition including the temperature sensors and the voltage sense wires. The cell connectors are made from various copper and aluminum alloys. The temperature sensors are installed at so-called hot and cold spots. The voltage sense wires are connected to the cell connectors and used to measure the voltage of every single cell in the module.

2.1.4 Battery pack design

A battery pack consists of several interconnected modules. There is no standard size or topology for battery packs as they are usually designed to fit into the available space in the intended vehicle. Likewise, the number of cells in a battery pack depends on the application. A pack with a nominal voltage of 355 V can have up to 96 cells connected in series. Depending on the vehicle architecture for which the battery is designed, the modules might need to be spatially separated from each other. However, compact battery pack designs are more common. Battery systems with a compact design typically have a metal casing in which all the battery components and the BMS are enclosed. The casing protects the battery system and provides the mechanical and electrical interfaces to external components such as the DC/DC-inverter, the DC/AC-inverter and the vehicle control unit (VCU).

2.1.5 Safety components

Safety components used at the cell level include primarily the pressure vent and some of the pressure and temperature-based fuses such as the circuit interrupt devices (CIDs) and the polymeric positive temperature coefficients (PTCs). The pressure vent is only included in hard case-type cells. It is used as a final safety precaution to release the excess pressure in a controlled manner in case other safety devices fail. A CID is a non-resettable pressure-based

fuse, usually integrated into low power cells. It interrupts the current path through the cell in case of high internal pressure. Thermistors such as PTCs are resettable thermal fuses. Under normal operating conditions, a PTC has a low resistance. Under fault conditions, the cell temperature increases and causes the PTC's resistance to increase. Consequently, the cell shuts down. Upon cooling, the PTC resets to a low-resistance state and the cell is again usable. The PTC limits the maximum voltage provided by the cell. Therefore, its use is limited to small cells for low energy applications [11].

At the system level, a battery disconnect unit (BDU) is used to disconnect the battery pack from the remaining electric drive-train in safety-critical situations.

2.2 Battery management system

The BMS ensures a safe and reliable operation of the battery system. The electrical battery management prevents the cell voltage from exceeding or falling below the specified limits. It also regulates the charging and discharging current. On the other hand, the thermal battery management is used for temperature regulation. Batteries perform poorly at high and low operating temperatures. High temperatures affect the battery system in many aspects. For instance, a constantly high operating temperature causes the capacity to decrease. During charge and discharge, heat is generated from the cell and must be efficiently released in order to avoid a further increase in the temperature. Overheating can cause premature failure, aging and in the worst case thermal runaways leading to fire and explosion. Temperature uniformity within a cell and from cell to cell is important to maximize the battery performance and extend its lifespan. An excessive or uneven temperature increase may cause localized damages in the battery pack. It also reduces the battery's life-cycle, which is measured in terms of the number of complete charge/discharge cycles supported until depletion [13]. The BMS has to provide an accurate estimate of the state-of-charge (SoC) and the state-of-health (SoH) of the battery pack and predict its future behavior based on the current battery states and the past battery usage [14]. The SoH is determined as a function of the internal battery resistance, its capacity, the voltage, the self-discharge rate and the number of completed charge/discharge cycles. The BMS must also ensure data integrity

and identify reading errors. It should be able to distinguish between unusual but seemingly correct readings and readings containing errors, for example, due to hardware failure. In addition, voltage and current measurements need to be time-synchronized in oder to correctly calculate the power [12].

2.2.1 Subcomponents and topologies

A modular BMS consists of different subcomponents such as the CMUs, the MMUs and the PMU. The CMUs are used to monitor the battery cells and are responsible for data acquisition and cell balancing. They operate at low voltages (less than 5 V) and have different ground potentials. Therefore, they have to be galvanically isolated from each other [15].

An MMU is used to monitor a battery module with typically 8 to 12 cells. It also provides inter-cell balancing. In the literature, an MMU with integrated CMUs is sometimes referred to as a cell supervision circuit (CSC). In this case, the cell data is pre-processed by the MMU and passed on to the PMU. Similar to the CMUs, the MMUs have different ground potentials and are galvanically isolated from each other [15].

The PMU monitors the condition of the battery pack by estimating for example the SoC and SoH. The current and voltage of the battery pack are constantly monitored in addition to the isolation resistance between the battery pack terminals (HV+ and HV-) and the ground of the vehicle. The PMU is also responsible for controlling the MMUs and the pack safety devices like the pole cutting contactors. Furthermore, it handles the thermal management (the heating and cooling system) and communicates with external systems such as the VCU. The PMU operates at high voltages (up to 600 V). The ground potential of the PMU and that of the vehicle are the same. An isolated communication interface is needed between the PMU and the MMUs/CMUs due to different ground potentials. The galvanic isolation is also required in order to guarantee a strict separation between the subcomponents of the BMS operating at different voltages. This can be implemented using analog devices such as optocouplers. The following sections describe the topologies of state-of-the-art BMSs in a comparative manner. For more details, refer to [13, 15, 16].

2.2.1.1 Centralized topology

In centralized BMSs, the PMU unites the functionality of the PMU, MMU and CMU. The battery cells are connected to the PMU through a multitude of wires. Due to high complexity and maintainability requirements, centralized BMSs are less suitable for large battery packs.

2.2.1.2 Master-slave topology

The master-slave topology is the most commonly used topology in automotive BMSs. The master handles computation and communication tasks, while the slaves are remote monitoring and control devices. In order to easily manage the wiring complexity, the slaves should be placed as close as possible to the cells. Even though this topology is simple and cost-effective, it has the disadvantage that a defective master causes the entire system to fail [12].

2.2.1.3 Distributed topology

In a distributed BMS, identical BMS devices collaborate to monitor the condition of the battery pack. Each BMS device implements the functions of the CMU, MMU and PMU and can be used to supervise one or more cells. Distributed architectures offer more flexibility and have a better fault tolerance compared to non-distributed topologies. However, they are more complex and require advanced cell monitoring devices, a flexible and safe communication infrastructure, smart sensors and advanced real-time operating systems for a seamless coordination between the different devices [12].

2.2.2 Data acquisition

In order to take advantage of the maximum battery capacity, the data measurements need to be accurate. Any loss of accuracy adversely affects the battery longevity and performance. The BMS has an extremely noisy and often hot environment, which makes it very challenging to provide accurate and consistent data. State-of-the-art BMS monitoring devices achieve an accuracy between 0.5 % and 1.0 % for the current measurements (up to 450 A). For the cell voltage measurements, the accuracy is typically between 1 mV and 2 mV, while a measurement accuracy of at least 0.1 % is required for the pack voltage

measurements [12]. A cell voltage precision of 1 mV is usually equivalent to a 12 to 14 bits analog-to-digital converter (ADC).

2.2.2.1 Voltage measurement

The cells of a battery pack do not necessarily have the same capacity and/or the same SoC. For this reason, at least one voltage measurement per cell is required. Some BMSs measure in addition the module voltage or the voltage of a group of interconnected cells in order to detect systematic errors and diagnose wiring faults. In the case where the cell voltage is used to compute the SoC, the required cell voltage accuracy can be determined from the desired SoC accuracy and the shape of the battery open-circuit-voltage/state-of-charge curve (OCV/SoC curve) [17]. The voltage measurement range should cover the full range of possible cell voltages under normal conditions. A high accuracy is needed only for voltages within the normal operating range. Those outside that range do not need the same precision. Nonlinear compression can be used to represent the expected range of 0% to 100% SoC with a few bits. If for any battery cell the voltage goes beyond the safe operating range limits, the BMS shuts the cell down or switches to a limited operation mode. In this case, the calculation of accurate SoC and power limits may not be required or even possible. In order to ensure synchronization, a timestamp can be sent along with the cell voltage indicating when the measurement was performed [13].

2.2.2.2 Temperature measurement

The temperature measuring circuit must cover the largest possible operating range expected in a battery system. The optimum temperature operating range varies depending on the battery cell chemistry. The temperature measurements are often made over the temperature range -40 °C to 80 °C with a precision of 0.5 °C or 1 °C (7 to 8 bits). A nonlinear compression or special codes can be used to represent out-of-range temperature readings. Usually, temperatures outside the normal operating range do not require a high precision, because battery operation is inhibited [13].

The temperature measurement accuracy depends on the sensor signal chain and the sensor location. In case of large battery packs, it is very cost prohibitive to use one temperature sensor per cell. Thus, up to three external sensors are

typically used in each battery module. In this case, it is possible that the cell internal temperature exceeds the safe operating range before the temperature measurements indicate the problem. In addition, the detection probability of thermal events depends on how far the temperature sensors are from the affected cells. In the worst case, the cell voltages may exceed the safe operating range while all temperature readings remain inside the acceptable range [13]. A solution to this problem could be to use smart cells with integrated sensors (here we assume that the costs will be reduced and the accuracy will increase by integrating the sensors into the cell).

2.2.2.3 Current sensing

The sensor used to measure the battery pack current can be a resistive shunt, a current transformer or a Hall effect sensor. A shunt resistor is a high-precision resistor with a very low resistance. Measuring the current using a shunt resistor is the most prevalent method due to its robustness and high precision in case of very small and very large currents [12].

2.2.2.4 Smart cells

Battery cells with integrated BMS components are referred to as smart cells. Smart cells are the enablers for more advanced and efficient cell and battery management. More smartness at the cell level enhances the safety. Supported by the European technology platform on smart systems integration (EpoSS), the smart-LIC[5] project is one of the prominent projects dedicated to the topic of battery cell smartness. G. Meyer included in the first chapter of his book on the advanced micro-systems for automotive applications a description of the smart-LIC cell design [14]. The components to be integrated into the smart cell are the sensing elements, the actuators used for balancing and switching purposes, a monitoring unit for data (pre-)processing and storage and a bidirectional communication interface. The sensing elements of a smart cell measure the voltage, current and temperature. Additional integrated features including pressure measurement and the electrochemical impedance spectroscopy are within the scope of research, too. The bidirectional communication interface

[5]Smart and compact battery management system module for integration into lithium-ion cells for fully electric vehicles.

is based on a differential contactless data transmission bus using galvanically isolated, capacitively coupled data transmission links. The integrated cell monitoring unit collects the data from the sensors and sends them to the master using a capacitive coupling mechanism at data rates between 500 kbit/s and 1 Mbit/s. It can also activate passive balancing upon request from the master. The voltage measurement can be triggered by means of a broadcast command sent from the master to all the cells.

2.2.3 Communication

CAN is the most widely used standard bus system in BMSs. A CAN-enabled BMS component uses a high-speed CAN-transceiver with galvanic isolation, which is required to separate low- and high-voltage domains in order to prevent damages to communication devices. Isolated CAN also provides a good noise rejection. Data rates up to 1 Mbit/s are possible using high-speed CAN. Some of the commercially available off-the-shelf BMS devices have proprietary bus interfaces. For instance, Linear Technology's most recent battery stack monitor uses a two-wire isolated serial peripheral interface (isoSPI). The isoSPI interface translates a full-duplex SPI signal into a differential signal, which is then transmitted via a single pair of twisted wires [18]. The galvanic isolation is realized using standard transformers. Daisy-chains and bus configurations are supported. Based on the manufacturer specification, a reliable communication is possible for cable lengths up to 100 meters with data rates up to 1 Mbit/s.

2.3 Powerline communication

PLC is a communication technology that enables the use of the existing power cables in order to exchange data between different devices within a communication system. There are many applications of PLC. For instance, broadband PLC (BBPLC) is widely used as a last-mile access technology for Internet, voice over IP and high definition television. On the other hand, narrowband PLC (NBPLC) is used to provide building services such as smart grid management and metering, energy management, remote surveillance and remote control. A more comprehensive overview of narrow- and broadband PLC applications can be found in [19] and [20].

Many studies and researches have investigated the limitations and possibilities of using the PLC in automotive applications. In [21] for instance, a brief tutorial is given about the realization of a vehicular high-speed data communication on powerlines. It is shown that the electrical power supply system within an automobile has very few in common with the supply grid of residential areas and, therefore, new and different approaches are required. More details about the conducted study, the proposed approaches and the major findings can be found in [22].

Despite numerous studies, PLC has not yet been adopted as a standard communication technology for automotive applications, especially because high data rates are hard to achieve. For instance, the DC-BUS, which was developed by Yamar Electronics Ltd.[6] in cooperation with the DC-BUS Alliance, supports net data rates up to 250 kbit/s. This corresponds to a gross data rate of about 650 kbit/s. Maximum net data rates of 1.7 Mbit/s have been reached only with prototypes [23].

2.3.1 Channel characteristics

Primarily designed for power transmission, the powerlines do not represent a favorable medium for data communication. In the case of PLC over AC lines, the data must be transmitted at carrier frequencies above 3 kHz in order to avoid interference between the power and the data signals. The impedance of a PLC network changes constantly as a function of the load pattern. In case of impedance mismatch, multipath signal propagation occurs, which results in frequency-selective fading. Since electrical devices with different properties are connected to the powerlines, there are various noise sources.

In [24], an overview is given of the basic powerline topologies and the characteristics of powerline channels. The characterization and modeling of the channel in different PLC environments is discussed. Mathematical noise models are described in addition to the reference channels defined within the Open PLC European Research Alliance (OPERA) project and used in BBPLC to enable reproducible performance results and comparisons between different PLC solutions. Furthermore, some of the hardware emulation tools used for

[6] yamar.com

the analysis and design of PLC solutions are presented. Channel modeling is also addressed in [25], where it is shown that a set of common elements and parameters can be used for a general description of the powerlines of power supply systems with different structures and topologies. Channel emulation is another important topic. Channel emulators are extremely helpful in order to conduct various tests and compare the performance of different communication systems [26]. Depending on the frequency range and the transmit power, unshielded and untwisted powerlines might act as antennas receiving and emitting radio signals and, thus, disturbing other services operating in the same frequency range [27]. Limiting the power injected into the powerlines helps to combat cross-talk interference.

2.3.2 Modulation schemes

The use of robust modulation schemes in addition to channel coding allows for a reliable data transmission over the powerline. In [28–30], an overview is given of the most prevailing modulation and coding techniques for NBPLC and BBPLC including FSK, PSK combined with permutation coding, OFDM, filtered multitone (FMT) modulation, pulse-shaped OFDM, wavelet OFDM, OFDM with offset quadrature amplitude modulation (OQAM) and cyclic block FMT. FSK is widely used in NBPLC because it is highly resilient to signal strength variations and does not require linear amplifiers in the transmitter. Multi-carrier modulation techniques such as OFDM are used to achieve higher data rates. Prime and PLC G3 are common examples of NBPLC protocols using OFDM in combination with coded differential phase shift keying (DPSK) for data transmission in the CENELEC[7] A band (35 kHz–91 kHz). In OFDM systems with DPSK, the differential modulation can be either in the time or frequency domain, depending on the type of channel fading. A time domain DPSK (t-DPSK) allows for adaptive subcarrier allocation. Moreover, carriers with frequency-selective fading can be switched off [31]. t-DPSK can be applied only in case of quasi-stationary channels, i.e. channels that remain constant over at least two consecutive transmissions. OFDM with frequency domain DPSK (f-DPSK) has a lower implementation complexity compared to OFDM

[7] cenelec.eu

with t-DPSK. It also offers a better symbol error rate performance in case of fast fading channels.

The HomePlug protocol for BBPLC uses adaptive OFDM and supports three types of digital modulation schemes: coherent binary PSK (BPSK), differential BPSK (DBPSK) and differential quadrature PSK (DQPSK). Depending on the channel characteristics, different combinations of modulation formats and channel code rates are possible. This allows to adapt the sender to the channel and improve the data and error rates [32].

2.4 Single-carrier communication systems

This section gives a short overview of the digital single-carrier modulation schemes and the channel equalization algorithms used in state-of-the art communication systems.

2.4.1 Linear modulation

Single-carrier communication systems using linear modulation schemes have an end-to-end baseband configuration typically consisting of the transmit filter, the channel and the receive filter [33]. The signal at the output of the receive filter can be expressed as

$$y[k] = \sum_m a_m g[k - mT_\mathrm{s}] + n[k], \tag{2.1}$$

where a_m denotes the transmit symbols and $g[k]$ represents the equivalent baseband impulse response of the overall end-to-end system defined as

$$g[k] = g_T[k] * h_\mathrm{b}[k] * g_R[k], \tag{2.2}$$

where $*$ denotes convolution. $g[k]$, $h_\mathrm{b}[k]$ and $g_\mathrm{R}[k]$ are the discrete-time equivalent baseband impulse responses of the transmit filter, the channel and the receive filter, respectively. Typically, the transmit symbols are assumed to have zero-mean and be statistically independent and identically distributed (i.i.d.), while the channel noise $n[k]$ is modeled as additive white Gaussian noise (AWGN) with zero-mean and a constant spectral power density.

2.4.1.1 Modulation schemes

There are three types of linear modulation schemes: pulse amplitude modulation (PAM), PSK and QAM. In PAM, the signal amplitude is used to encode the information and the minimum distance between the constellation points is a function of the signal energy. Thus, PAM is highly susceptible to noise and interference [34]. Unlike PAM, PSK encodes the information into the phase of the transmit signal. The constellation points or symbols s_i are given by

$$s_i = A\left(\cos(\phi_i) + j\sin(\phi_i)\right), \quad \text{with} \quad \phi_i = 2\pi\frac{i-1}{M}, \tag{2.3}$$

where $i \in \{1, \cdots, M\}$, M is the modulation order and the amplitude A is a function of the signal energy. The minimum distance between the constellation points is $d_{\min} = A \cdot \sin(2\pi/M)$. A PSK signal has a constant envelope when rectangular pulse shaping is used. When pulse shaping filters with a better spectral efficiency are used, the PSK signal envelope is no longer constant and linear amplification is required in order to avoid amplitude distortion and spectral broadening [35].

In case of QPSK, abrupt phase transitions of up to 180 ° can be observed. This causes large amplitude variations and a high peak-to-average power ratio (PAPR) compared to constant envelope modulation [35]. Subsequently, a significant back-off from the saturation point is required for the operation of the power amplifier at the transmitter. Operation in back-off means that the maximum output power level must be reduced in order to avoid nonlinear distortion of the signal. The power amplifier's efficiency (ability to convert the direct current (DC) supply power into RF energy) decreases when the operation point is far below the saturation point. The efficiency of the power amplifier can be improved using for example active linearization by means of pre-distortion compensation. Systems requiring an improvement in the efficiency beyond what is achievable using active linearization techniques need to use more advanced power amplifier topologies [36]. The abrupt phase transitions in QPSK can be avoided by offsetting the quadrature component of the signal by half a symbol duration. This is called offset-QPSK (OQPSK). The offset makes the signal less sensitive to distortion during symbol transitions as the maximum phase transition is reduced from 180 ° to 90 ° [35]. Since OQPSK retains the orthogonality of the signals, it exhibits the same bit error performance as QPSK

and BPSK.

$\pi/4$-QPSK is another technique used to mitigate large amplitude variations of QPSK. Two identical QPSK constellations rotated by 45 ° with respect to one another are used. One constellation is used to select the even symbols. The other one is used to select the odd symbols. This technique allows for a maximum phase transition of 135 °, versus 90 ° for OQPSK and 180 ° for QPSK. In case of nonlinear amplification, $\pi/4$-QPSK is less spectrally efficient than OQPSK [35].

QAM encodes the information bits into both the amplitude and the phase of the transmit signal. It has the advantage of being more spectrally efficient than PAM and PSK. Both PSK and QAM require coherent demodulation. A coherent demodulator converts the received signal into a decision sample at maximum SNR using a matched filter or a correlator followed by a symbol rate-sampling circuit [37]. Carrier phase recovery is required in order to ensure that the local reference carrier is matched in phase to the received signal. This comes at the expense of receiver complexity, especially in case of time-varying channels. Independently of whether or not the demodulation is coherent, both carrier frequency recovery and symbol timing synchronization are required in order to avoid error performance degradation caused by frequency and/or timing offsets [33, 38].

2.4.1.2 Differential modulation

The differential modulation falls in the more general class of modulation with memory, where symbol sequences are mapped to phase transitions and a phase transition represents the differential phase between the current symbol and the previous one. In differential modulation, there is no need for a coherent phase reference at the receiver.

Noncoherent demodulation is less sensitive to random drifts in the carrier phase than coherent demodulation. However, it is not suitable for rapidly varying channels, where the signal phase can decorrelate between two symbols, making the previous symbol a very noisy phase reference. In addition, the error performance of DPSK is roughly 3 dB worse than that of coherent PSK due to the added noise of the reference symbol [35, 39].

2.4.1.3 Error performance

This section provides a brief overview of the error performance of the modulation schemes discussed above, where the focus is mainly on the results. For more details, interested readers can refer to [35]. In BPSK, each symbol corresponds to one bit. Thus, the symbol and bit error rates are equal. With coherent detection and perfect frequency and phase recovery, the bit error probability P_b in an AWGN channel is

$$P_\mathrm{b} = Q\left(\frac{d_\mathrm{min}}{\sqrt{2N_0}}\right) = Q(\sqrt{2\gamma_\mathrm{b}}), \quad \text{with} \quad \gamma_\mathrm{b} = \frac{E_\mathrm{b}}{N_0}, \tag{2.4}$$

where E_b is the bit energy, N_0 is the constant noise power spectral density and $Q(x)$ is given as

$$Q(x) = \frac{1}{2}\mathrm{erfc}\left(\frac{x}{\sqrt{2}}\right), \quad \text{with} \quad \mathrm{erfc}(x) = \frac{2}{\sqrt{\pi}}\int_0^x e^{-\tau^2} d\tau. \tag{2.5}$$

QPSK can be thought of as two orthogonal BPSK systems (in-phase and quadrature components). Therefore, QPSK has the same bit error performance as BPSK with twice the bandwidth efficiency. The symbol error probability equals the probability that either branch has an error and is obtained as follows:

$$P_\mathrm{s} = 1 - \left[1 - Q\left(\sqrt{2\gamma_\mathrm{b}}\right)\right]^2. \tag{2.6}$$

Assuming the symbol energy is split equally between the in-phase and quadrature branches, we obtain $\gamma_\mathrm{s} = 2\gamma_\mathrm{b}$ and $\gamma_\mathrm{s} = E_\mathrm{s}/N_0$, where E_s is the symbol energy. In this case, the symbol error probability can be expressed as

$$P_\mathrm{s} = 1 - \left[1 - Q(\sqrt{\gamma_\mathrm{s}})\right]^2. \tag{2.7}$$

According to [35], the average symbol error probability using coherent demodulation can be approximated by

$$P_\mathrm{s} \cong 2Q\left(\sqrt{2\gamma_\mathrm{s}}\sin\left(\frac{\pi}{M}\right)\right), \tag{2.8}$$

in case of coherent M-ary PSK with $M \geq 4$. If gray coding is used, mistaking a received PSK symbol for one of its nearest neighbors results in a single bit error which, at high SNR, leads to the approximation

$$P_\mathrm{b} \cong \frac{P_\mathrm{s}}{\log_2(M)}. \tag{2.9}$$

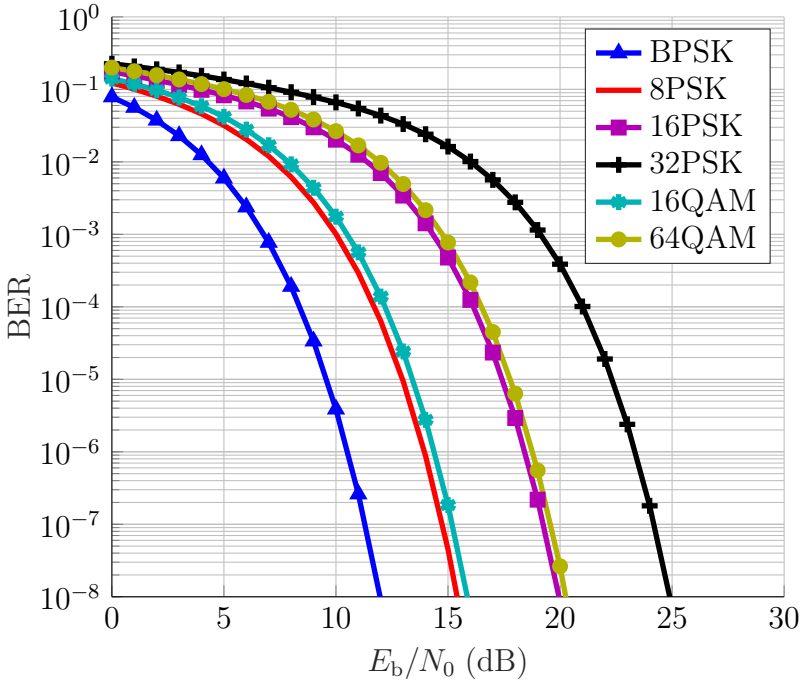

Figure 2.1: BER curves of linear digital modulation schemes

Finally, the average probability of bit error for M-ary QAM with square constellations using coherent demodulation can be approximated by

$$P_b \cong 2\left(\frac{\sqrt{M}-1}{\sqrt{M}\log_2(M)}\right)\operatorname{erfc}\left(\sqrt{\frac{3\log_2(M)}{2(M-1)}\gamma_b}\right), \tag{2.10}$$

as described in [35]. The BER curves of the above mentioned linear modulation schemes are shown in Figure 2.1.

2.4.1.4 Spectral and energy efficiencies

The spectral efficiency refers to the information rate that can be transmitted over a given bandwidth in a specific communication system. Table 2.3 provides an overview of the maximum spectral efficiency achieved using different digital modulation schemes in an AWGN channel. The spectral efficiency increases as the modulation order increases. The Table also includes the E_b/N_0 required by the modulation schemes under consideration to reach a BER of 10^{-6}. QAM distributes the constellation points more evenly than PSK and hence achieves a greater distance between adjacent constellation points. This explains why

Modulation Scheme	**Maximum Spectral Efficiency** (**bit/s/Hz**)	$\boldsymbol{E_b/N_0}$ (**dB**)
BPSK	1	10.6
QPSK, 4-QAM	2	10.6
8PSK	3	14
16QAM	4	14.5
16PSK	4	18.3
32PSK	5	23.3
64QAM	6	18.8

Table 2.3: E_b/N_0 in an AWGN channel at BER = 10^{-6} [40]

QAM is more energy efficient than PSK. For instance, 16QAM requires 4 dB less E_b/N_0 than 16PSK to achieve a BER of 10^{-6}.

2.4.2 Frequency modulation

In frequency modulation, the information bits are encoded in the frequency of the transmit signal. Therefore, the transmit signal has a constant envelope. In M-ary FSK for instance, orthogonal frequencies are used and the modulated signal is given by

$$s_{\mathrm{FSK}}(t) = A\cos(2\pi f_c t + 2\pi\alpha_i \Delta f_c t + \phi_i), \quad \text{with} \quad iT_s \leq t < (i+1)T_s \tag{2.11}$$

where f_c is the carrier frequency assuming passband data transmission, $\alpha_i \in \{\pm 1, \pm 3, \cdots, \pm(M-1)\}$ and ϕ_i is the phase of the i-th signal. In case of coherent demodulation, a minimum frequency separation $\Delta f_{\min}$ of $1/2T_s$ is required in order to maintain the orthogonality between the FSK frequencies. In case of noncoherent demodulation, orthogonality is achieved with $\Delta f_{\min} = 1/T_s$.

The FSK signals can have different phases. This results in phase discontinuity in the transmit signal. Such discontinuities can increase the signal bandwidth and lead to undesirable spectral broadening [35, 39]. Continuous phase frequency shift keying (CPFSK) eliminates the phase discontinuity. In CPFSK, the modulated signal is given by

$$s_{\mathrm{CPFSK}}(t) = A\cos(2\pi f_c t + \theta(t)), \quad \text{with} \quad \theta(t) = 2\pi\beta \int_{-\infty}^{t} m(\tau)d\tau \tag{2.12}$$

where β is the modulation index and $m(t)$ is a PAM signal given as

$$m(t) = \sum_k a_k g(t - kT_\mathrm{s}), \tag{2.13}$$

where a_k are the information bits and $g(t)$ is the frequency pulse. The bandwidth occupancy of CPFSK is dependent on $\Delta f_{\min}$. According to Carson's rule, for small β, the transmission bandwidth of $s(t)$ is approximated by

$$B_\mathrm{s} \approx M\Delta f_{\min} + 2B_\mathrm{g}, \tag{2.14}$$

where B_g is the bandwidth of the shaping pulse $g(t)$. The spectral occupancy of CPFSK-modulated signals is larger than that of linearly modulated signals by $M\Delta f_{\min}$. Since $\Delta f_{\min}$ is inversely proportional to the symbol duration T_s, the spectral efficiency penalty of CPFSK relative to linear modulation increases as a function of the symbol rate [35, 39].

Minimum shift keying (MSK) is a special case of FSK with a minimum frequency separation $\Delta f_{\min} = 1/2T_\mathrm{s}$. MSK can be thought of as binary CPFSK with $\beta = 1/2$ or as a special case of OQPSK with sinusoidal symbol weighting. When a matched filter is used to recover the information from each of the two quadrature components independently, MSK has the same error performance as QPSK and BPSK. Due to sinusoidal symbol weighting, MSK has lower sidelobes than OQPSK. On the other hand, the MSK main lobe is wider than that of OQPSK, which can be detrimental in the case of narrowband links [35, 39].

Gaussian minimum shift keying (GMSK) is a special case of MSK using a Gaussian filter for pre-modulation pulse shaping. The Gaussian filter used in GMSK is generally specified by its time-bandwidth product given by BT_s, where B is the 3 dB bandwidth of the filter and T_s is the symbol duration. The smaller the time-bandwidth product, the more ISI is produced by the filter. If BT_s is less than 0.3, some form of ISI mitigation is required. Even with a low BT_s values the bandwidth efficiency of GMSK is less than that of filtered QPSK [35, 39].

2.4.2.1 Coherent and noncoherent demodulation

The coherent demodulation of FSK signals requires the received signal to be matched in phase to the carrier signal. This can be realized using for

example one carrier phase recovery circuit for each FSK frequency. No phase synchronization is required in case of noncoherent demodulation. A noncoherent demodulator uses for each carrier frequency a filter matched to that frequency followed by an envelope detector and sampler. Noncoherent demodulation can also be performed by multiplying the received signal by a noncoherent in-phase and quadrature signal at each carrier frequency, integrating it over the symbol duration, sampling it and, finally, squaring it in order to obtain the signal energy. The detector outputs the bit sequence corresponding to the frequency of the branch with the highest energy.

Frequency and timing errors adversely affect the performance of FSK modulation. Thus, both carrier frequency recovery and symbol timing synchronization are necessary [35].

2.4.2.2 Error performance

Acoording to [35], the symbol error probability P_s of M-ary FSK with coherent demodulation can be upper-bounded by

$$P_\mathrm{s} \leq \frac{1}{2}(M-1)\mathrm{erfc}\left(\sqrt{\frac{\log_2(M)}{2}\gamma_\mathrm{b}}\right), \tag{2.15}$$

in an AWGN channel. The bit error probability P_b can be expressed as a function of the symbol error probability as follows:

$$P_\mathrm{b} = \frac{M}{2(M-1)}P_\mathrm{s} \quad \leq \quad \frac{M}{4}\mathrm{erfc}\left(\sqrt{\frac{\log_2(M)}{2}\gamma_\mathrm{b}}\right). \tag{2.16}$$

In case of coherent binary FSK (BFSK), P_b can be calculated as

$$P_\mathrm{b} = Q(\sqrt{\gamma_\mathrm{b}}). \tag{2.17}$$

The symbol error probability of noncoherent M-ary FSK is given according to [35] by

$$P_\mathrm{s} = \sum_{m=1}^{M}(-1)^{m+1}\binom{M-1}{m}\frac{1}{m+1}\exp\left(\frac{-m\gamma_\mathrm{s}}{m+1}\right). \tag{2.18}$$

In FSK, the power efficiency increases as a function of the modulation order. However, this expectedly comes at the cost of an expanded spectral occupancy. For example, Figure 2.2 shows that 2FSK requires at least 3 dB more E_b/N_0

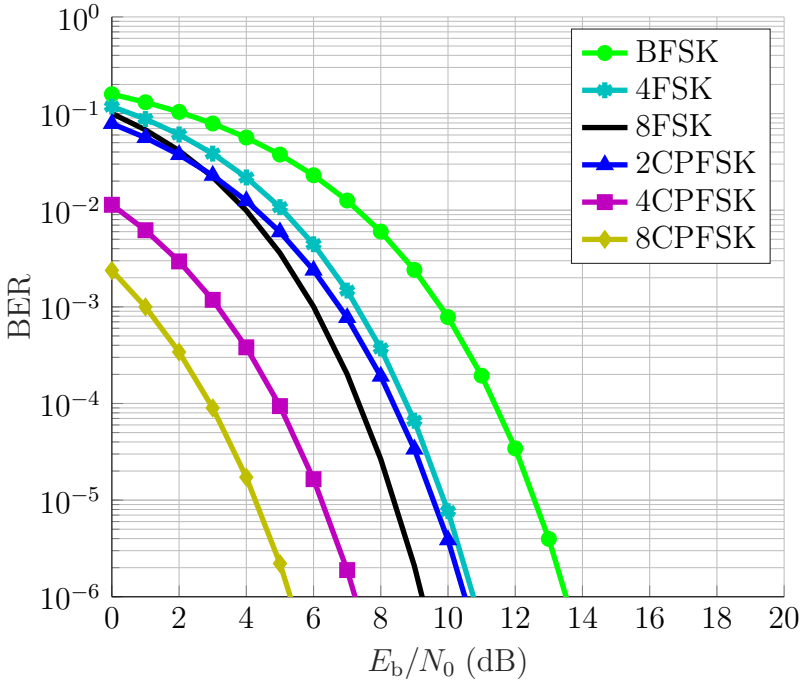

Figure 2.2: BER curves of FSK and CPFSK ($\beta = 1/2$) with coherent demodulation

than 4FSK to reach the same BER. In case of CPFSK, the error probability analysis needs to be performed over multiple symbols due to the memory in the modulation [35, 41]. Figure 2.2 shows the BER curves obtained using FSK and CPFSK. We can see that CPFSK with $\beta = 1/2$ requires 3 dB less E_b/N_0 than FSK to reach the same BER.

2.4.3 Channel equalization

ISI degrades the BER performance of communication systems and has therefore to be eliminated using channel equalization. In this section, we introduce the Nyquist ISI criterion and give a brief overview of linear and nonlinear equalizers.

2.4.3.1 Intersymbol interference (ISI)

Based on (2.1), the signal at the output of the receive filter can be expressed according to [42] as

$$y[k] = a_k g[0] + \sum_{m \neq k} a_m g[k-m] + n[k], \tag{2.19}$$

where a_k is the k-th transmit symbol and $y[k]$ is the k-th received symbol. The second term in (2.19) represents the ISI affecting the symbol a_k. The ISI depends on the channel characteristics and the transmit symbol sequence. Independently of the transmit signal power, the ISI can give rise to an irreducible error floor. An approximation to the BER with ISI can be obtained by treating the ISI as an uncorrelated white Gaussian noise. This leads to the signal-to-interference-plus-noise ratio (SINR) defined as

$$\mathrm{SINR} = \frac{P_\mathrm{r}}{N_0 B + I}, \tag{2.20}$$

where P_r is the received signal power and I is the average power associated with the ISI. The influence of the ISI becomes more significant as the data rate increases and the symbol duration T_s becomes smaller. The impact of ISI on the symbol error rate is often analyzed by means of simulations since different channel models, modulation schemes and symbol sequence characteristics are possible [35].

2.4.3.2 Nyquist ISI criterion

The Nyquist ISI criterion specifies the necessary and sufficient conditions to be fulfilled in the time and frequency domains in order to ensure ISI-free data transmission. In the time domain, the received pulse shape must be null at the ideal sampling points associated with past or future symbols, i.e.

$$g[k] = \delta[k] = \begin{cases} 1, & k = 0 \\ 0, & k \neq 0. \end{cases} \tag{2.21}$$

In the frequency domain, summing up all the spectra obtained by shifting the signal spectrum by multiples of $1/T_\mathrm{s}$ must result in a constant [42], i.e.

$$\sum_{k=-\infty}^{\infty} G\left(f - \frac{k}{T_\mathrm{s}}\right) = T_\mathrm{s}. \tag{2.22}$$

The ISI would be completely removed from the received signal, if the frequency response of the equalizer is equal to the inverse of the channel frequency response $H(f)$ and the combination of the transmit and receive filters yields a Nyquist filter. However, after passing through such an equalizer the white Gaussian noise would be colored and the noise power spectral density would be equal to $N_0/|H(f)|^2$. As a result, the noise power would be enhanced at the frequencies with high channel attenuation. Such an equalizer has a poor performance even though the ISI effects are completely eliminated. Thus, the equalization algorithm should be designed to mitigate the effects of ISI and at the same time maximize the SNR of the post-equalization signal [35].

2.4.3.3 Equalizer types

The three most important equalization schemes used to mitigate ISI are maximum-likelihood sequence estimation (MLSE), linear equalization (LE) and decision feedback equalization (DFE). The MLSE algorithm achieves the best BER performance. It is however highly complex, especially for long channel impulse responses, since it uses sequence estimation for detection. In practice, suboptimal equalizers with a lower complexity are often preferred. Linear equalizers such as the minimum-mean square error (MMSE) equalizer remove the ISI symbol-by-symbol and detect the symbols individually. However, they typically suffer from noise enhancement in frequency-selective fading channels. In comparison, decision feedback equalization (DFE) is fairly simple to implement and does not suffer from noise enhancement. At low SNR, however, DFE may perform poorly due to error propagation [35].

The MMSE algorithm minimizes the expected mean squared error (MSE) between the transmit symbols and the equalizer output and, thus, provides a good balance between ISI mitigation and noise enhancement. If the noise is white at the input of the equalizer, finding the optimal filter coefficients is a standard Wiener filtering problem [43]. If, however, the noise is colored due for example to matched filtering, the equalizer can be divided into two components, a noise whitening filter and an ISI removing filter. Let $X(k)$, $Y(k)$ and $\tilde{Y}(k)$ be the random processes representing the transmit signal, the signal at the input of the equalizer and the signal after equalization, respectively. As shown

in [39], the cost function used to derive the equalizer coefficients is defined as

$$F_{\mathrm{MSE}} = \boldsymbol{E}\left\{\left|\tilde{Y}(k) - X(k-k_0)^2\right|\right\}, \quad \text{with} \quad \tilde{Y}(k) = \mathbf{Y}^{\mathrm{T}}\mathbf{e}, \tag{2.23}$$

where $\boldsymbol{E}$ stands for the expected value, k_0 represents the delay caused by the channel and the equalizer, $\mathbf{e}$ is the equalizer coefficients vector and $\mathbf{Y}$ is defined as

$$\mathbf{Y} = \begin{pmatrix} Y(k) \\ Y(k-1) \\ \cdots \\ Y(k-n_{\mathrm{e}}+1) \end{pmatrix}, \tag{2.24}$$

where n_{e} is the number of equalizer coefficients. F_{MSE} is minimized, and thus the minimum MSE is obtained, when $\mathbf{e}$ is equal to $\mathbf{R}_{\mathrm{YY}}^{-1} \cdot \mathbf{r}_{\mathrm{YX}}$, where $\mathbf{R}_{\mathrm{YY}}$ is the autocorrelation matrix of $\mathbf{Y}$ and $\mathbf{r}_{\mathrm{YX}}$ is the cross-correlation vector between $\mathbf{Y}$ and $X(k-k_0)$ [39]. In frequency ranges with deep spectral nulls in the channel, a DFE would perform much better than a linear equalizer. In general, a DFE equalizer consists of a linear feedforward filter, which mitigates a part of the ISI by means of linear filtering, and a nonlinear feedback filter, which removes the remaining ISI by making a hard decision on the previous symbols and removing their effect from the incoming symbols. Let $\tilde{Y}_{\mathrm{q}}$ be the random process representing the output of the decision feedback equalizer. By definition,

$$\tilde{Y}_{\mathrm{q}}(k) = \mathbf{Y}^T\mathbf{e} - \mathbf{X}^T\mathbf{b}, \tag{2.25}$$

where the first term is the output of the feedforward filter with $\mathbf{e}$ as its coefficients and the second part represents the detected symbols $\mathbf{X}$ weighted by the feedback filter coefficients $\mathbf{b}$. The cost function to be minimized in order to obtain $\mathbf{e}$ and $\mathbf{b}$ is given according to [39] by

$$F_{\mathrm{qMSE}} = \boldsymbol{E}\left\{\left|\tilde{Y}_{\mathrm{q}}(k) - X(k-k_0)\right|^2\right\}. \tag{2.26}$$

The feedforward filter coefficients are given by

$$\mathbf{e} = \left[\mathbf{R}_{\mathrm{YY}} - \frac{1}{\sigma_{\mathrm{X}}^2}\mathbf{R}_{YX}\mathbf{R}_{YX}^H\right]^{-1} \cdot \mathbf{r}_{\mathrm{YX}}, \tag{2.27}$$

Algorithm	$\boldsymbol{N}_{\mathbf{mult}}$	**Complexity**	**Convergence**	**Tracking**
LMS	$2n_\mathrm{e} + 1$	low	Slow	Poor
MMSE	n_e^2 to n_e^3	very high	Fast	Good
RLS	$2.5n_\mathrm{e}^2 + 4.5n_\mathrm{e}$	high	Fast	Good
Fast Kalman	$20\ n_\mathrm{e} + 5$	fairly low	Fast	Good
Square Root RLS	$1.5\ n_\mathrm{e}^2 + 6.5\ n_\mathrm{e}$	high	Fast	Good

Table 2.4: Training and tracking characteristics of equalization algorithms, where N_mult is the number of multiply operations and n_e is the number of equalizer taps [35]

while the feedback filter coefficients can be calculated as

$$\mathbf{b} = \frac{1}{\sigma_\mathrm{X}^2}\mathbf{R}_{YX}^H \cdot \mathbf{e}, \quad \text{with} \quad \sigma_\mathrm{X}^2 = \boldsymbol{E}\left\{\left|X(k)\right|^2\right\}, \tag{2.28}$$

where $\mathbf{R}_\mathrm{YX}$ is the cross-correlation matrix between $\mathbf{Y}$ and $\mathbf{X}$. In case of a time-varying environment, the system must periodically estimate the channel and update the equalizer coefficients accordingly. Thus, adaptive equalizers are used. The length of the training sequence used for channel estimation depends on the number of equalizer coefficients to be determined and the convergence speed of the training algorithm [35]. A summary of the training and tracking characteristics of different algorithms is given in Table 2.4 as a function of the number of equalizer taps denoted by n_e. As can be seen, the least mean squares (LMS) algorithm does not seem to be good enough due to its poor tracking and slow convergence. Better results can be achieved using either the fast Kalman or the square root recursive least squares (RLS) algorithms, which however may be unstable in their convergence and tracking [35].

2.5 Media access control

Based on the open system interconnection (OSI) model, the MAC layer is one of two sublayers of the data link layer and is used to manage the access of multiple network devices to a shared physical medium. In a communication system with multiple devices, the MAC protocol allows to prevent collisions

and ensure a fair resource sharing. MAC protocols are divided into fixed and dynamic access protocols. MAC protocols with fixed access are based on reservation. Thus, they ensure a collision-free data transmission, a good network utilization and an easy realization of quality of service (QoS) guarantees, which makes them suitable for time-critical applications [27]. MAC protocols with dynamic access can be classified into contention and arbitration protocols. The contention protocols use random access and are suitable for bursty traffic. However, they have a poor network utilization. For instance, in a highly loaded network the utilization decreases due to the collisions and the high number of retransmissions. The performance can be improved by reducing the collision probability in the network and using mechanisms for collision resolution as an additional feature [27]. Arbitration protocols like token-passing and polling use an arbitration mechanism in order to coordinate the connected devices between each other and avoid collisions. The arbitration procedure requires additional time and hence causes longer transmission delays. Therefore, dynamic MAC protocols with arbitration are less suitable for time-critical services [27].

2.5.1 Frequency and time division duplexing

Transceivers supporting frequency division duplexing (FDD) are able to simultaneously transmit and receive signals using different frequency bands for the up- and downlinks. Systems using FDD are called full duplex. FDD requires the use of diplexers able to isolate the transmit and receive paths so that simultaneous transmission and reception are possible. FDD is best suited for continuous and symmetric data traffic and is, thus, an efficient technique for a communication network with fairly constant and balanced traffic in both transmission directions [27].

Half duplex communication systems use TDD, where both the transmitter and receiver operate in the same frequency band but at different times. Mixers, oscillators and frequency synthesizers can be, therefore, reused. In Addition, the diplexer can be replaced by a lower cost transmit/receive switch, thereby eliminating the complexity and costs associated with isolating the transmit and receive signals. TDD is best suited for bursty and asymmetric data traffic. Using dynamic TDD, the capacity for up- and downlinks can be flexibly allocated based on the traffic demand. This improves the channel utilization. Moreover,

an effective power control can be achieved due to the reciprocity of the up- and downlinks [27].

2.5.2 Multiple access schemes

Multiple access schemes like TDMA, frequency division multiple access (FDMA) and code division multiple access (CDMA) are used by MAC protocols with fixed access (reservation-based). TDMA, FDMA and CDMA divide the physical channel into multiple orthogonal transmission channels. In TDMA, the orthogonality between the transmission channels is provided in the time domain, while in FDMA the channels are orthogonal in the frequency domain. In CDMA systems, the transmission channels are defined by special code sequences and the orthogonality between them is provided by the orthogonality of the applied codes [27].

2.5.2.1 Time division multiple access

In TDMA, network devices use the same frequency band but at different times. TDMA divides the time axis into time slots of equal duration. Each time slot is assigned to a device. The slot assignment follows a pre-defined pattern, which is repeated periodically. Typically, a guard interval is added at the end of each time slot to ensure that distinct transmissions do not interfere with each other. Guard intervals also reduce the impact of clock instability and differences in transmission, propagation and processing delays. TDMA/TDD-based systems are half-duplex. Half duplex systems have two types of time frames, downlink and uplink frames. Transmission and reception occur at different times. Therefore, the transmitter can be turned off during reception. TDMA-based systems can be made full duplex using FDD (TDMA/FDD) [27].

2.5.2.2 Frequency division multiple access

FDMA divides the entire available frequency band into non-overlapping subbands representing the transmission channels to be allocated to the network devices. Typically, the subchannels are narrowband and the data rate per subchannel is fixed and small. FDMA requires guard bands between the channels allocated by the devices in order to mitigate the intercarrier interference

(ICI). In addition, selective narrowband filtering is needed by each device. Even though TDMA tends to have a higher data transfer overhead (protocol and frame synchronization) than FDMA, the guard interval associated with it typically utilizes less capacity compared to the guard band linked with the FDMA technique. While TDMA is used for bursty data transmission and requires an accurate system-wide clock synchronization, FDMA is best suited for continuous data transmission without the need for clock synchronization between the network devices and the master [27].

2.5.2.3 Code division multiple access

CDMA is based on the spread-spectrum principle. Multiplexing between different devices is realized through the use of orthogonal codes. The devices use the same frequency band and can transmit data simultaneously. Thus, the chosen code sequences must have good auto- and cross-correlation properties [27]. Direct-sequence CDMA (DS-CDMA) and frequency hopping CDMA (FH-CDMA) are two possible realizations. DS-CDMA is based on direct sequence spread spectrum (DSSS), where a specific binary sequence is used for data spreading, while FH-CDMA is based on frequency hopping spread spectrum (FHSS), where the signal transmission is spread over different frequency bands as defined by the frequency hopping pattern [19].

Chapter 3

Technical Feasibility Analysis

3.1 System overview

This thesis focuses on BMSs with a master-slave configuration. Compared to state-of-the-art wired communication technologies, PLC requires less wiring and can be used for cost-effective solutions. However, if each battery cell is monitored and controlled individually, a reduction in the overall costs can only be achieved if the cost per CMU is kept low. Cost and complexity are interrelated. While the hardware complexity of a CMU is determined by the transceiver architecture, the computational complexity mainly depends on the chosen digital signal processing algorithms and can be, thus, reduced by using less complex or more optimized and efficient physical layer algorithms.
Cost and complexity are not the only key factors underpinning the design of the PLC system components. Other key factors are data transmission robustness, communication data rate and power consumption.

We consider a PLC system consisting of as many CMUs as cells in the battery pack. A CMU continuously measures the cell voltage, temperature and (possibly) pressure. The measurement data need to be regularly sent to the PMU in order to reliably monitor the condition of the battery. As explained in Section 2.2.2, state-of-the-art BMSs require an accuracy of at least 1 mV for cell voltage measurements. As a result, at least 14 bits are required to encode the cell voltage, which is typically between 3.2 V and 3.8 V (nominal voltage). For the cell temperature, a precision of 0.5 °C to 1 °C is required. Therefore, at least 7 bits are needed. For the pressure, we assume that 7 bits are sufficient.

The CMUs are daisy-chained to each other and back to the PMU via the powerlines. The PLC system supports communication in both directions, from the PMU to the CMUs (downlink) and the other way round (uplink), where data rates above 1 Mbit/s are expected. We assume that the data transmission in the uplink is bursty, i.e. a CMU transmits data intermittently rather than as a continuous stream. As mentioned earlier, there are different types of cell measurements which don't necessarily have the same update rate. For instance, the cell voltage can be measured more frequently and transmitted more often to the PMU than the temperature or the pressure. The bursty character of the data transmission is an important design criterion with a significant impact on the choice of the media access scheme for the PLC system.

Since the CMUs are powered by the battery cells, both the physical and the MAC layers have to be as energy efficient as possible. Since BMSs are safety-critical systems, the PLC system is expected to be highly-reliable, i.e. it should be able to sustain its functionality under the given operation conditions over its entire lifetime. Not only do timing constraints and functional requirements have to be met, but also a robust data transmission is required without additional complexity. In such cases where different key factors for the system design come into play, trade-offs are inevitable.

3.1.1 MAC protocol

The choice of the media access scheme for the MAC protocol is an important issue in the design of the PLC system. As explained in Section 2.5, reservation-based MAC protocols avoid collisions and long transmission delays. Due to the bursty nature of the PLC data traffic and based on Section 2.5.2, TDMA seems to be the most suitable multiple access scheme for our application. In case the network traffic is asymmetric, TDD can be used and the PLC system would be half-duplex. As shown in Section 2.5.1, TDMA/TDD allows for a simple and cost-effective solution compared to TDMA/FDD. By exploiting the channel reciprocity in the up- and downlink, a more effective power control can be achieved using TDD and, thus, the energy efficiency of the PLC system can be improved. The CMUs can estimate the downlink channel and use it to adjust the transmit power. Similarly, the PMU can estimate the uplink channel and adjust the transmit power, accordingly. The overall energy consumption

of the PLC-system can be further reduced by switching the PLC transceivers into an energy saving mode when no data transmission is required.

TDMA-based communication protocols offer a deterministic data communication with time-triggered control and periodic signal transmission. The communication over the channel is based on a pre-defined schedule. In order to support sporadic data transmission, a dynamic segment with a fixed time length can be added to the communication cycle, similar to the FlexRay standard [44]. Such an approach combines the advantages of time-triggered and event-triggered communication. Owing to the finite length of the dynamic segment, the data communication in the static segment is still deterministic. However, there is no guarantee that all the battery cells wishing to send dynamic messages are scheduled in the same communication cycle. Some sporadic messages might need to be transmitted in subsequent cycles.

Unlike FDMA, TDMA benefits from the implicit frequency diversity of broadband and frequency-selective channels, which helps to mitigate the effects of frequency-selective fading. If a training sequence is required for frame synchronization or channel estimation, its length should be much smaller than that of the data packet in order to improve the overall channel utilization.

The basic architecture of a PLC-enabled CMU is illustrated in Figure 3.1. The CMU has a PLC interface used to connect it to the DC power lines. The PLC interface consists of a PLC transceiver and a communication controller (CC). The PLC transceiver implements the physical layer. It consists of an AC-coupling circuit, an analog front-end (AFE) including the transmit and receive blocks and a digital processor. The CC is used to implement the data link layer including the MAC protocol. It can be designed as a stand-alone controller or as a peripheral module of a host application microcontroller (host MCU). An integrated design allows for simple and fast communication between the host and the PLC controllers, while more flexibility can be achieved with a stand-alone CC. The CC executes the communication protocol using different communication components for protocol operation control, media access control, framing, error detection, error handling and clock synchronization. As for the host, it provides control and/or configuration information to the CC and the transceiver.

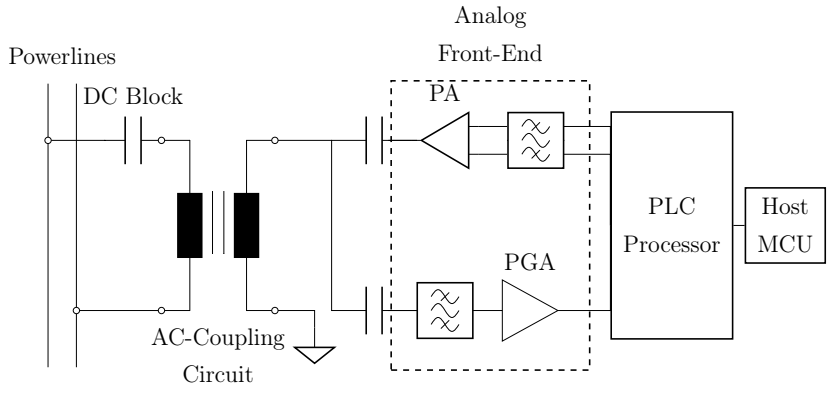

Figure 3.1: Basic architecture of a PLC-enabled cell monitoring unit

3.1.2 Data rate derivation

As mentioned in Section 3.1.1, a TDMA-based communication cycle can be divided into a static and a dynamic segment. The static segment is organized into a number of time slots of equal lengths. Guard intervals are added between the time slots in order to reduce the effect of time synchronization errors and guarantee a smooth deterministic data transmission in the static segment. In practice, an exhaustive specification of the PMU commands and the battery cell data packet format is required for the design of the static communication schedule.

The minimum data rate of the PLC system can be determined as a function of the number of battery cells N, the time slot duration T_{slot}, the guard interval T_{g}, the update rate(s) of the cell measurements, the number of time slots reserved to the PMU and those reserved to the CMUs per communication cycle. All the parameters relevant for the data rate derivation are listed in Table 3.1 for ease of reference. We assume that the communication cycle does not include a dynamic segment for sporadic data. The minimum required data rate is expected to be higher in case the communication cycle includes a dynamic segment in addition to the static one. The length of the time slot is determined by the longest data packet (either a PMU or a CMU data packet), the largest possible signal delay and the largest possible time deviation between the CMUs and the PMU due to timing errors. For the data rate derivation, we neglect the effect of signal delay and time deviation and obtain the following expression

for the time slot duration:

$$T_{\text{slot}} = T_{\text{p}} + T_{\text{g}}, \quad \text{with} \quad T_{\text{p}} = \frac{L_{\text{p}} + L_{\text{o}}}{R_{\text{b}}}, \tag{3.1}$$

where T_{p} is the time duration of the longest data packet, L_{p} is the payload length (in bits), L_{o} is the overhead length (in bits) and T_{g} is the guard interval duration. The communication cycle duration T_{cycle} is determined by the time slot duration T_{slot} and the total number of slots N_{slots} as follows:

$$T_{\text{cycle}} = N_{\text{slots}} T_{\text{slot}}, \quad \text{with} \quad N_{\text{slots}} = N_{\text{slots,pmu}} + N_{\text{slots,cells}}. \tag{3.2}$$

A real-time communication between the CMUs and the PMU (with negligible latency) allows to improve the reaction time of the PMU in critical situations. In order to support real-time communication, the communication cycle can be designed such that T_{cycle} is equal to T_{u}, which is the shortest update period of the cell measurements. By replacing T_{cycle} in (3.2) with T_{u} and substituting T_{slot} with its expression given in (3.1), we obtain

$$R_{\text{b}} = \frac{(L_{\text{p}} + L_{\text{o}}) N_{\text{slots}}}{T_{\text{u}} - T_{\text{g}} N_{\text{slots}}}, \tag{3.3}$$

where T_{g} is determined based on the delay spread of the physical channel. Longer guard intervals provide better protection against interference to the following time slot. However, this comes at the cost of lower channel efficiency. For instance, in the IEEE 802.11 standard, the symbol guard interval is equal to 0.8 µs [45]. The IEEE 802.11n standard adds optional support for a 0.4 µs guard interval [46], which provides 11% increase of the net data rate.

3.1.2.1 Equal measurement update rates

In case voltage, temperature and pressure measurements have equal update rates, the number of slots N_{slots} can be calculated as

$$N_{\text{slots}} = N_{\text{slots,pmu}} + N N_{\text{slots,cell}}. \tag{3.4}$$

Instead of using separate data packets for voltage, temperature and pressure, a CMU can send all the required cell data in one data packet. In this case, we have $N_{\text{slots,cell}} = 1$ and

$$R_{\text{b}} = \frac{(L_{\text{p}} + L_{\text{o}}) N_{\text{slots}}}{T_{\text{u}} - T_{\text{g}} N_{\text{slots}}}, \quad \text{where} \quad N_{\text{slots}} = N_{\text{slots,pmu}} + N. \tag{3.5}$$

Parameter	**Description**
T_{cycle}	Communication cycle duration
T_{slot}	Time slot duration
T_{g}	Guard interval duration
N_{slots}	Number of time slots per communication cycle
$N_{\text{slots,pmu}}$	Number of time slots reserved to the PMU per communication cycle
$N_{\text{slots,cells}}$	Number of time slots reserved to the CMUs per communication cycle
$N_{\text{slots,cell}}$	Number of time slots reserved to one CMU per communication cycle
$N_{\text{m,cell}}$	Number of cell measurement types
N	Number of battery cells
T_{u}	Shortest update period of the cell measurements
T_{p}	Time duration of the longest data packet
L_{p}	Payload length of the longest data packet (in bits)
L_{o}	Overhead length per data packet (in bits)
γ_{over}	Data overhead factor
L_{d}	Maximum length of cell data (in bits)
R_{b}	Data rate in bit/s

Table 3.1: TDMA-based communication cycle parameters

Reducing the number of data packets per CMU per communication cycle improves the channel utilization efficiency, which is one of the key aspects to consider when designing the communication schedule. In order to better understand the relation between the data rate and the key design parameters listed in Table 3.1, we consider the example of a battery system with $N = 100$ cells and assume that $T_\mathrm{g} = 0.4\,\mu\mathrm{s}$, $N_\mathrm{slots,pmu} = 2$, $N_\mathrm{slots,cell} = 1$ and $L_\mathrm{p} = 40\,\mathrm{bits}$. Figure 3.2 shows the data rate obtained with these parameter values as a function of the measurement update period T_u and the data overhead factor γ_over, defined as the ratio of L_o to L_p. The update period varies between 1 ms and 40 ms, while the overhead factor is chosen between 0 and 0.5. A minimum data rate of 4.2 Mbit/s is required, when $T_\mathrm{u} = 1\,\mathrm{ms}$ and $\gamma_\mathrm{over} = 0$. An increase in the overhead factor results in a higher data rate. For instance, the data rate is equal to 5.1 Mbit/s with $\gamma_\mathrm{over} = 0.2$. While data rates far above 2 Mbit/s are expected with an update period of 1 ms, we notice that the data rate is significantly below 1 Mbit/s for update periods longer than 5 ms. When channel coding is applied, a data rate increase by $1/R_\mathrm{c}$ compared to the uncoded case is expected, in order to maintain the net data throughput. Figure 3.3 shows the coded data rate as a function of the measurement update period and the code rate R_c. With $T_\mathrm{u} = 1\,\mathrm{ms}$ and $R_\mathrm{c} = 0.7$, a coded data rate of at least 7.3 Mbit/s is required, while in case of longer update periods (above 5 ms) the data rate is below 1.5 Mbit/s.

It is also interesting to investigate the relation between the data rate, the number of cells and the maximum number of bits that can be transmitted within one time slot. Figures 3.4 and 3.5 show the data rate results obtained with $T_\mathrm{u} = 5\,\mathrm{ms}$ and $T_\mathrm{u} = 1\,\mathrm{ms}$, respectively. The required data rate increases proportionally with the data packet length. Similarly, a linear increase of the data rate as a function of the number of cells is expected, when $T_\mathrm{g} << T_\mathrm{u} N_\mathrm{slots}$. Furthermore, a comparison of the results obtained with different measurement update rates confirms that data rates above 2 Mbit/s are required only in case the measurement update period is equal to or below 1 ms.

If $T_\mathrm{u} = 1\,\mathrm{ms}$, every additional 10 bits of the cell data result in an increase of the data rate by 2 Mbit/s, assuming 100 cells in the battery pack. Furthermore, the data rate increases by 75 kbit/s per additional cell, in case the cell data length is equal to 40 bits. However, in case the cell data length is equal to 100

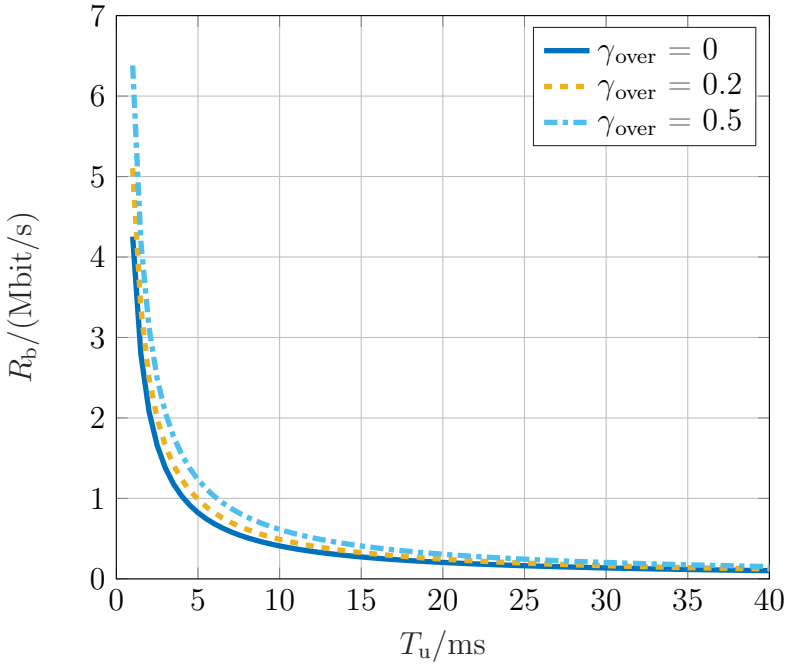

Figure 3.2: Data rate as a function of the measurement update period and the overhead factor with $N = 100$, $N_{\text{slots,pmu}} = 2$, $N_{\text{slots,cell}} = 1$ and $L_{\text{p}} = 40$ bits

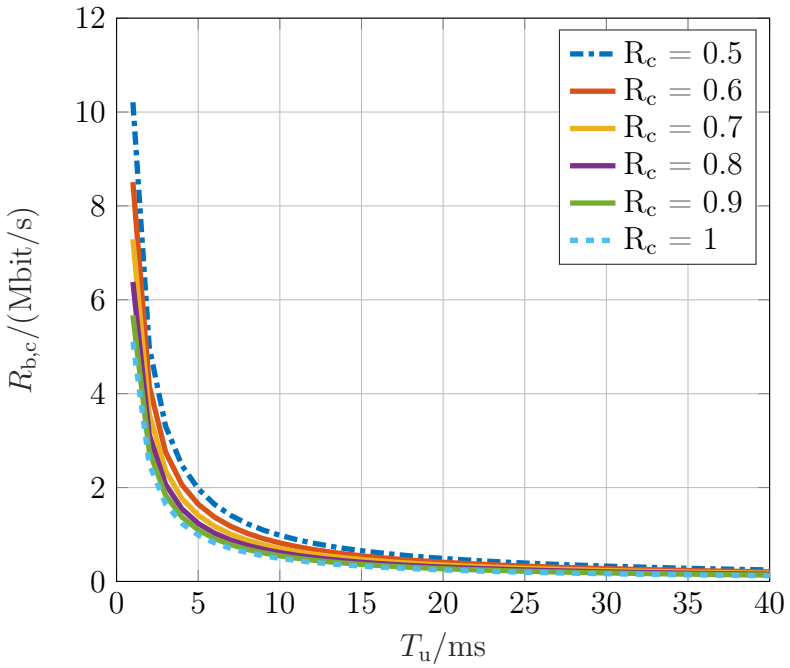

Figure 3.3: Coded data rate as a function of the measurement update period and the code rate with $N = 100$, $N_{\text{slots,pmu}} = 2$, $N_{\text{slots,cell}} = 1$, $L_{\text{p}} = 40$ bits and $\gamma_{\text{over}} = 0.2$

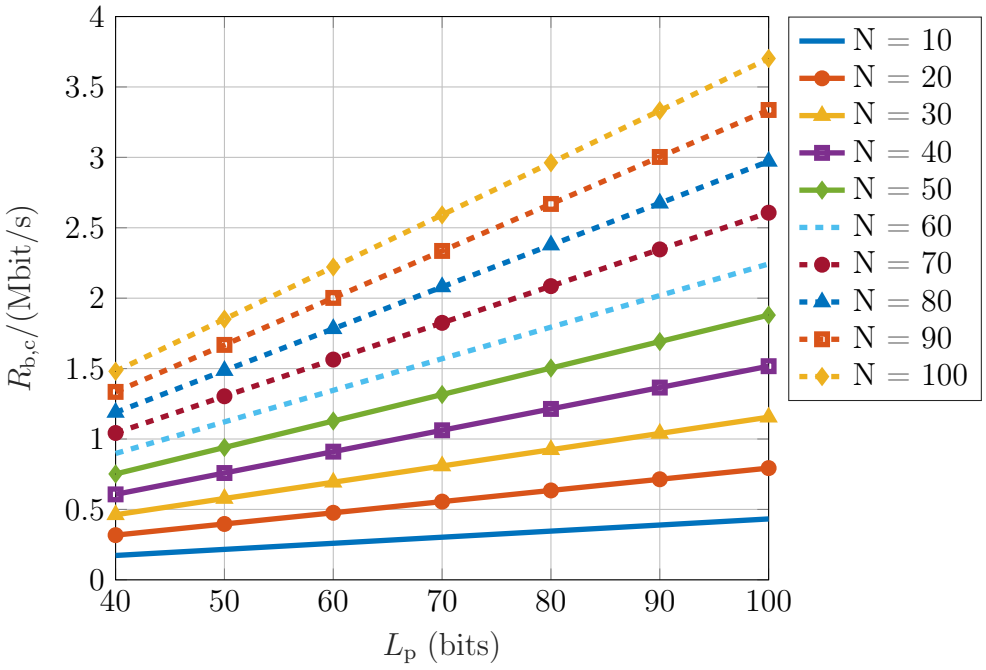

Figure 3.4: Coded data rate as a function of the number of cells and the packet payload length with $N_{\text{slots,pmu}} = 2$, $N_{\text{slots,cell}} = 1$, $\gamma_{\text{over}} = 0.2$, $R_c = 2/3$ and $T_u = 5\,\text{ms}$

bits, the expected increase of the data rate equals 200 kbit/s per additional cell. With an update period of 5 ms, the data rate increases by 50 kbit/s with each additional battery cell, assuming the cell data length is equal to 100 bits.

3.1.2.2 Different measurement update rates

In the following, we assume that there are $N_{\text{m,cell}}$ different types of cell measurements with different update rates. Let's number the cell measurements from 1 to $N_{\text{m,cell}}$ for ease of reference. Let γ_j be the ratio of $T_{u,j}$ to T_u, where $T_{u,j}$ is the update period of the j-th cell measurement with $j \in \{1, 2, \cdots, N_{\text{m,cell}}\}$, and T_u is the shortest update period among all possible measurement update periods. Assuming that one data packet is sent per CMU per cell measurement to the PMU, the number of time slots reserved to the CMUs per communication cycle is given by

$$N_{\text{slots,cells}} = \begin{cases} \sum_{j=1}^{N_{\text{m,cell}}} \left\lceil \frac{N}{\gamma_j} \right\rceil, & L_d > L_p \\ N, & \text{otherwise} \end{cases} \tag{3.6}$$

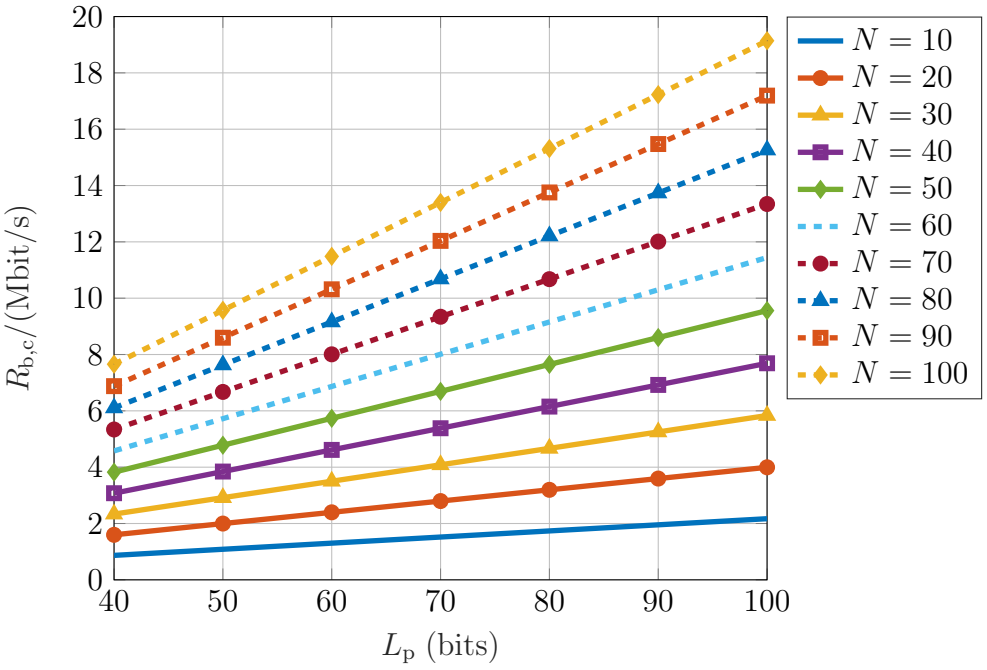

Figure 3.5: Coded data rate as a function of the number of cells and the packet payload length with $N_{\text{slots,pmu}} = 2$, $N_{\text{slots,cell}} = 1$, $\gamma_{\text{over}} = 0.2$, $R_c = 2/3$ and $T_u = 1\,\text{ms}$

where $\lceil x \rceil$ denotes the least integer greater than or equal to x. In (3.6), it is shown that if the maximum cell data length is smaller or equal to the longest data packet, a communication cycle has as many time slots for the CMUs as cells. In this case the data rate is determined by the shortest update period of the cell measurements and can be calculated from (3.5). If, however, the cell data does not completely fit in one data packet, the number of cell data packets per communication cycle is determined by the number of cells and the update rates of the cell measurements. In this case the CMUs do not necessarily have an equal number of time slots within a communication cycle. The PMU receives an update of the measurement with the shortest update period, in every communication cycle and from every CMU. Measurements with longer update periods are updated less frequently. As a consequence, a communication frame with $\kappa = \max_j(\gamma_j)$ communication cycles is needed in order to send all the data required from the CMUs.

The communication frame has a fixed schedule that is repeated periodically. Table 3.2 shows an example of a communication frame with four cycles in case

Communication Cycle	Voltage	Temperature	Pressure
1	1 – 100	1–50	1–25
2	1 – 100	51–100	26–50
3	1 – 100	1–50	51–75
4	1 – 100	51–100	76–100

Table 3.2: Communication frame with four communication cycles and three types of cell measurements with the update periods $T_{\mathrm{u,v}} = T_{\mathrm{u}}$, $T_{\mathrm{u,t}} = 2T_{\mathrm{u}}$ and $T_{\mathrm{u,p}} = 4T_{\mathrm{u}}$ (100 cells)

of a battery pack with 100 cells. The cell voltage, temperature and pressure have the update periods $T_{\mathrm{u,v}} = T_{\mathrm{u}}$, $T_{\mathrm{u,t}} = 2T_{\mathrm{u}}$ and $T_{\mathrm{u,p}} = 4T_{\mathrm{u}}$, respectively. The table uses the numbers 1 to 100 to indicate which battery cells send voltage, temperature and/or pressure data packets in the communication cycles 1 to 4. This example shows that in every communication cycle 100 data packets are sent for the voltage, 50 for the temperature and 25 for the pressure, i.e. two communication cycles are required to transmit all the temperature data packets, while four cycles are required to transmit all the pressure data packets. The end of the communication frame is reached when the PMU receives the measurement update with the longest update period from the last cell in the battery pack.

In order to better understand the relation between the data rate and the measurement update periods, we consider the example of a battery system with $N = 100$ cells and $N_{\mathrm{m,cell}} = 3$. We choose $T_{\mathrm{g}} = 0.4\,\mu\mathrm{s}$, $\gamma_{\mathrm{over}} = 0.2$, $R_{\mathrm{c}} = 2/3$, $N_{\mathrm{slots,pmu}} = 4$ and $L_{\mathrm{p}} = 20$ bits. Figure 3.6 shows the coded data rate obtained with these parameter values as a function of γ_{t} and γ_{p} ($\gamma_{\mathrm{v}} = 1$) with update periods between 5 ms and 40 ms in the case where $T_{\mathrm{u}} = 5\,\mathrm{ms}$. As can be seen, the required data rate is below 2.4 Mbit/s. In case, however, $T_{\mathrm{u}} = 1\,\mathrm{ms}$, the minimum required data rate is expected to be between 8 Mbit/s and 12.5 Mbit/s, when only one measurement out of three has an update period longer than T_{u}. This is shown in Figure 3.7. When two measurements out of three have update periods above 5 ms, the data rate is between 4 Mbit/s and 5.5 Mbit/s.

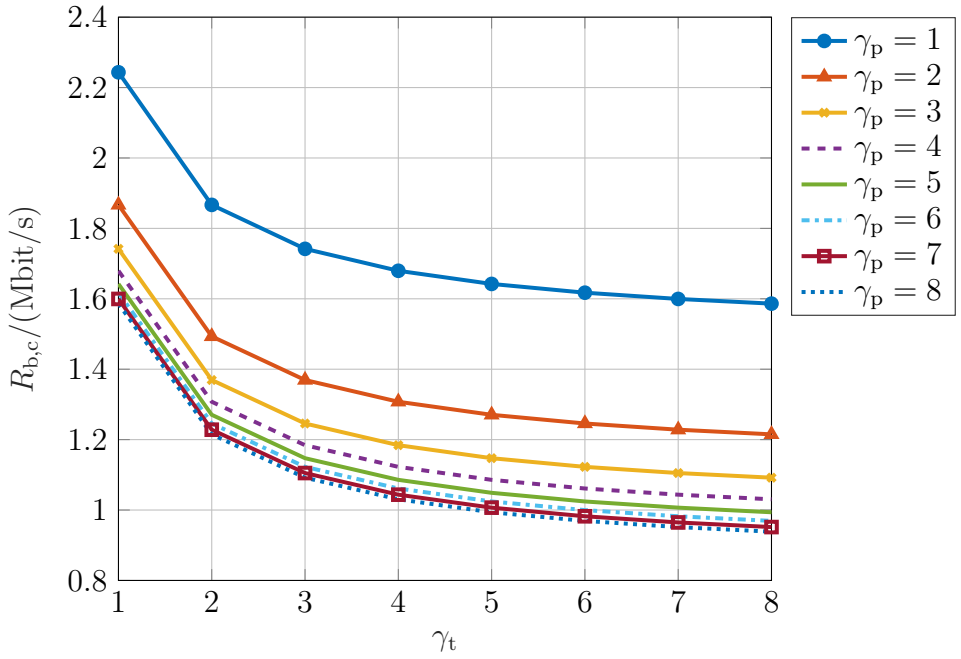

Figure 3.6: Coded data rate as a function of γ_t and γ_p ($\gamma_v = 1$, $T_u = 5\,\text{ms}$) with $N = 100$, $N_{\text{slots,pmu}} = 4$, $L_p = 20\,\text{bits}$, $\gamma_{\text{over}} = 0.2$ and $R_c = 2/3$

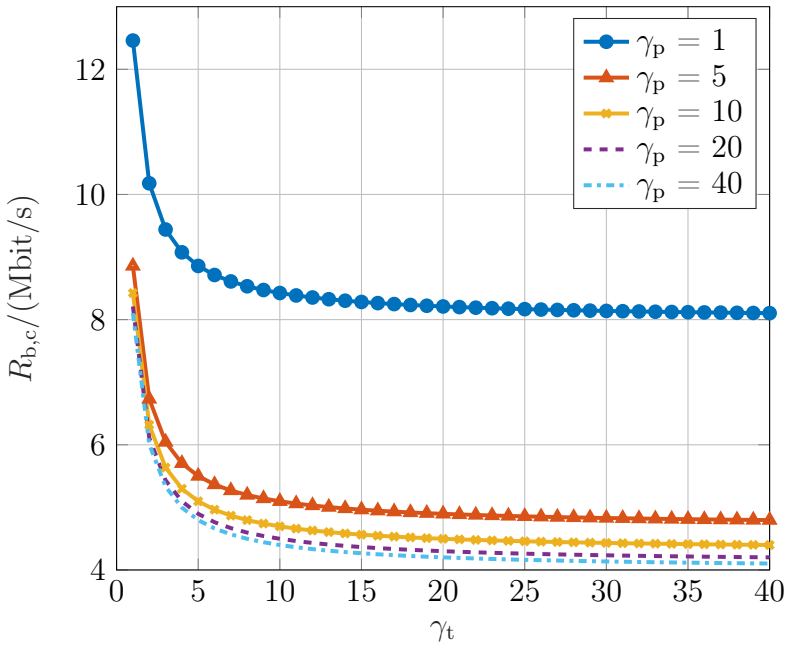

Figure 3.7: Coded data rate as a function of γ_t and γ_p ($\gamma_v = 1$, $T_u = 1\,\text{ms}$) with $N = 100$, $N_{\text{slots,pmu}} = 4$, $L_p = 20\,\text{bits}$, $\gamma_{\text{over}} = 0.2$ and $R_c = 2/3$

3.2 Radio frequency properties of battery cells

This section deals with the characterization of the RF properties of lithium-ion battery cells, based on impedance measurements conducted in the frequency range 1 MHz to 100 MHz. There are many different methods for measuring the AC impedance. In general, the choice of the measurement method and the impedance measuring instrument is made based on the required frequency range, accuracy and impedance measurement range.

3.2.1 Choice of the measurement method

The auto-balancing bridge method offers high accuracy across a very wide range of impedance values in the frequency range 20 Hz to 110 MHz. In comparison, the RF current-voltage (I-V) method is recommended in the frequency range 110 MHz to 3 GHz as it has a higher accuracy and provides a wider measurement range. For measurements at higher frequencies, the network analysis method can be used [47].

We opt for the auto-balancing bridge method because of its high accuracy in the frequency range 1 MHz to 100 MHz. This method determines the complex impedance of the device under test (DUT) by measuring the voltage applied to it and the current flowing through it as shown in Figure 3.8. It balances the current flowing through the DUT with the one flowing through the range resistor R_r, while maintaining the electrical potential at the output of the DUT at zero volts (virtual ground) [47].

There are several terminal configurations that can be applied to interconnect the DUT with the test ports of the measurement instrument (conventionally named UNKNOWN terminals) [47]. We choose the four-terminal (4T) configuration, which uses four cables, two as current path leads and two as voltage sensing leads. When separating the current and voltage sensing leads from each other, the signal current scarcely flows through the voltage sensing leads. This reduces the effect of lead impedances and contact resistances and, thus, improves the accuracy, especially in case of low impedance measurements. Impedances down to 10 mΩ can be accurately measured.

A compensation of the effect of the test cables used to extend the UNKNOWN terminals is required. The compensation does not completely remove the error.

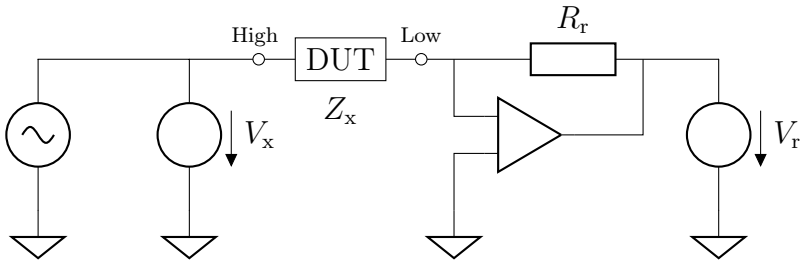

Figure 3.8: Simplified circuit model of the auto-balancing bridge method [47]

Thus, the measurement accuracy obtained after compensation is not as good as that obtained at the calibration plane [47]. The commonly used compensation techniques are open/short compensation, open/short/load compensation and cable length correction.

3.2.2 Impedance characterization

The impedance measurements are performed using a precision impedance analyzer designed for measurements in the frequency range 40 Hz to 110 MHz with a basic measurement accuracy of 0.08%. At first, we use dummy prismatic 40 Ah lithium-ion battery cells to measure the impedance of different cell components such as the top cap, the external case and the current collectors. More details on the battery cell structure can be found in Section 2.1.2.
The dummy cells have almost the same dimensions as commercial 40 Ah cells ($L \times H \times T = 173\,\text{mm} \times 115\,\text{mm} \times 32\,\text{mm}$). Based on the measurement results, we create lumped circuit models with empirically determined parameters. In a further step, we measure the impedance of 40 Ah and 60 Ah lithium-ion battery cells. Finally, the impedance of a series connection of up to six 40 Ah battery cells is measured. The results are presented and discussed in the following sections.

3.2.2.1 Cell components

We model the measurement wires used for voltage sensing as a pair of parallel wires, where $L_i = 6\,\text{nH}$ is the internal inductance, $L_e = 172\,\text{nH}$ is the external inductance, $C = 0.6\,\text{pF}$ is the external capacitance and $R_{dc} = 6\,\text{m}\Omega$ is the internal resistance. L_e can be assigned to either wire in the loop and is in series

with L_i [48]. In case of a circular wire, R_dc is calculated as

$$R_\mathrm{dc} = \frac{l}{\sigma \pi r_\mathrm{w}^2}, \tag{3.7}$$

where r_w is the radius, σ is the conductivity and l is the total length of the wire. The external capacitance is calculated from the open-circuit impedance. It can also be determined analytically. The external capacitance C' per unit length is the ratio of the charge on the wires per unit length to the voltage between them. C' is a function of the wire radius r_w and the distance s between the wires and can be expressed as

$$C' = \frac{Q}{lV} = \frac{\pi \epsilon_0}{\ln(s/r_\mathrm{w})}, \quad \text{with} \quad \epsilon_0 = 8.85 \times 10^{-12}\ \mathrm{F/m}. \tag{3.8}$$

The internal inductance L_i can only be calculated analytically. The low frequency internal inductance $L'_\mathrm{i,lf}$ per unit length is given by

$$L'_\mathrm{i,lf} = \frac{\mu_0}{8\pi}, \quad \text{for} \quad r_\mathrm{w} << \delta, \tag{3.9}$$

while the internal high frequency inductance $L'_\mathrm{i,hf}$ per unit length can be expressed as

$$L'_\mathrm{i,hf} = \frac{e\sigma}{r_\mathrm{w}} L'_\mathrm{i,lf} = \frac{1}{4\pi r_\mathrm{w}} \sqrt{\frac{\mu_0}{\pi \sigma f}}, \quad \text{for} \quad r_\mathrm{w} >> \delta. \tag{3.10}$$

In (3.9) and (3.10), δ refers to the skin depth given by

$$\delta = \frac{1}{\sqrt{\pi f \mu_0 \sigma}} = \frac{6.6 \times 10^{-2}}{\sqrt{f}}. \tag{3.11}$$

The loop inductance L_loop, which is equal to $(L_\mathrm{e} + 2L_\mathrm{i})$, is calculated from the impedance measured under short circuit. The external inductance is approximately frequency independent. In comparison, the internal inductance is proportional to the inverse square root of the frequency and can be, therefore, neglected [48].

Figure 3.9 shows the measurement and simulation results obtained for the impedance of the top cap (DUT1) of a dummy 40 Ah battery cell, the top cap with attached current collectors (DUT2) and the whole cell without the *jelly roll* (DUT3). Based on the measurements, it is obvious that the complex-valued impedance of a hollow battery cell (without the *jelly roll*) is dominantly capacitive for frequencies below the resonant frequency. For higher frequencies,

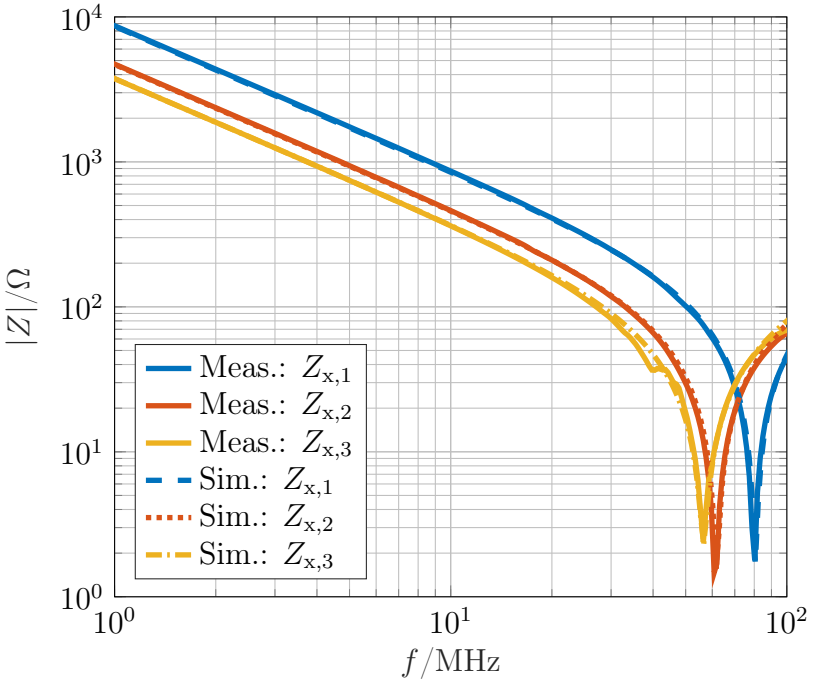

Figure 3.9: Measurement versus simulation results of the impedance Z_{x} of DUT1, DUT2 and DUT3

the impedance becomes dominantly inductive. In order to obtain the same impedance behaviour, DUT1, DUT2 and DUT3 can be represented by lumped circuit models that are based on series RLC circuits, as shown in the figures 3.10, 3.11 and 3.12, respectively. In all these figures, Z_{x} denotes the impedance measured before compensation, i.e. before de-embedding the effect of the measurement lines, while Z_{DUT} refers to the impedance of the associated DUT. It should be noted that the circuit models are built upon each other, i.e. the circuit model of DUT3 is based on the circuit model of DUT2, which in turn is obtained from the circuit model created for DUT1. The circuit parameters listed in Table 3.3 are empirically determined using simulation-based model fitting.

In a next step, we measure the impedance of a dummy 40 Ah battery cell without an electrolyte (DUT4) and create the circuit model shown in Figure 3.13, which considers the effect of the *jelly roll* on the overall cell impedance. The measured and simulated results are presented in Figure 3.14. As can be seen, the impedance of a battery cell without an electrolyte has a dominant inductive reactance, at least for frequencies above 1 MHz.

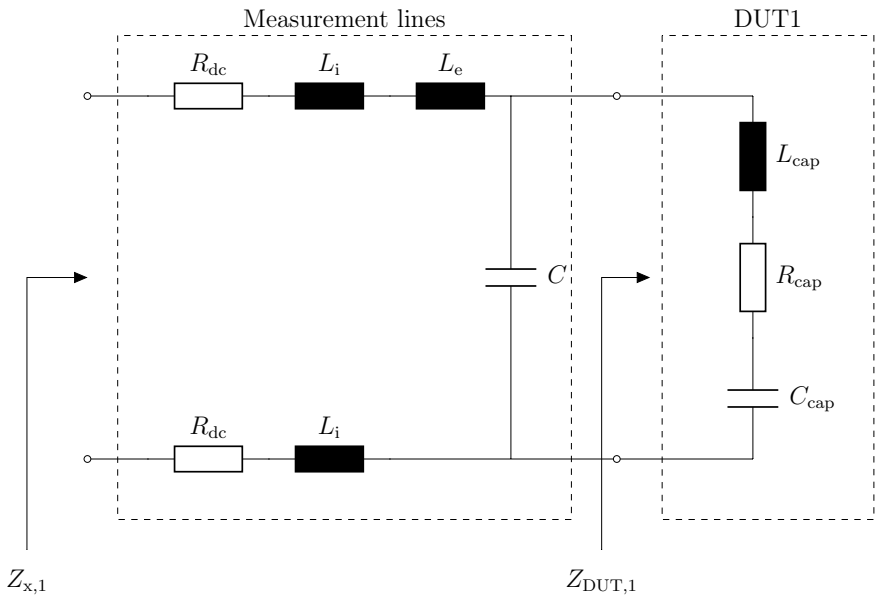

Figure 3.10: Lumped circuit model of the top cap (DUT1) of a dummy 40 Ah battery cell

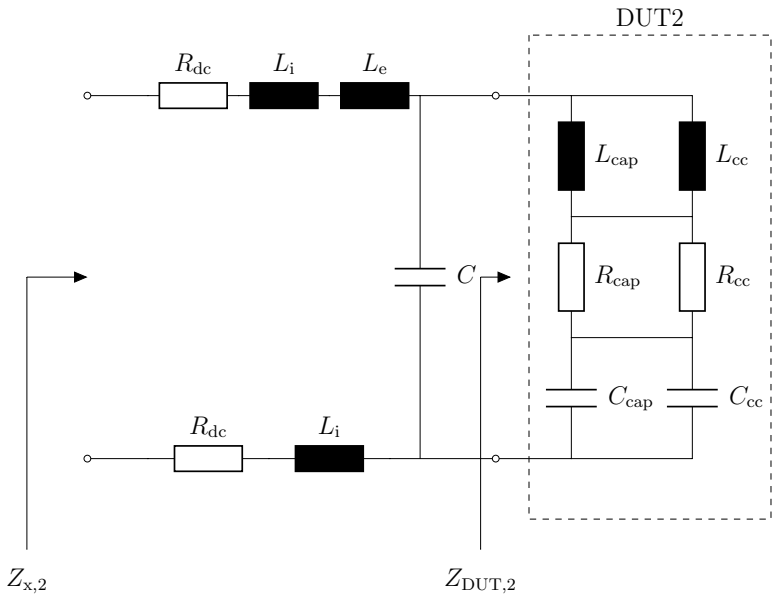

Figure 3.11: Lumped circuit model of the top cap of a dummy 40 Ah battery cell with attached current collectors (DUT2)

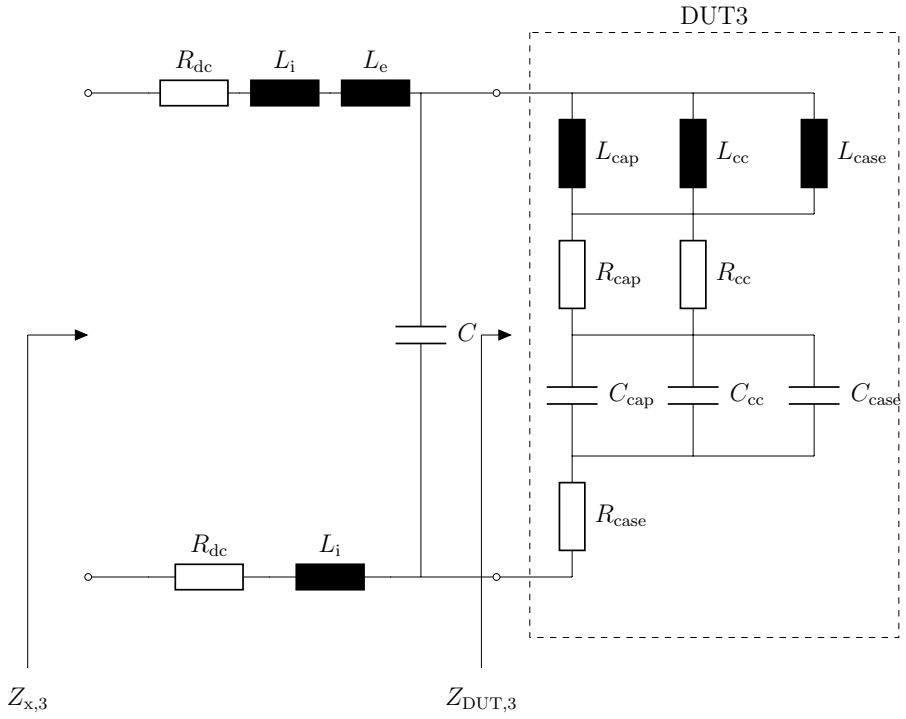

Figure 3.12: Lumped circuit model of a dummy 40 Ah battery cell without *jelly roll* (DUT3)

Finally, the impedance of a dummy 40 Ah battery cell as obtained from measurement and simulation is shown in Figure 3.15. The equivalent circuit model used to produce the simulation results is shown in Figure 3.16. From the measured complex impedance, we derive the equivalent inductance and obtain a value of approximately 20 nH. Furthermore, we observe that at frequencies above 25 MHz there are multiple resonances. Figure 3.15 also shows that the simulation model provides a good fit with the measurements.

3.2.2.2 Single cells

We measure the AC impedance of 40 Ah and 60 Ah battery cells. Figure 3.17 shows the absolute value of the complex impedance, while the phase is plotted in Figure 3.18. According to the obtained results, a battery cell has a dominant inductive reactance in the frequency range 1 MHz to 25 MHz. Furthermore, a 40 Ah cell has an equivalent inductance value of approximately 20 nH, compared to an inductance value of 30 nH in the case of 60 Ah battery cells.

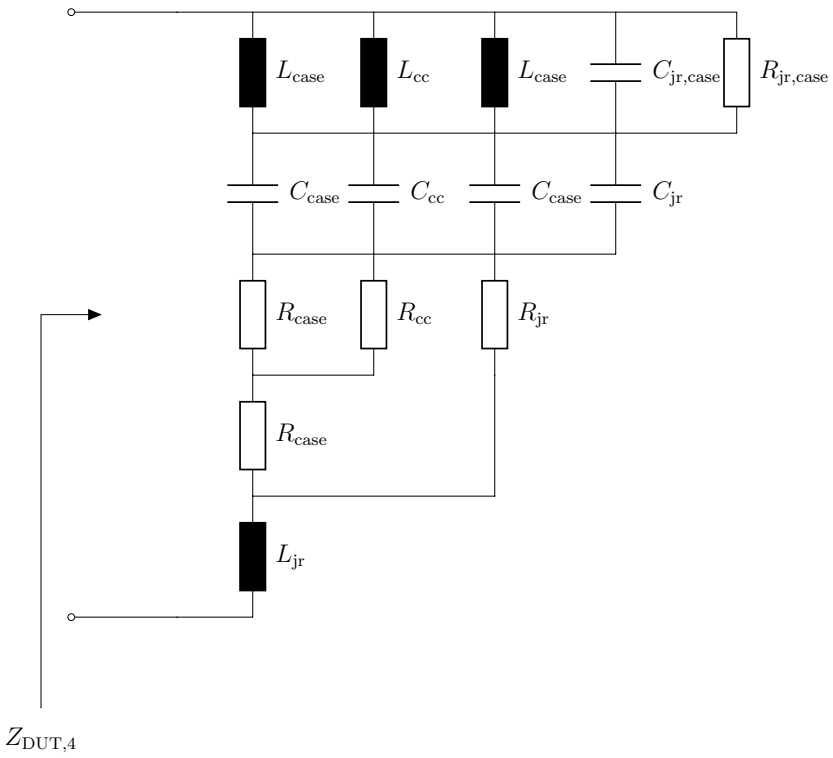

Figure 3.13: Lumped circuit model of a dummy 40 Ah battery cell without an electrolyte (DUT4)

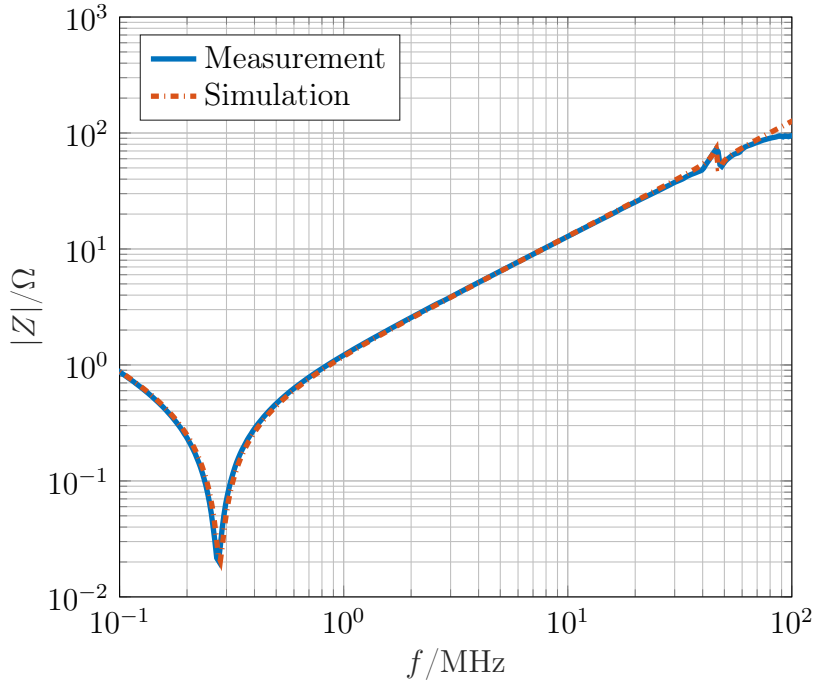

Figure 3.14: Measurement versus simulation results of the impedance Z_x of a dummy 40 Ah battery cell without an electrolyte (DUT4)

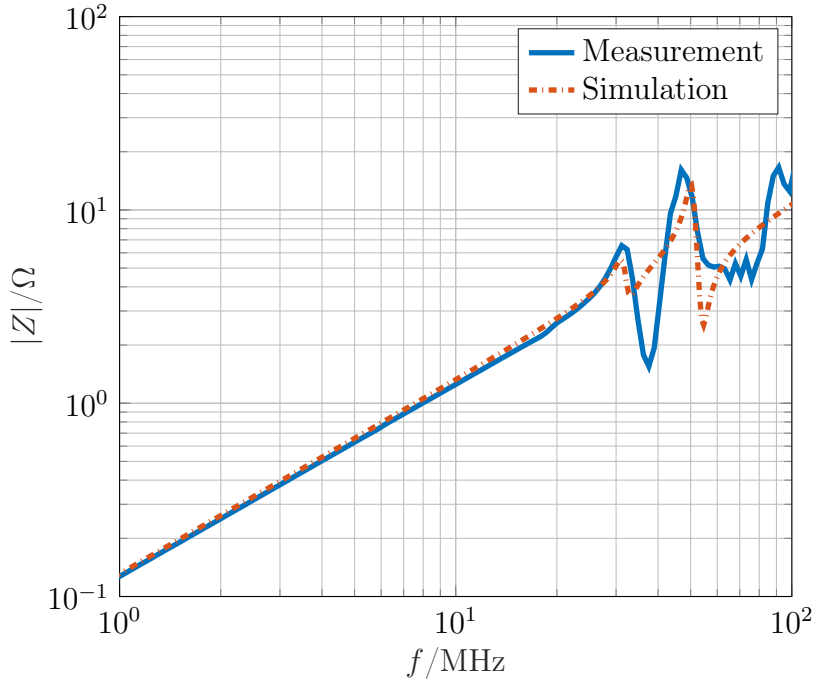

Figure 3.15: Impedance of a dummy 40 Ah battery cell as obtained from measurement and simulation

Cell Components	**Lumped Circuit Parameters**	
Top Cap	L_{cap}	28.61 nH
	R_{cap}	1.786 Ω
	C_{cap}	17.887 pF
Current Collectors	L_{cc}	20.669 nH
	R_{cc}	6 Ω
	C_{cc}	15.4 pF
External Case	L_{case}	4.216 nH
	R_{case}	1 Ω
	C_{case}	8.459 pF
Jelly Roll	L_{jr}	17.778 nH
	R_{jr}	14.5 mΩ
	C_{jr}	1.576 µF
	$R_{\text{jr,case}}$	28.75 Ω
	$C_{\text{jr,case}}$	3.775 nF
Electrolyte	L_{el}	30 nH
	$R_{\text{el,s}}$	0.5 Ω
	C_{el}	0.7 nF
	$R_{\text{el,p}}$	30 Ω
	$C_{\text{el,jr}}$	10 µF

Table 3.3: Parameters of the lumped circuits used to model the cell components in the frequency range 1 MHz to 100 MHz

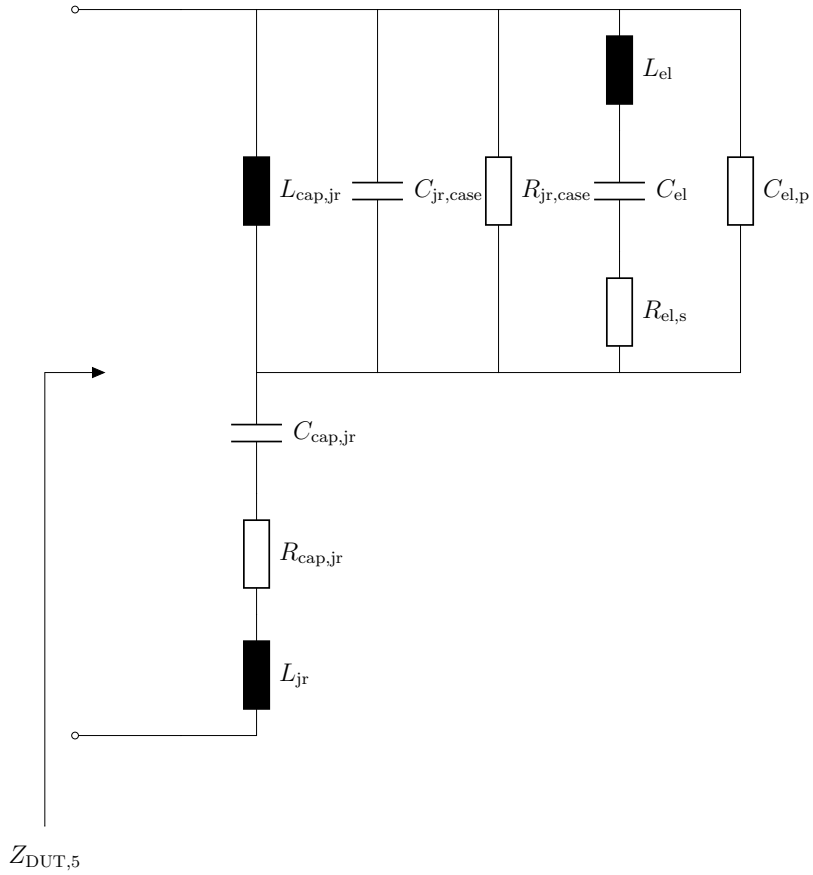

Figure 3.16: Equivalent circuit model of a dummy 40 Ah battery cell: $L_{\mathrm{cap,jr}}$ results from the parallel connection of L_{cap}, L_{case} and L_{cc}. $C_{\mathrm{cap,jr}}$ results from the parallel connection of C_{cap}, C_{cc}, C_{case} and C_{jr}. R_{cov} is a function of R_{cap}, R_{cc}, R_{case} and R_{jr}

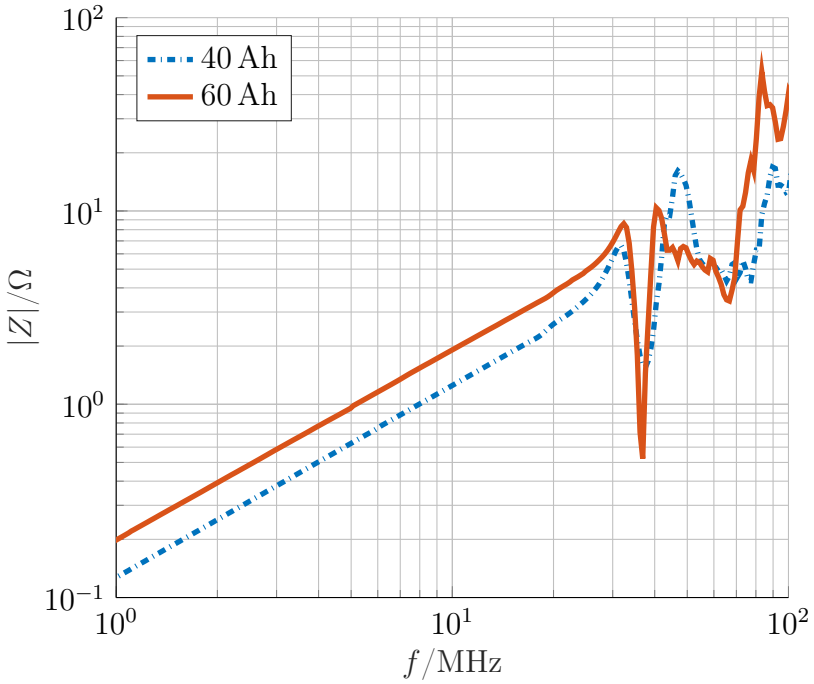

Figure 3.17: Magnitude of the impedance of 40 Ah and 60 Ah battery cells

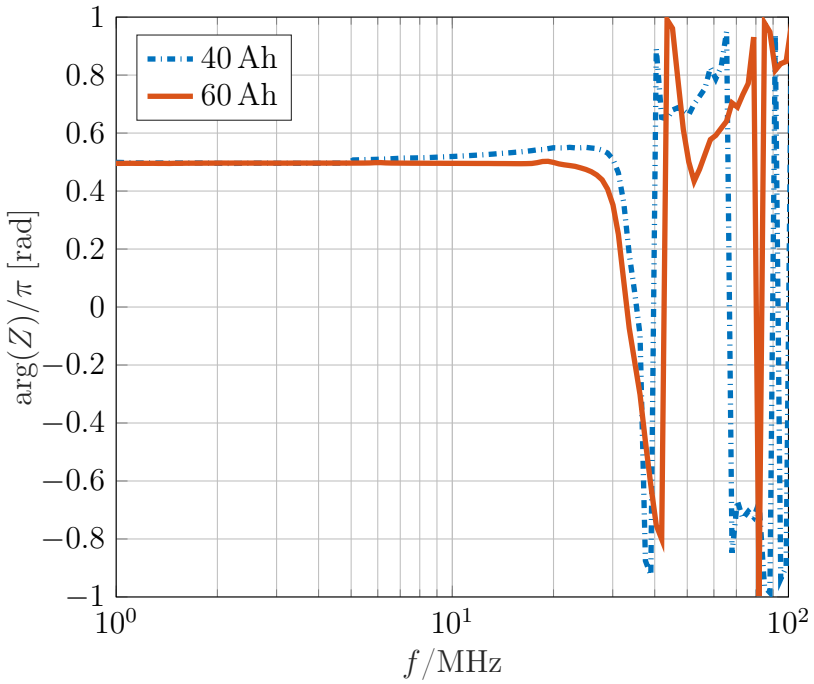

Figure 3.18: Phase of the impedance of 40 Ah and 60 Ah battery cells

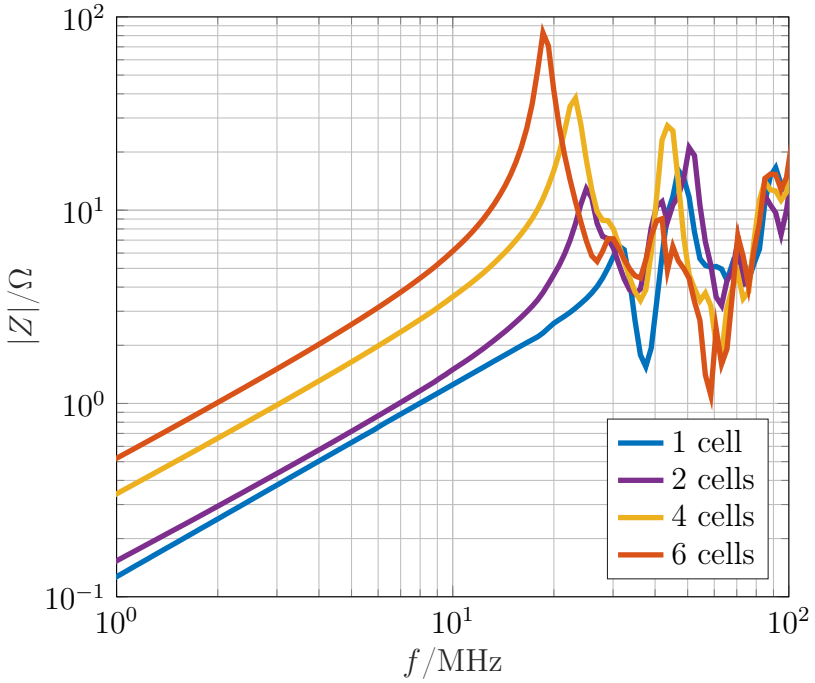

Figure 3.19: Impedance of a series connection of two, four and six 40 Ah battery cells

3.2.2.3 Cells connected in series

The impedance of a series connection of two, four and six 40 Ah cells is measured. The measurement results are shown in Figure 3.19. Two in series connected cells have an equivalent inductance value of approximately 24 nH, which is much less than twice the inductance of one battery cell. When four battery cells are connected in series, we measure an inductance value of approximately 57.29 nH. Also here we observe that the inductance value does not necessarily double when the number of cells is doubled. When six cells are connected in series, we obtain 98.67 nH for the equivalent inductance. Furthermore, strong impedance resonances are observed at frequencies higher than 25 MHz. The resonance frequencies move towards lower frequencies when the number of cells increases, probably due to higher inductance. At the same time the resonance peaks increase in magnitude. This gives a first indication on how challenging it can be to model battery cells and battery cell connections in the HF range, especially when dealing with large scale battery packs.

3.3 Channel characterization

We assume that the PLC channel can be modeled as a two-port network, where the input port is determined by the plus and minus terminals of the battery pack and the output port is determined by the plus and minus terminals of the battery cell for which the PLC channel is measured. We opt for the S-parameters to characterize the channel properties, mainly because S-parameter measurements are less prone to error and easier to conduct in the HF range, compared to other measurement types such as impedance and admittance measurements. The S-parameter measurements do not require open and short circuit terminations. Instead, matched loads are used. The source and load impedances are configured by the network analyzer. Both are equal to the reference impedance $Z_{\text{ref}} = 50\,\Omega$. The characteristic impedance of the coaxial cables used to connect the test ports of the vector network analyzer (VNA) to the input and output of the channel is also equal to Z_{ref}. Thus, the source and load impedances match the impedance of the measurement lines.

The high voltage and high current battery pack must be galvanically isolated from the VNA in order to avoid hardware damages. We use coupling circuit boards with isolation transformers and DC blocking capacitors to connect the measurement lines to the input and output of the PLC channel. In order to obtain accurate S-parameter results, calibration and compensation are applied. The calibration accuracy depends on the calibration type, the quality of the calibration standards and the care with which the calibration is performed. The compensation is used to eliminate the effects of the measurement setup, such as the coupling circuit boards.

The incident and outgoing waves at the input and output of the PLC channel are determined by what the VNA measures at its ports. Let's assume that a_1 and b_1 are the incident and outgoing waves at the channel's input, while a_2 and b_2 are those at its output. The scattering matrix $\mathbf{S}$ relates the outgoing waves to the incoming waves by

$$\begin{bmatrix} b_1 \\ b_2 \end{bmatrix} = \mathbf{S} \cdot \begin{bmatrix} a_1 \\ a_2 \end{bmatrix}, \quad \text{with} \quad \mathbf{S} = \begin{bmatrix} S_{11} & S_{12} \\ S_{21} & S_{22} \end{bmatrix}, \tag{3.12}$$

where S_{21} is the forward transmission coefficient and S_{12} is the reverse transmission coefficient. At the input port, the input reflection coefficient Γ_{in} is

given according to [49] by

$$\Gamma_{\text{in}} = \frac{b_1}{a_1} = \frac{Z_{\text{in}} - Z_{\text{ref}}}{Z_{\text{in}} + Z_{\text{ref}}}, \tag{3.13}$$

and can be expressed as

$$\Gamma_{\text{in}} = S_{11} + \frac{\Gamma_{\text{l}} S_{12} S_{21}}{1 - \Gamma_{\text{l}} S_{22}}, \quad \text{with} \quad \Gamma_{\text{l}} = \frac{Z_{\text{l}} - Z_{\text{ref}}}{Z_{\text{l}} + Z_{\text{ref}}}, \tag{3.14}$$

where Z_{in} is the input impedance, Z_{l} is the load impedance and Γ_{l} is the reflection coefficient at the load [49]. On the other hand, the output reflection coefficient Γ_{out} is given by

$$\Gamma_{\text{out}} = \frac{b_2}{a_2} = \frac{Z_{\text{out}} - Z_{\text{ref}}}{Z_{\text{out}} + Z_{\text{ref}}}, \tag{3.15}$$

and can be expressed as

$$\Gamma_{\text{out}} = S_{22} + \frac{\Gamma_{\text{s}} S_{12} S_{21}}{1 - \Gamma_{\text{s}} S_{22}}, \quad \text{with} \quad \Gamma_{\text{s}} = \frac{Z_{\text{s}} - Z_{\text{ref}}}{Z_{\text{s}} + Z_{\text{ref}}}, \tag{3.16}$$

where Z_{out} is the output impedance, Z_{s} is the source impedance and Γ_{s} is the reflection coefficient at the source [49]. Based on (3.14), S_{11} is equal to Γ_{in} for $a_2 = 0$. Similarly, S_{22} is equal to Γ_{out} for $a_1 = 0$. Let I_1 be the current flowing into the channel, I_2 be the current flowing out of the channel, V_1 be the voltage at the input port and V_2 be the voltage at the output port. Then the incident and outgoing waves can be expressed as

$$a_1 = \frac{V_1 + Z_{\text{ref}} \cdot I_1}{2 \cdot \sqrt{Z_{\text{ref}}}}, \qquad a_2 = \frac{V_2 - Z_{\text{ref}} \cdot I_2}{2 \cdot \sqrt{Z_{\text{ref}}}} \tag{3.17}$$

and

$$b_1 = \frac{V_1 - Z_{\text{ref}} \cdot I_1}{2 \cdot \sqrt{Z_{\text{ref}}}}, \qquad b_2 = \frac{V_2 + Z_{\text{ref}} \cdot I_2}{2 \cdot \sqrt{Z_{\text{ref}}}}. \tag{3.18}$$

From (3.17) and (3.18), it can be inferred that $a_2 = \Gamma_{\text{l}} b_2$. Thus, we obtain

$$\frac{a_2}{a_1} = \frac{S_{21}}{\Gamma_{\text{out}} - S_{22}} = \frac{\Gamma_{\text{l}} S_{21}}{1 - \Gamma_{\text{l}} S_{22}}. \tag{3.19}$$

3.3.1 Channel attenuation

The battery pack used for the measurements is shown in Figure 3.20. The pack has eight modules connected in series. Each module has 12 cells in series. The results obtained for S_{21} and S_{12} are shown in the Figures 3.21

and 3.22, respectively. As can be seen, the forward and inverse transmission coefficients are equal. The voltage transfer function of the PLC channel is frequency-dependent and can be calculated as

$$H(f) = \frac{V_2}{V_1} \times \frac{V_1}{V_\mathrm{s}}, \tag{3.20}$$

where V_2/V_1 is the input-to-output voltage transfer function and V_1/V_s is the input-to-source voltage ratio. V_2/V_1 can be expressed as

$$\frac{V_2}{V_1} = \frac{a_2 + b_2}{a_1 + b_1} = \frac{a_2}{a_1}\left(\frac{1 + \Gamma_\mathrm{out}}{1 + \Gamma_\mathrm{in}}\right). \tag{3.21}$$

By substituting a_2/a_1 in (3.21) with its expression given in (3.19) we obtain

$$\frac{V_2}{V_1} = S_{21}\left[\frac{1 + \Gamma_\mathrm{l}}{(1 + \Gamma_\mathrm{in})(1 - \Gamma_\mathrm{l} S_{22})}\right]. \tag{3.22}$$

For the input-to-source voltage ratio we have

$$\frac{V_1}{V_\mathrm{s}} = \frac{Z_\mathrm{in}}{Z_\mathrm{in} + Z_\mathrm{s}} = \frac{(1 + \Gamma_\mathrm{in})(1 - \Gamma_\mathrm{s})}{2(1 - \Gamma_\mathrm{in}\Gamma_\mathrm{s})}. \tag{3.23}$$

Substituting (3.22) and (3.23) in (3.20) yields

$$H(f) = \frac{V_2}{V_\mathrm{s}} = \frac{S_{21}}{2}\left[\frac{(1 - \Gamma_\mathrm{s})(1 + \Gamma_\mathrm{l})}{(1 - \Gamma_\mathrm{s} S_{11})(1 - \Gamma_\mathrm{l} S_{22}) - \Gamma_\mathrm{s}\Gamma_\mathrm{l} S_{12} S_{21}}\right]. \tag{3.24}$$

Under the assumption that the PLC transceivers have standard 50 Ω input and output impedances, it can be inferred that $H(f)$ is equal to $S_{21}/2$ and the PLC channel is reciprocal. The channel attenuation obtained in this case is given in Figure 3.23 for some battery cells. Based on the attenuation level and the frequency-dependent character of the channel, we can divide the frequency range into smaller bands with particular characteristics. For instance, in the frequency range from 1 MHz to 40 MHz, a strong frequency dependency is observed and the attenuation varies between 25 dB and 80 dB. In the frequency range from 40 MHz to 70 MHz, the frequency response is smoother and less peaks and notches can be observed. The attenuation varies between 20 dB and 40 dB and is, thus, not as high as in the lower frequency range. At higher frequencies, the frequency response changes rapidly as a function of the frequency and the attenuation tends to be high. Based on these observations, the frequency range from 40 MHz to 70 MHz seems to be better suited for a robust and power efficient data transmission than the other frequency ranges (assuming AWGN).

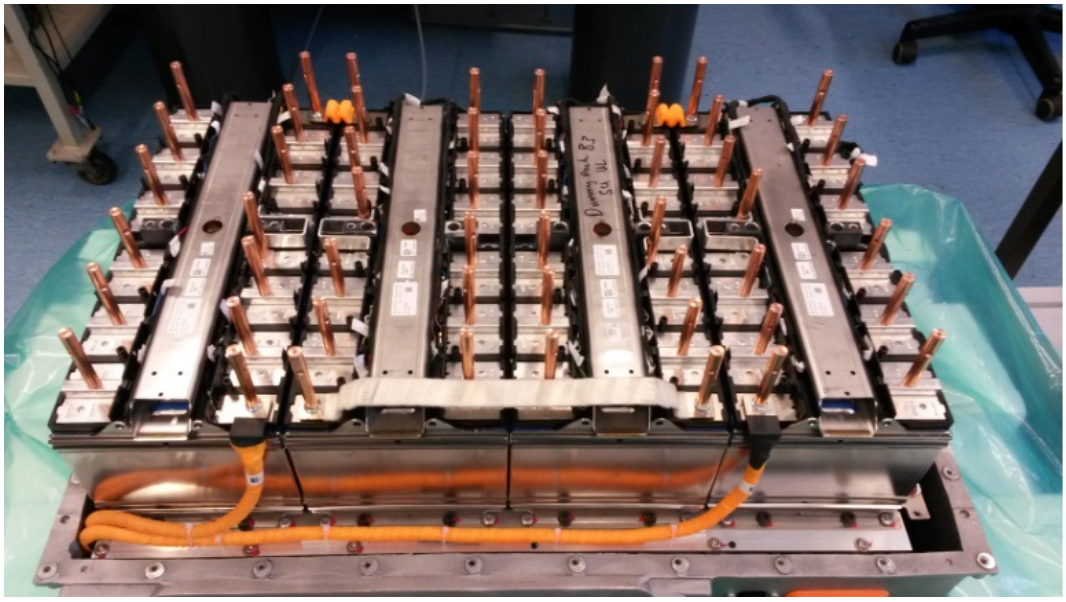

Figure 3.20: Battery pack used for S-parameter measurements

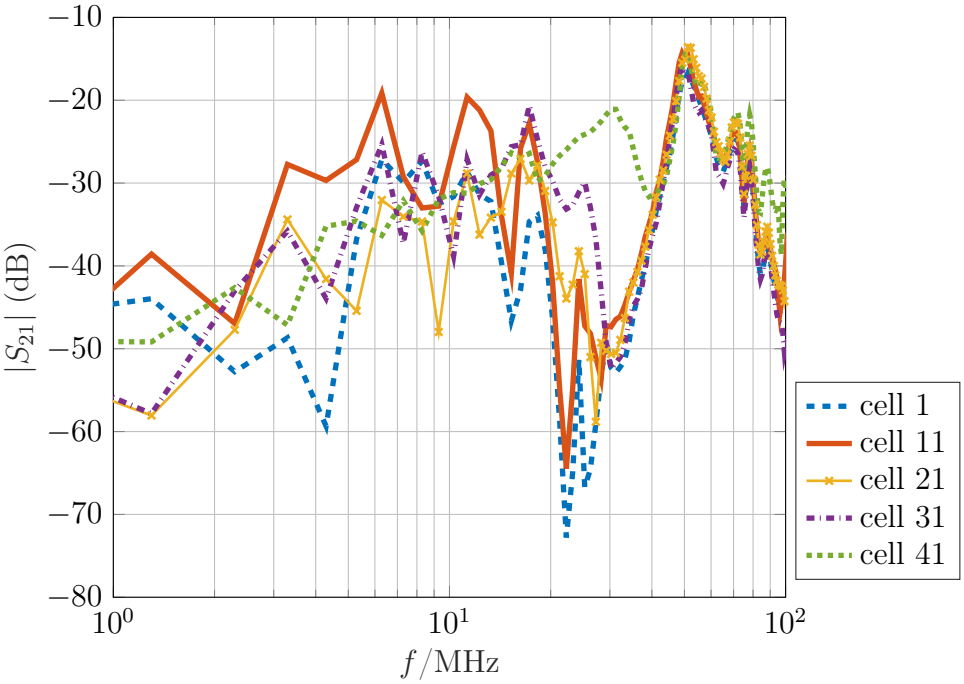

Figure 3.21: Measurement results obtained for S_{21}

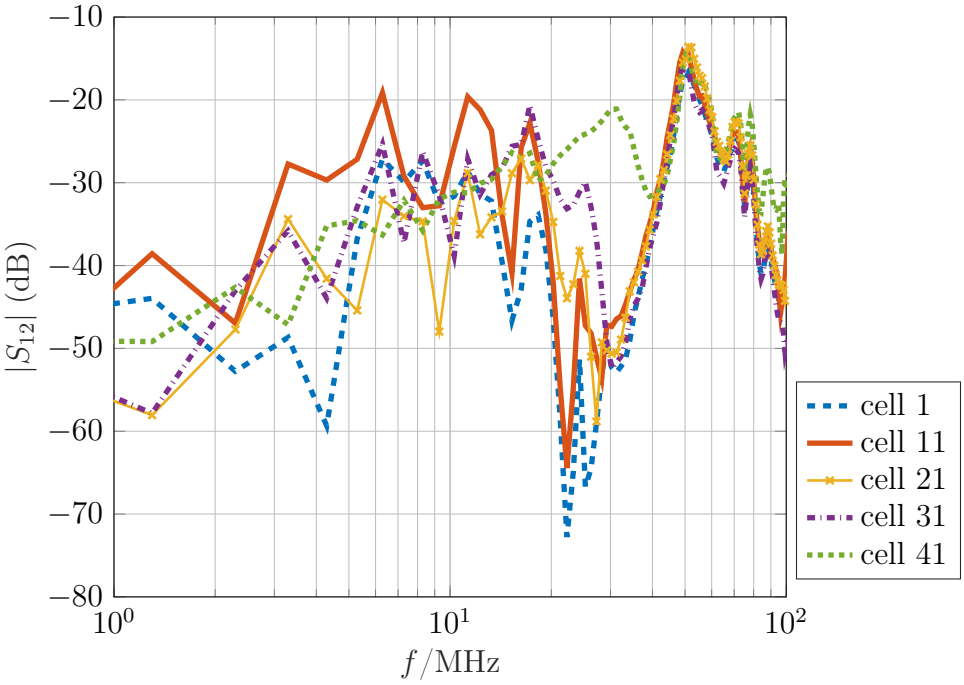

Figure 3.22: Measurement results obtained for S_{12}

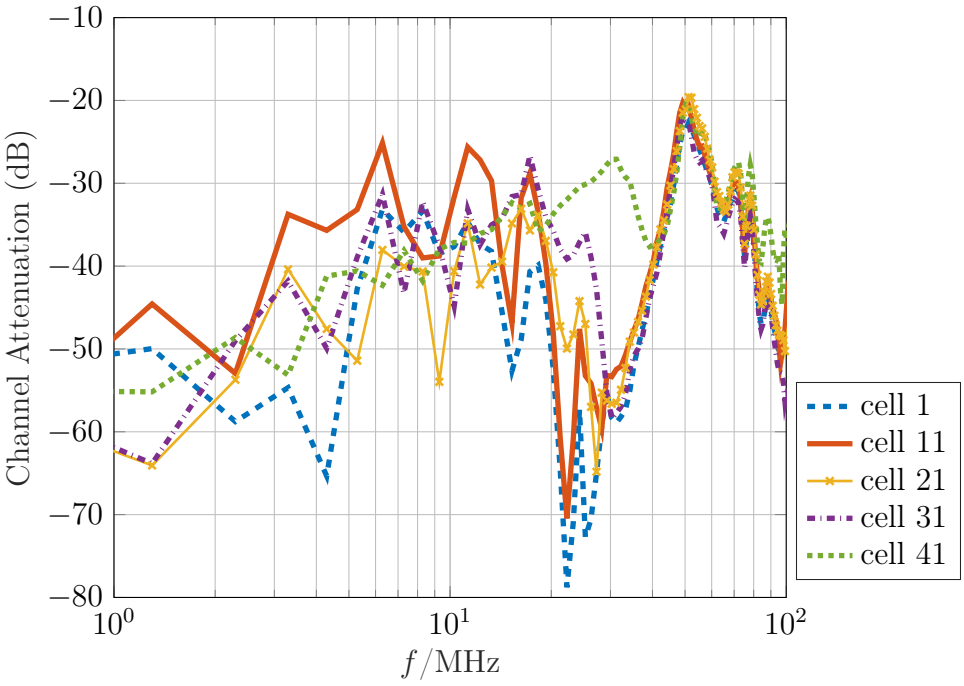

Figure 3.23: Channel attenuation assuming PLC transceivers with standard 50 Ω input and output impedances

3.3.2 Impedance matching

The Z-parameter matrix of a two-port network relates the port voltages to the port currents as follows:

$$\begin{bmatrix} V_1 \\ V_2 \end{bmatrix} = \mathbf{Z} \cdot \begin{bmatrix} I_1 \\ I_2 \end{bmatrix}, \quad \text{with} \quad \mathbf{Z} = \begin{bmatrix} Z_{11} & Z_{12} \\ Z_{21} & Z_{22} \end{bmatrix}, \tag{3.25}$$

where $Z_{nm} = V_n/I_m$ for $I_k = 0$ and $k \neq m$. Z_{11} is the input impedance obtained when the output port is open, Z_{22} is the output impedance obtained when the input port is open, Z_{21} is the input transfer impedance and Z_{12} is the output transfer impedance. In case the load and source impedances are both equal to the reference impedance, the Z-parameters can be derived from the S-parameters as follows:

$$Z_{11} = \frac{(1 + S_{11})(1 - S_{22}) + S_{12}S_{21}}{\Delta S} Z_{\text{ref}}, \tag{3.26}$$

$$Z_{21} = \frac{2S_{21}}{\Delta S} Z_{\text{ref}} \quad , \quad Z_{12} = \frac{2S_{12}}{\Delta S} Z_{\text{ref}}, \tag{3.27}$$

$$Z_{22} = \frac{(1 - S_{11})(1 + S_{22}) + S_{12}S_{21}}{\Delta S} Z_{\text{ref}}, \tag{3.28}$$

where $\Delta S = (1 - S_{11})(1 - S_{22}) - S_{12}S_{21}$ [50]. Based on the previous S-parameter results, the two-port network used to represent the PLC channel is reciprocal. Thus, Z_{21} and Z_{12} are equal. In Figure 3.24, Z_{21} is given in magnitude for different battery cells. We can see that the input transfer impedance strongly varies as a function of the frequency with values between 0.01 Ω and 100 Ω. Multiple peaks and notches can be seen across the entire frequency range. For frequencies above 40 MHz the impedance tends to be higher and less dependent on the cell position in the battery pack, compared to lower frequencies. Z_{22} can be viewed as the impedance of a battery cell mounted in a battery pack. Figure 3.25 shows that Z_{22} varies in magnitude between 10 mΩ and 100 Ω. We obtain a value between 26.8 nH and 43 nH for the equivalent inductance, depending on the cell position in the battery pack. Resonance peaks can be seen across the entire frequency range, even though high peak magnitudes are only observed at frequencies above 25 MHz.

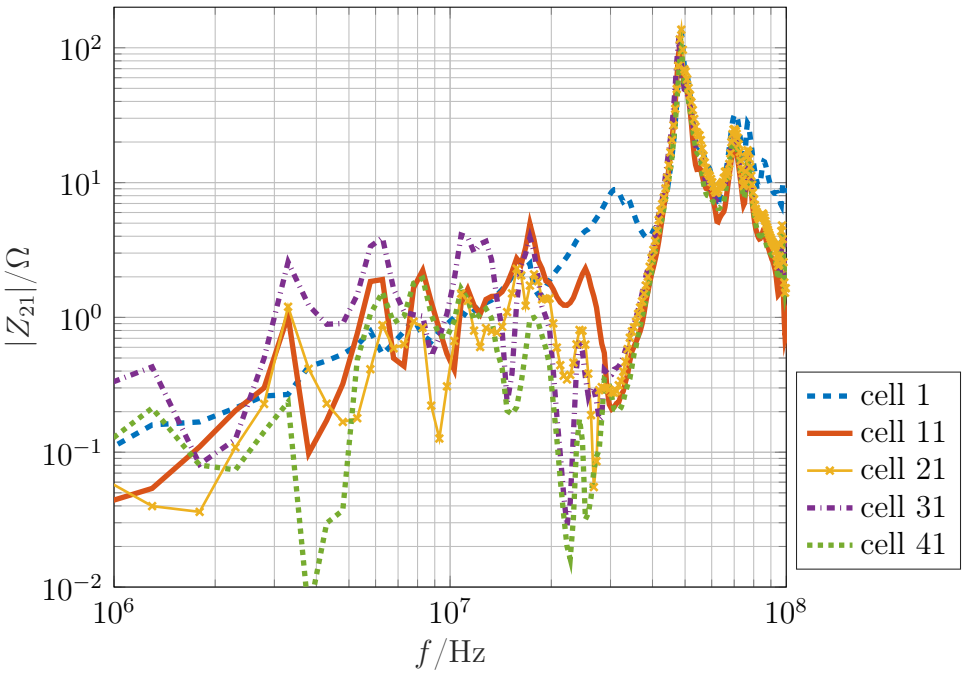

Figure 3.24: Magnitude of the channel's input transfer impedance

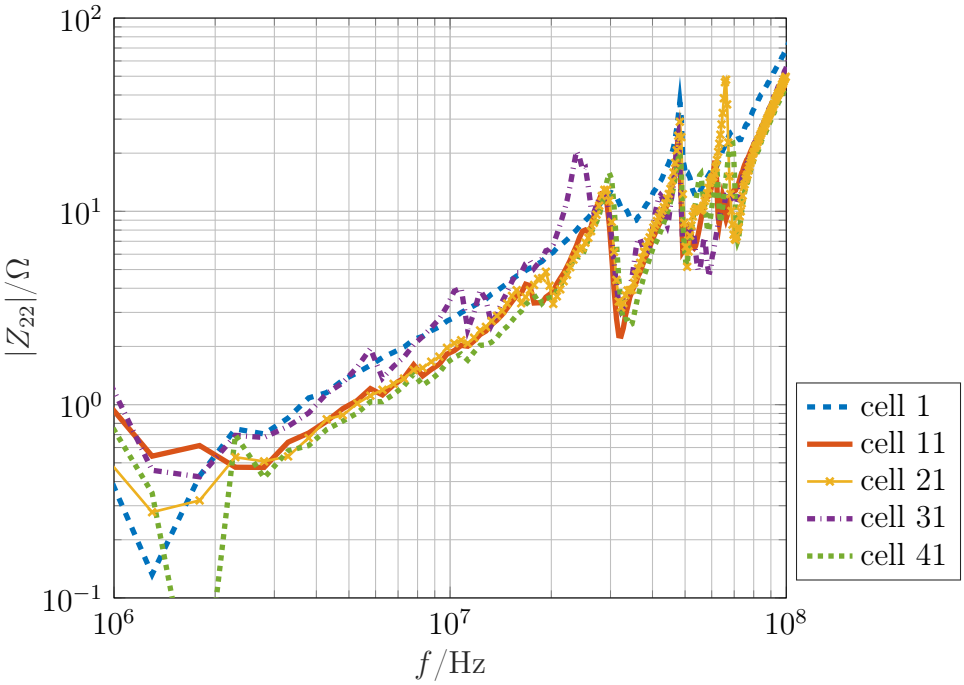

Figure 3.25: Magnitude of the channel's output impedance

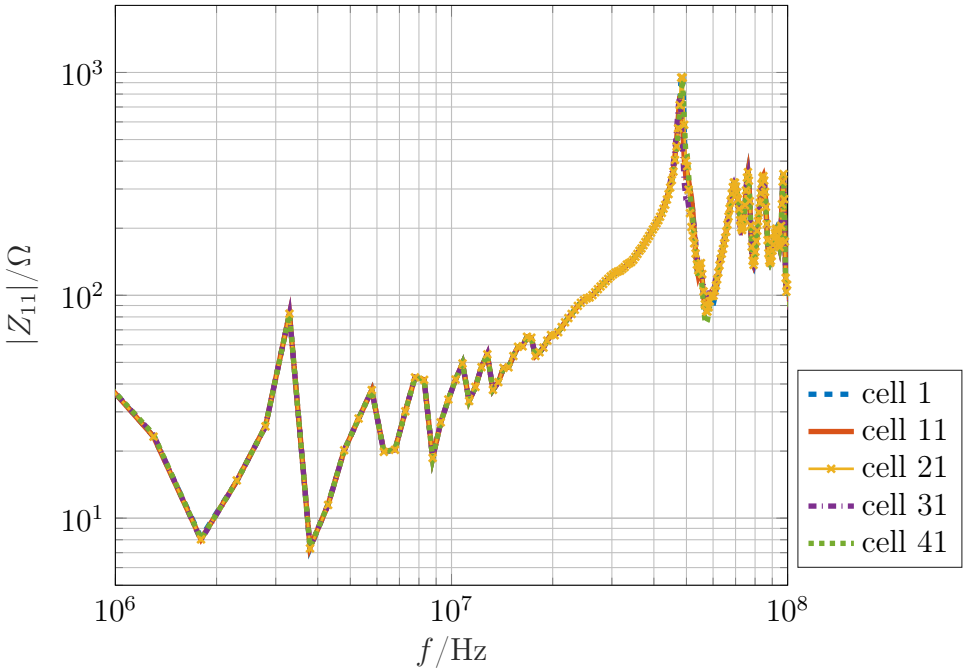

Figure 3.26: Magnitude of the channel's input impedance

The impedance of the battery pack is represented by Z_{11}, which, according to Figure 3.26, varies in magnitude between 10 Ω and 1 kΩ, depending on the frequency. Even though the impedance curves exhibit multiple resonances, we still can calculate the equivalent inductance and obtain a value of 565 nH by means of approximation. This is a rather low value considering the fact that the battery pack has 96 cells connected in series, each of which has an average inductance value of 35 nH (also based on approximations). This shows once again that modeling the battery pack is rather challenging. A pure cascade of the basic cell circuit model is probably not sufficient to obtain an accurate model of the battery pack.

Impedance matching allows to reduce signal reflections and achieve maximum power transfer. If the source impedance is matched to the input of the two-port network, we have $Z_\mathrm{s} = Z_\mathrm{in}^*$. Similarly, a matched output is obtained for $Z_\mathrm{l} = Z_\mathrm{out}^*$. The input and output impedances of the channel are given by

$$Z_\mathrm{in} = Z_{11} - \frac{Z_{12}Z_{21}}{Z_{22}+Z_\mathrm{l}} \quad \text{and} \quad Z_\mathrm{out} = Z_{22} - \frac{Z_{12}Z_{21}}{Z_{11}+Z_\mathrm{s}}. \tag{3.29}$$

Based on the measurement results, we obtain $Z_\mathrm{in} \approx Z_{11}$ and $Z_\mathrm{out} \approx Z_{22}$. Since the input and output impedances are frequency-dependent, impedance matching

is hard to realize. In order to better understand the impact of impedance mismatches on the power gain of the PLC system, we use the transducer gain. The latter measures the power delivered to the load normalized by the available power from the source. The transducer gain is the most representative measure of the power gain of a two-port network, especially because it takes into account the effects of the source and the load impedances. In terms of the Z-parameters, the transducer gain is given according to [49] as

$$G_{\mathrm{T}} = \frac{4\,\mathrm{Re}(Z_{\mathrm{s}})\,\mathrm{Re}(Z_{\mathrm{l}})|Z_{21}|^2}{|(Z_{11}+Z_{\mathrm{s}})(Z_{22}+Z_{\mathrm{l}})-Z_{12}Z_{21}|^2}, \tag{3.30}$$

where Re(.) denotes the real part of the complex impedance. In terms of the S-parameters, the transducer gain can be calculated as follows:

$$G_{\mathrm{T}} = \frac{(1-|\Gamma_{\mathrm{s}}|^2)|S_{21}|^2(1-|\Gamma_{\mathrm{l}}|^2)}{|(1-\Gamma_{\mathrm{s}}S_{11})(1-\Gamma_{\mathrm{l}}S_{22})-\Gamma_{\mathrm{s}}\Gamma_{\mathrm{l}}S_{12}S_{21}|^2}. \tag{3.31}$$

In case of the downlink, the output impedance of the transmitter in the PMU represents the source impedance, while the input impedance of the receiver in the CMU represents the load impedance. Figure 3.27 shows the transducer gain obtained for the downlink of cell Nº1 with different combinations of purely resistive source and load impedances, where impedance values between 25 Ω and 75 Ω are chosen. We can see that, in the frequency range below 30 MHz, the highest transducer gain is obtained with low source and load impedances ($Z_{\mathrm{source}} = Z_{\mathrm{load}} = 25\,\Omega$). Increasing either the source or the load impedance causes the power gain to degrade. We recall that, in the aforementioned frequency range, the input impedance of the downlink channel is between 10 Ω and 100 Ω and the output impedance is below 20 Ω. On the other hand, at frequencies above 30 MHz, the power gain increases when the source impedance is low and the load impedance is high, knowing that the channel's input impedance is above 100 Ω and its output impedance is between 1 Ω and 100 Ω. Furthermore, as shown in Figure 3.28, the load impedance should not be much higher than 100 Ω, otherwise this would have the reverse effect, i.e. the power gain would be reduced. Based on these results, we can conclude that the power gain of the channel can be improved by having a low source impedance and a load impedance which has the same order of magnitude as the channel's output impedance. Finally, it should be noted that comparable results were obtained for the PLC channels of other battery cells. Reversing the roles of the source

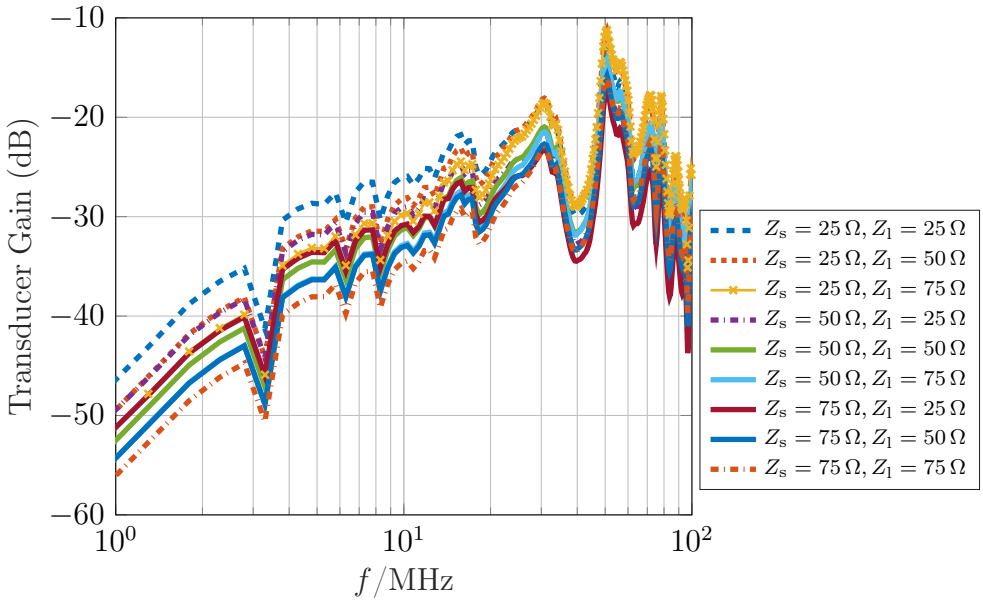

Figure 3.27: Transducer gain in the downlink as a function of the load and source impedances (cell Nº1)

and load, one can measure the transducer gain of the uplink channel in the same way.

Based on the expression given for the voltage transfer function in (3.24), the channel would not be reciprocal if the source and load impedances are different. However, we showed in Section 3.1.1 that channel reciprocity would be an advantage for TDMA/TDD. If we have a look at Figure 3.27, we can see that in case the load and source impedances are both equal to 50 Ω, the transducer gain is smaller than the maximum possible gain by up to 5 dB. Thus, a possible compromise would be to design the PLC transceivers to have standard 50 Ω input and output impedances. In the remainder of this thesis, we assume, for simplicity, that the channel is reciprocal, where $\Gamma_s = \Gamma_l = 0$ and the voltage transfer function is equal to $S_{21}/2$.

3.3.3 Impulsive noise

The noise measurements are performed in the time-domain for different driving scenarios. Figure 3.29 shows an example of a noise voltage signal measured at the input of the battery pack over a time period of 200 µs. As can be seen, the noise is predominantly impulsive. Similar results were obtained in

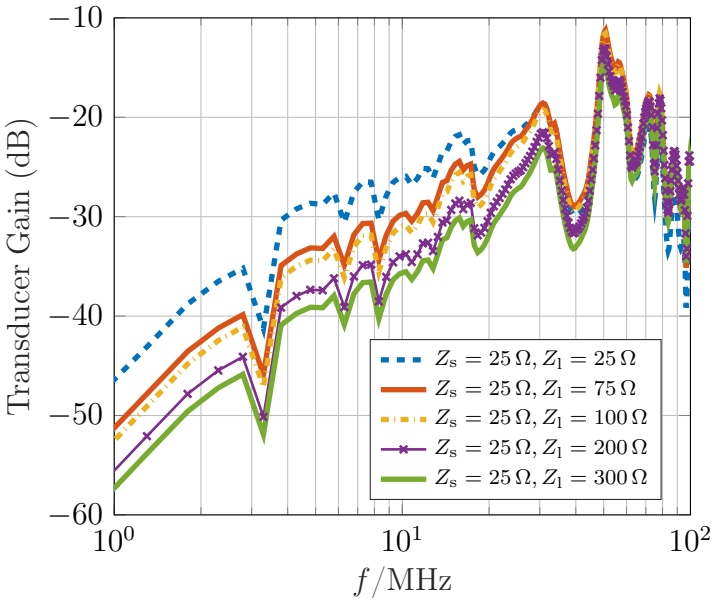

Figure 3.28: Transducer gain in the downlink as obtained with low source impedance and high load impedance (cell Nº1)

other cases, where it was clear that the noise has an impulsive character, no matter what the driving scenario is. The impulsive noise can be characterized using the following parameters: the pulse width T, the inter-arrival time between subsequent pulses τ and the pulse amplitude A. The measurement data have been extensively analyzed. A summary of the analysis results can be found in Table 3.4. We distinguish between periodic and aperiodic impulsive noise. For the pulse width, the inter-arrival time and the pulse energy, we calculate the arithmetic mean μ and the standard deviation σ defined as

$$\mu = \frac{1}{n}\sum_{i=1}^{n} x_i \qquad \text{and} \qquad \sigma = \sqrt{\frac{1}{n}\sum_{i=1}^{n}(x_i - \mu)^2}, \tag{3.32}$$

where n denotes the number of pulses over a specific period of time. Based on the measurement results, the pulse width has a mean value of approximately 3 µs (except for scenario 5) and a standard deviation between 0.05 µs and 1.2 µs, depending on the driving scenario. The inter-arrival time is equal to 50 µs on average, when the ignition is on. In case the vehicle is moving, the inter-arrival time becomes shorter resulting in more pulses over the same period of time. An even smaller inter-arrival time is observed, when the battery is being charged. The measurements also show that the noise signal has an energy between

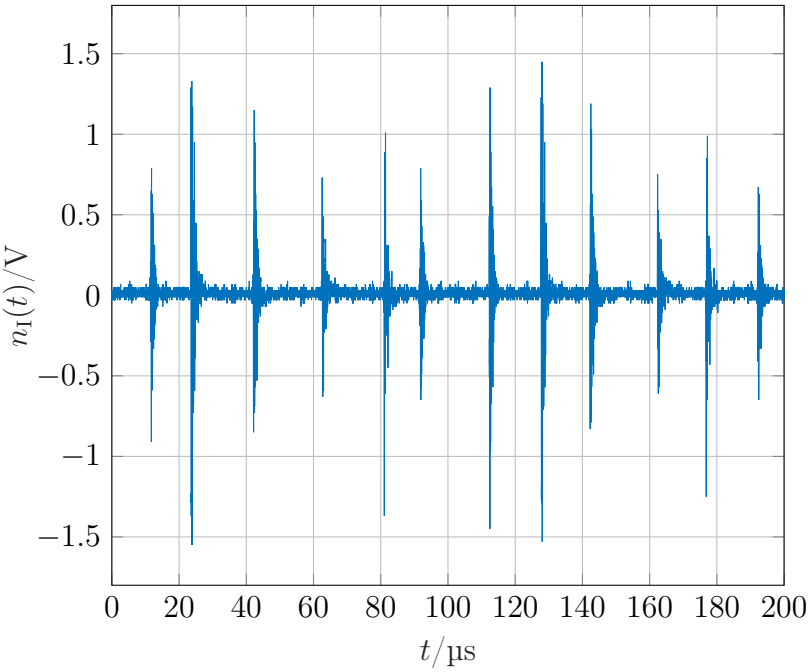

Figure 3.29: Impulsive noise measured in the case of scenario 9 (accelerating full power uphill)

$0.14\,\mathrm{mV^2\,s}$ and $0.45\,\mathrm{mV^2\,s}$.

The impulsive noise can be modeled as the sum of up to K amplitude-modulated single-tone sinusoids as follows:

$$n_{\mathrm{I}}(t) = \sqrt{2} \cdot \mathrm{Re}\left\{ \sum_{k=1}^{K} A_k \cdot u_{\mathrm{T}_k}(t) \cdot e^{j(2\pi f_k t + \phi_k)} \right\}, \tag{3.33}$$

where A_k is the amplitude of the k-th sinusoid with $k \in \{1, \cdots, K\}$, T_k is the period of the k-th sinusoid, f_k is the frequency and ϕ_k is the phase at $t = 0$. A_k, T_k and ϕ_k are random variables. $u_{\mathrm{T}_k}(t)$ describes the envelope of the amplitude-modulated k-th sinusoid as a function of time. In general, $u_{\mathrm{T}}(t)$ is defined as

$$u_{\mathrm{T}}(t) = \begin{cases} F \cdot e^{c_1(t-\hat{t})}, & \text{for} \quad 0 \le t < \hat{t} \\ F \cdot e^{-c_2(t-\hat{t})}, & \text{for} \quad \hat{t} \le t < T, \end{cases} \tag{3.34}$$

where F is a normalization factor and $\hat{t}$ is the value of t at which $u_{\mathrm{T}}(t)$ reaches a maximum. Starting from $t = 0$, the amplitude envelope increases exponentially until it reaches its maximum value at $t = \hat{t}$. The rise-time is determined by the positive non-zero integer factor c_1. For $t \ge \hat{t}$, the amplitude envelope falls

exponentially as a function of the positive non-zero integer c_2, i.e. c_2 determines the fall-time and, thus, the steepness of the function decay. The normalization factor F is chosen such that

$$\int_{t=0}^{T} |u_{\mathrm{T}}(t)|^2 dt = 1, \tag{3.35}$$

and can be calculated as follows:

$$F = \frac{c_1 + c_2}{c_1 \cdot c_2} - \left[\frac{1}{c_1} e^{-c_1 \hat{t}} + \frac{1}{c_2} e^{-c_2 (T - \hat{t})} \right]. \tag{3.36}$$

We assume that the phase ϕ_k is uniformly distributed over the range from 0 to 2π. In addition, we assume that the pulse width, the inter-arrival time, the amplitude and the point in time at which the peak amplitude is reached have each a Gaussian distribution with means and variances as given in Table 3.4.

We compare the measured noise signals and those obtained using the model, both in the time and frequency domains. Figure 3.30 shows a sample noise signal produced by using the model for scenario 9 (accelerating full power uphill). The first pulse in this signal is shown in Figure 3.31 in addition to the measured one, while in Figure 3.32 we can see the noise power spectral densities. The obtained results suggest that, knowing the statistical properties of the noise, the real world impulsive noise can be reproduced to a relatively satisfactory extent. Having a second look at Figure 3.32, we notice that the noise power spectral density lies significantly below the noise floor at frequencies above 40 MHz, which justifies an AWGN noise model in that frequency range, as it will be assumed in the next sections.

3.4 Channel model

Channel models are mathematical models used to emulate the effects of the physical medium on the transmit signal. In this section we focus on the frequency selectivity of the channel, the fading and the channel noise. As shown in Section 3.3, the channel noise can be modeled as AWGN at frequencies above 40 MHz. Assuming that the PLC channel is time-invariant, we can use a linear time-invariant (LTI) filter to model the channel. A LTI filter is characterized by its impulse response (CIR) in the time domain and its frequency response in the frequency domain. For convenience, the physical

Driving Scenario	**Noise Type**	**Pulse Width (μs)**		**Inter-arrival Time (μs)**		**Noise Energy (10^{-7}V²s)**	
		μ_{T}	σ_{T}	μ_{τ}	σ_{τ}	μ_{A}	σ_{A}
Ignition on P, engine off	Periodic	3.1	0.044	50.0	0.2	1.8	0.43
Ignition on P, engine powered	Periodic	3.0	0.15	50.0	0.14	2.1	2.0
Ignition on "engine running" (hold by brake)	Periodic	3.0	0.15	50.1	0.11	1.9	0.85
Ignition on "engine running" (hill hold)	Periodic	3.4	0.22	50.0	0.17	4.5	2.2
@ 250 V charger	Periodic	0.95	1.2	2.1	2.3	0.0045	0.0061
10 km/h uphill	Periodic	2.8	0.36	22.4	0.2	2.4	2.3
30 km/h uphill	Aperiodic	2.6	0.27	15.4	0.1	1.4	1.0
60 km/h uphill	Aperiodic	3.2	1.1	20.3	8.4	1.7	1.1
Accelerating full power uphill	Aperiodic	2.7	0.36	16.4	3.5	2.3	1.9
60 km/h braking	Aperiodic	2.9	0.45	18.6	5.7	2.9	1.6

Table 3.4: Impulsive noise characteristics for different driving scenarios (measurement data provided by Robert Bosch GmbH)

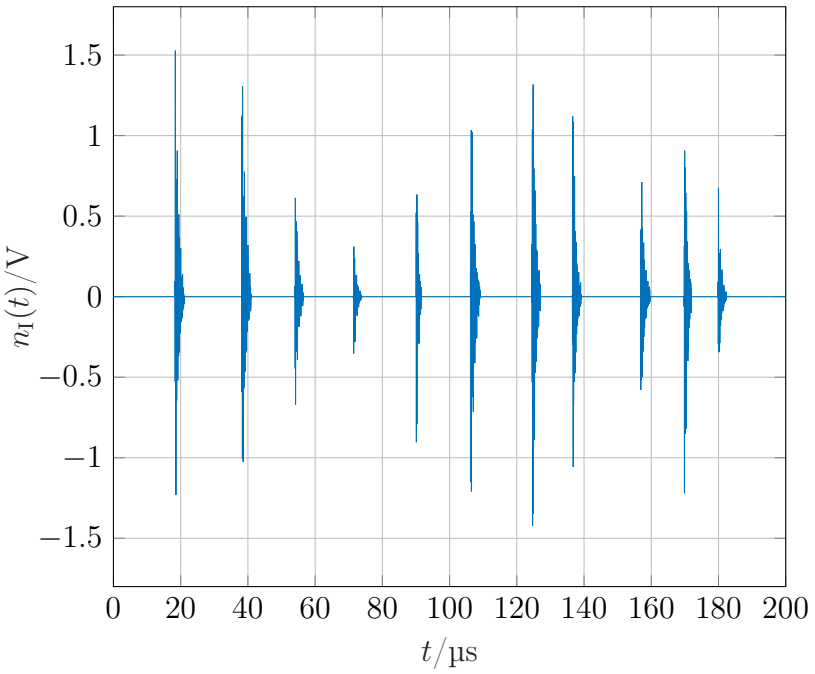

Figure 3.30: Modeled impulsive noise obtained in the case of scenario 9 (accelerating full power uphill)

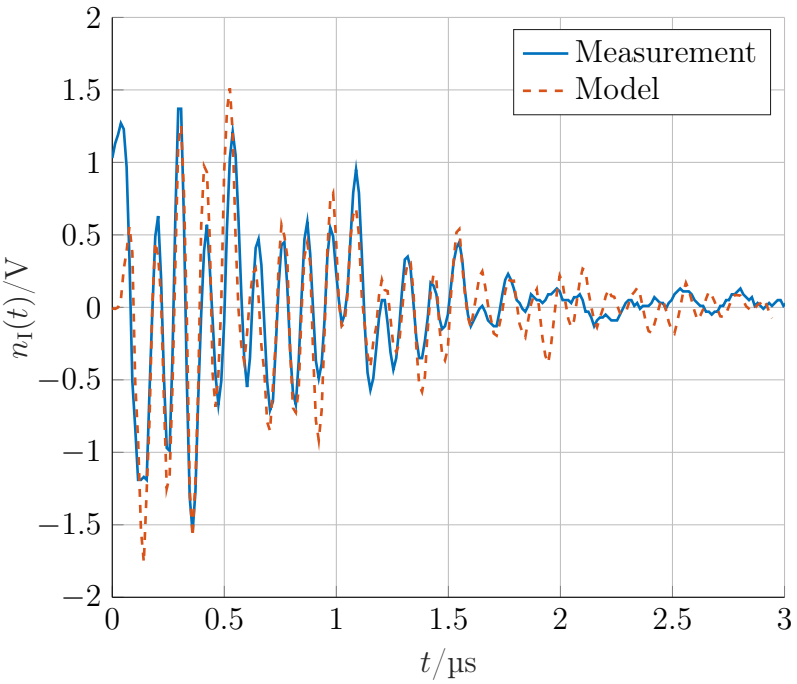

Figure 3.31: First pulse in the noise signal obtained in the case of scenario 9 (accelerating full power uphill)

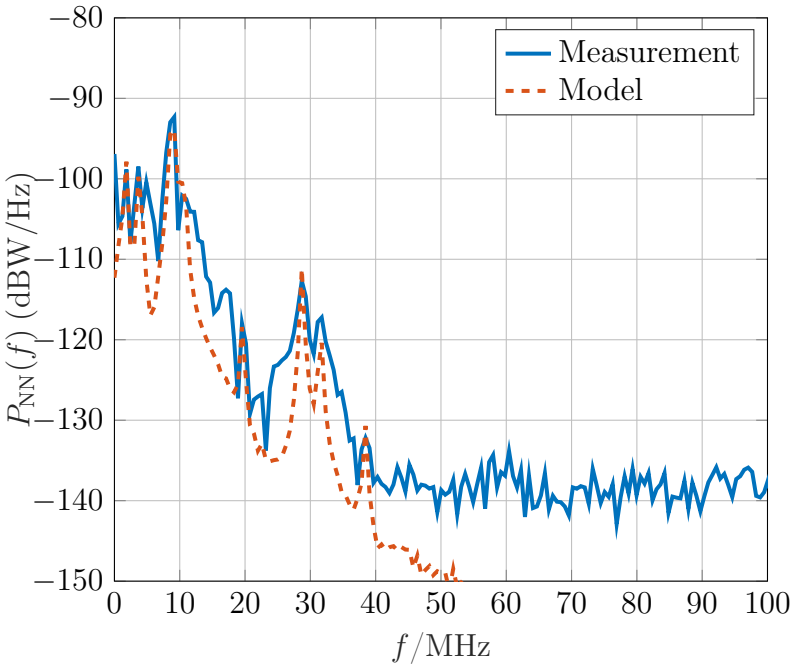

Figure 3.32: Noise power spectrum density in the case of scenario 9 (accelerating full power uphill)

layer simulations are performed using a symbol rate channel model. In addition, perfect synchronization at the receiver is assumed.

3.4.1 Signal-to-noise ratio maximization

In the equivalent baseband representation, the symbol rate-sampled received signal can be expressed as

$$y[k] = \sum_{i=-\infty}^{\infty} a_i c[k-i] + n[k], \tag{3.37}$$

where a_m are the zero-mean, statistically independent and identically distributed transmit symbols and $n[k]$ is the sampled noise process with zero-mean and variance σ^2. $c[k]$ is the overall channel impulse response given as

$$c[k] = \tilde{h}[k] * g_{\mathrm{w}}[k] \quad \text{with} \quad \tilde{h}[k] = g_{\mathrm{T}}[k] * h_{\mathrm{b}}[k] * g_{\mathrm{R}}[k], \tag{3.38}$$

where $*$ denotes the convolution, $g_{\mathrm{T}}[k]$ and $g_{\mathrm{R}}[k]$ are the discrete-time impulse responses of the transmit and receive filters, respectively, $g_{\mathrm{w}}[k]$ is the impulse response of the (optional) whitening filter and $h_{\mathrm{b}}[k]$ is the impulse response of

the channel in the equivalent baseband representation. In order to maximize the SNR at the receiver, the receive filter must be matched to the transmit filter and the channel. If the channel is frequency-selective, the noise would be colored at the output of the matched filter. In this case, it is required to use a whitening filter for noise decorrelation. The matched filter combined with the whitening filter is called the whitened matched filter (WMF). The noise at the output of the whitening filter is white assuming symbol-rate sampling. The impulse response of the matched filter is given as

$$g_{\mathrm{m}}[k] = g_{\mathrm{T}}^{*}[-k] * h_{\mathrm{b}}^{*}[-k], \tag{3.39}$$

where * denotes the complex conjugate. Even though a receive filter that is matched to the transmit filter is only suboptimal in terms of SNR maximization, it has the advantage that it does not have to be adapted to the channel. We will also see later that in case of the PLC channel there is no significant difference in the BER performance between a whitened matched filter and a receive filter that is matched to the transmit filter only. In the latter case, the channel noise is white if the transmit pulse shaping filter is a square-root Nyquist pulse (refer to 2.4.3.2). In order to reduce the ISI, square-root Nyquist filters such as the root-raised-cosine (RRC) filters should be used as transmit and receive filters. The cascade of two square-root Nyquist filters is equivalent to a Nyquist filter. The channel model can be then represented as a cascade of two LTI filters, one for the Nyquist filter and one for the channel. In this case, the overall channel impulse response can be expressed as

$$c[k] = \tilde{g}[k] * h_{\mathrm{b}}[k], \tag{3.40}$$

where $\tilde{g}[k]$ is the discrete-time impulse response of the Nyquist filter.

3.4.2 Whitening filter

Let $R_{\mathrm{nn}}[i]$ be the ACF of the channel noise (AWGN) defined as

$$R_{\mathrm{nn}}[i] = (n \star n)[i] = \sum_{k} n^{*}[k] n[k+i] = n^{*}[-i] * n[i]. \tag{3.41}$$

$R_{\mathrm{nn}}[i]$ can be represented as a Dirac delta function. Thus, its z-transform $\Phi_{\mathrm{nn}}(z)$ is equal to 1[8]. The z-transform converts a discrete-time signal into a

[8]For simplicity, we assume the noise has unit variance.

complex frequency domain representation. It is the discrete-time version of the Laplace transform, which is very similar to the Fourier transform, except that it is a complex function of a complex variable $s = \sigma + j\omega$ and is restricted to functions of positive t [51]. The (two-sided) z-transform of a signal $x[k]$ is defined according to [52] as

$$X(z) = \mathcal{Z}\{x[k]\} = \sum_{k=-\infty}^{\infty} x[k]z^{-k}. \tag{3.42}$$

The noise at the output of the matched filter is colored and can be expressed as $\tilde{n}[k] = n[k] * g_{\mathrm{m}}[k]$. Let $R_{\tilde{\mathrm{n}}\tilde{\mathrm{n}}}[i]$ be the ACF of the colored noise. Then we have

$$R_{\tilde{\mathrm{n}}\tilde{\mathrm{n}}}[i] = R_{\mathrm{nn}}(z) * R_{\mathrm{mm}}(z). \tag{3.43}$$

Let $\Phi_{\tilde{\mathrm{n}}\tilde{\mathrm{n}}}(z)$ be the z-transform of $R_{\tilde{\mathrm{n}}\tilde{\mathrm{n}}}[i]$. From (3.43), we can deduce that

$$\Phi_{\tilde{\mathrm{n}}\tilde{\mathrm{n}}}(z) = \Phi_{\mathrm{nn}}(z) \cdot \Phi_{\mathrm{mm}}(z) = \Phi_{\mathrm{mm}}(z), \tag{3.44}$$

where $\Phi_{\mathrm{mm}}(z)$ is the z-transform of the ACF of the matched filter impulse response. Assuming $\Phi_{\tilde{\mathrm{n}}\tilde{\mathrm{n}}}(z)$ is a rational function of z, $\Phi_{\tilde{\mathrm{n}}\tilde{\mathrm{n}}}(z)$ can be expressed as the ratio of the numerator polynomial $B(z)$ to the denominator polynomial $D(z)$. The roots of the numerator represent the zeros of $\Phi_{\tilde{\mathrm{n}}\tilde{\mathrm{n}}}(z)$, while those of the denominator represent the poles. Since the matched filter is a linear finite impulse response (FIR) filter, $\Phi_{\tilde{\mathrm{n}}\tilde{\mathrm{n}}}(z)$ has only zeros and no poles. Furthermore, due to the symmetry of the ACF, we have $\Phi_{\tilde{\mathrm{n}}\tilde{\mathrm{n}}}(z) = \Phi_{\tilde{\mathrm{n}}\tilde{\mathrm{n}}}(z^{-1})$. As a result, $\Phi_{\tilde{\mathrm{n}}\tilde{\mathrm{n}}}(z)$ can be written as

$$\Phi_{\tilde{\mathrm{n}}\tilde{\mathrm{n}}}(z) = B(z) = A\prod_i (1 - q_i z^{-1})(1 - q_i z), \tag{3.45}$$

where q_i and $1/q_i$ are real- or complex-valued zeros [39]. $\Phi_{\tilde{\mathrm{n}}\tilde{\mathrm{n}}}(z)$ can be decomposed into a product of two functions $\Phi^{+}_{\tilde{\mathrm{n}}\tilde{\mathrm{n}}}(z)$ and $\Phi^{-}_{\tilde{\mathrm{n}}\tilde{\mathrm{n}}}(z)$ defined as

$$\Phi^{+}_{\tilde{\mathrm{n}}\tilde{\mathrm{n}}}(z) = \sqrt{A}\prod_i (1 - q_i z^{-1}) \tag{3.46}$$

and

$$\Phi^{-}_{\tilde{\mathrm{n}}\tilde{\mathrm{n}}}(z) = \sqrt{A}\prod_i (1 - q_i z). \tag{3.47}$$

Let $R_{\mathrm{ww}}[i]$ be the ACF of the impulse response $g_{\mathrm{w}}[k]$ of the whitening filter and $\Phi_{\mathrm{ww}}(z)$ be the z-transform of $R_{\mathrm{ww}}[i]$. $\Phi_{\mathrm{ww}}(z)$ is given by

$$\Phi_{\mathrm{ww}}(z) = G_{\mathrm{ww}}(z^{-1}) \cdot G_{\mathrm{ww}}(z), \tag{3.48}$$

where $G_{\mathrm{ww}}(z)$ is the z-transform of $g_{\mathrm{w}}[k]$. Since $n[k] = \tilde{n}[k] * g_{\mathrm{w}}[k]$, we obtain

$$R_{\mathrm{nn}}[i] = R_{\tilde{\mathrm{n}}\tilde{\mathrm{n}}}[i] * R_{\mathrm{ww}}[i], \tag{3.49}$$

which means that $\Phi_{\mathrm{nn}}(z)$ relates to $\Phi_{\tilde{\mathrm{n}}\tilde{\mathrm{n}}}(z)$ as follows:

$$\Phi_{\mathrm{nn}}(z) = \Phi_{\tilde{\mathrm{n}}\tilde{\mathrm{n}}}(z) \cdot G_{\mathrm{ww}}(z^{-1}) \cdot G_{\mathrm{ww}}(z) = 1. \tag{3.50}$$

Based on (3.38) and (3.39) we have

$$\tilde{h}[i] = g_{\mathrm{m}}^{*}[-i] * g_{\mathrm{m}}[i] = R_{\mathrm{mm}}[i]. \tag{3.51}$$

Thus, the z-transform of the overall channel impulse response $c[k]$ can be expressed as

$$C(z) = \Phi_{\mathrm{mm}}(z) \cdot G_{\mathrm{ww}}(z) = \Phi_{\tilde{\mathrm{n}}\tilde{\mathrm{n}}}(z) \cdot G_{\mathrm{ww}}(z). \tag{3.52}$$

As shown earlier, $\Phi_{\tilde{\mathrm{n}}\tilde{\mathrm{n}}}(z)$ can be expressed as the product of $\Phi^{+}_{\tilde{\mathrm{n}}\tilde{\mathrm{n}}}(z)$ and $\Phi^{-}_{\tilde{\mathrm{n}}\tilde{\mathrm{n}}}(z)$, where $\Phi^{-}_{\tilde{\mathrm{n}}\tilde{\mathrm{n}}}(z) = \Phi^{+}_{\tilde{\mathrm{n}}\tilde{\mathrm{n}}}(z^{-1})$. In case $|q_i| \leq 1 \ \forall i$, all zeros of $\Phi^{+}_{\tilde{\mathrm{n}}\tilde{\mathrm{n}}}(z)$ are inside the unit circle $|z| = 1$, while those of $\Phi^{-}_{\tilde{\mathrm{n}}\tilde{\mathrm{n}}}(z)$ are outside. Knowing that a minimum-phase filter has poles and zeros inside the unit circle in the z-plane (excluding the unit circle itself) [51], $G_{\mathrm{ww}}(z)$ can be chosen equal to $1/\Phi^{+}_{\tilde{\mathrm{n}}\tilde{\mathrm{n}}}(z)$ in order to obtain a causal, stable and minimum-phase whitening filter. In this case, $c[k]$ would be maximum-phase with zeros outside the unit circle, and $C(z)$ would be equal to $\Phi^{-}_{\tilde{\mathrm{n}}\tilde{\mathrm{n}}}(z)$. However, for practical reasons, the overall channel impulse response must be minimum-phase. To fulfill this requirement, we have to set $G_{\mathrm{ww}}(z)$ equal to $1/\Phi^{-}_{\tilde{\mathrm{n}}\tilde{\mathrm{n}}}(z)$, which would result in an unstable system, as $G_{\mathrm{ww}}(z)$ would have poles outside the unit circle. The approximation given in [39] helps to get around this problem. It shows that a pole at a distance $d = 1 + d_0$ from the zero point in the z-plane can be approximated by a set of equidistant zeros, placed on a circle with a radius equal to d, excluding the position of the pole to be approximated. This approximation leads to a stable maximum-phase whitening filter and yields a minimum-phase channel model with $C(z) = \Phi^{+}_{\tilde{\mathrm{n}}\tilde{\mathrm{n}}}(z)$.

3.4.3 Channel frequency response

In Section 3.3, the voltage transfer function $H(f)$ was derived from the S-parameters in the frequency range 1 MHz to 100 MHz. Let $\tilde{H}(f)$ be the equivalent complex baseband frequency response of the bandlimited PLC channel. $\tilde{H}(f)$ can be obtained from $H(f)$ by frequency translation and low pass filtering as follows:

$$\tilde{H}(f) = G_{\mathrm{T}}(f) \cdot H(f + f_{\mathrm{c}}) \cdot G_{\mathrm{R}}(f), \tag{3.53}$$

where f_{c} denotes the carrier frequency, while $G_{\mathrm{T}}(f)$ and $G_{\mathrm{R}}(f)$ refer to the equivalent baseband frequency responses of the transmit and receive filters, respectively. Assuming B is the bandwidth allocated for data transmission, the carrier frequency can have any value between $f_{\mathrm{c,min}}$ and $f_{\mathrm{c,max}}$ defined as

$$f_{\mathrm{c,min}} = 1\,\mathrm{MHz} + \frac{B}{2}, \quad \text{and} \quad f_{\mathrm{c,max}} = 100\,\mathrm{MHz} - \frac{B}{2}. \tag{3.54}$$

In the remainder of this section, we assume that RRC filters are used. In this case, the channel bandwidth is given as

$$B = \frac{1+\alpha}{T_{\mathrm{s}}}, \tag{3.55}$$

and is, therefore, a function of the symbol duration T_{s} and the roll-off factor α of the equivalent raised-cosine (RC) filter. In case of suboptimal filtering, the overall channel frequency response can be expressed as

$$C(f) = G_{\mathrm{RC}}(f) \cdot H(f + f_{\mathrm{c}}), \tag{3.56}$$

where $G_{\mathrm{RC}}(f)$ is the equivalent baseband frequency response of the RC filter defined according to [42] as

$$G_{\mathrm{RC}}(f) = \begin{cases} T_{\mathrm{s}}, & |f| \leq \frac{1-\alpha}{2T_{\mathrm{s}}} \\ T_{\mathrm{s}} \cos^2\left(\frac{\pi T_{\mathrm{s}}}{2\alpha}\left(|f| - \frac{1-\alpha}{2T_{\mathrm{s}}}\right)\right), & \frac{1-\alpha}{2T_{\mathrm{s}}} < |f| \leq \frac{1+\alpha}{2T_{\mathrm{s}}} \\ 0, & \text{otherwise.} \end{cases} \tag{3.57}$$

Figure 3.33 shows, as an example, the overall channel frequency response of the bandlimited PLC channel of battery cell Nº3 obtained at $f_{\mathrm{c}} = 15\,\mathrm{MHz}$ in

case of suboptimal filtering with $B = 2.7\,\text{MHz}$ and $\alpha = 0.35$. In case matched filtering is applied, $C(f)$ can be expressed as

$$C(f) = G_{\text{RC}}(f) \cdot |H(f + f_{\text{c}})|^2 \cdot G_{\text{ww}}(f), \tag{3.58}$$

where $G_{\text{ww}}(f)$ is the equivalent baseband frequency response of the whitening filter.

3.4.4 Channel impulse response

Given the carrier frequency and the target symbol rate or the allocated channel bandwidth, the CIR $c(t)$ can be calculated from the CFR $C(f)$, using the inverse Fourier transform (IFT). In case of suboptimal filtering, $c(t)$ can be expressed as

$$c(t) = g_{\text{RC}}(t) * \left(h(t) e^{-j2\pi f_{\text{c}} t} \right), \tag{3.59}$$

where $g_{\text{RC}}(t)$ is the IFT of $G_{\text{RC}}(f)$ and $h(t)$ is the IFT of $H(f)$. Figure 3.34 shows the continuous-time baseband CIR of the PLC channel of battery cell №3 at $f_{\text{c}} = 15\,\text{MHz}$ with $B = 2.7\,\text{MHz}$ and $\alpha = 0.35$. $c(t)$ is sampled with the symbol rate in order to obtain the discrete-time impulse response $c[k]$. Frequency-selective channels are time dispersive, i.e. the received signal consists of multiple attenuated copies of the transmit signal with different delays. Therefore, the discrete-time CIR can be written as

$$c[k] = \sum_{i=0}^{l-1} a_i \delta[k - i], \tag{3.60}$$

where l is the channel length and a_i is the coefficient of the i-th channel tap.

3.4.5 Frequency selectivity analysis

In this section, we investigate the impact of the roll-off factor on the CIR, assuming RC filtering. In a next step, we analyze the channel frequency selectivity as a function of the allocated channel bandwidth.

A flat fading channel has a coherence bandwidth that is larger than the signal bandwidth. Thus, all the frequency components of the transmit signal are affected by the same magnitude of fading. Unlike flat fading channels, frequency-selective channels have a coherence bandwidth that is smaller than the signal

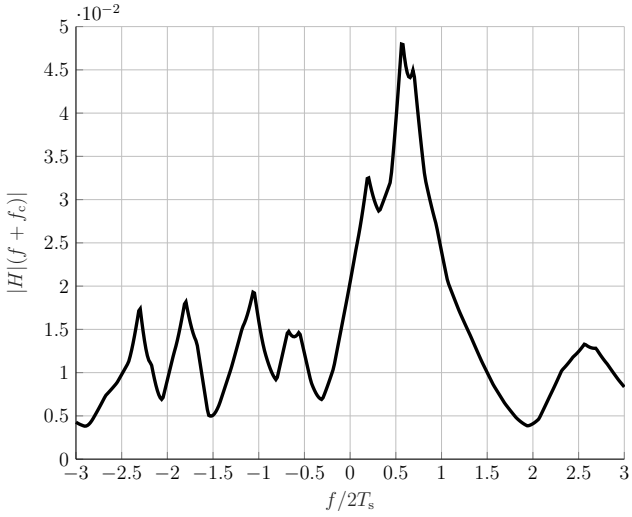

(a) Baseband channel frequency response ($f_c = 15\,\text{MHz}$)

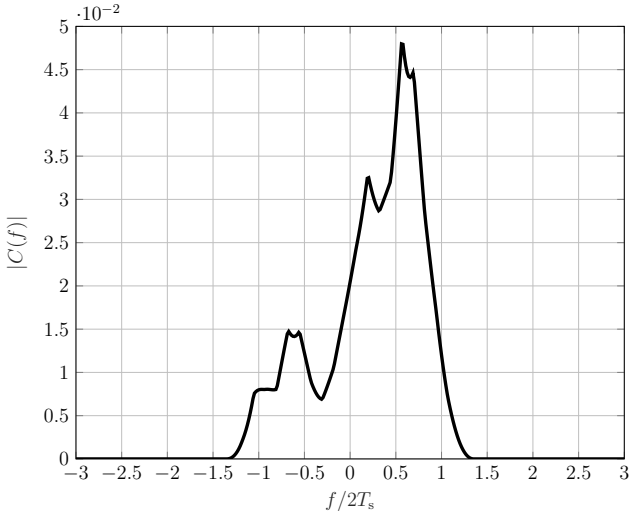

(b) Baseband channel frequency response including RC-filtering ($\alpha = 0.35$, $T_s = 0.5\mu s$)

Figure 3.33: Equivalent baseband channel frequency response (cell Nº3)

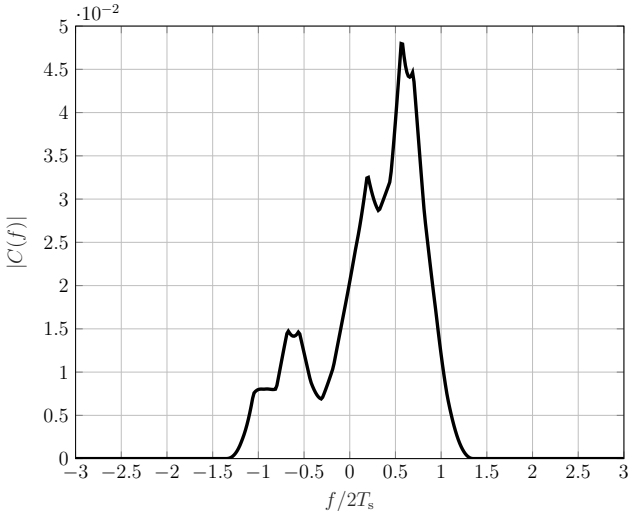

(a) Baseband channel frequency response

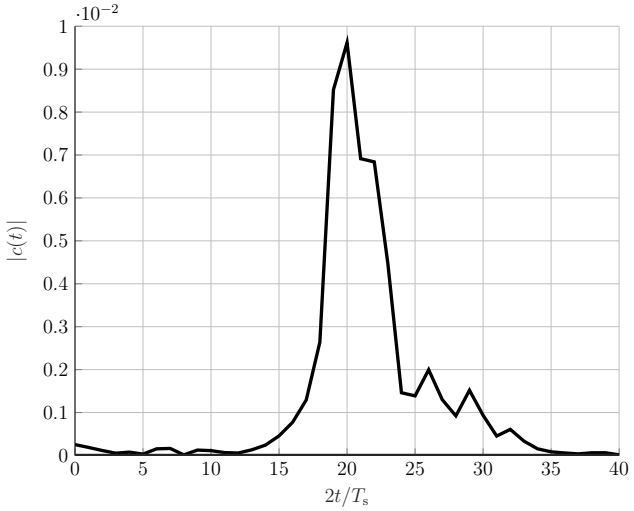

(b) Continuous-time channel impulse response

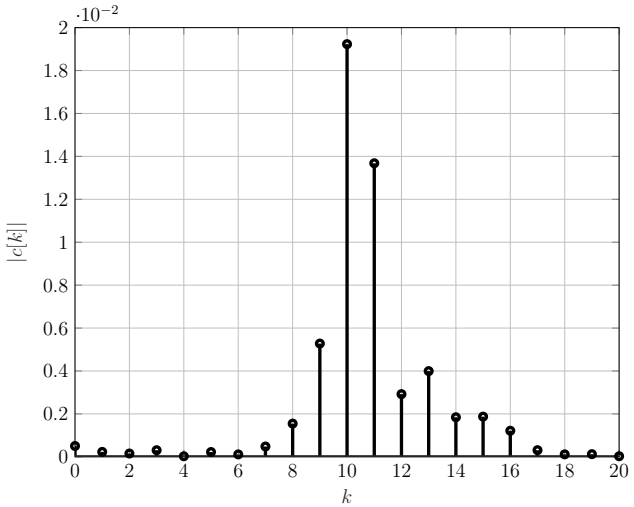

(c) Symbol rate-sampled channel impulse response

Figure 3.34: Equivalent baseband channel impulse response (cell Nº3, $f_\mathrm{c} = 15\,\mathrm{MHz}$, $\alpha = 0.35$ and $T_\mathrm{s} = 0.5\,\mu\mathrm{s}$)

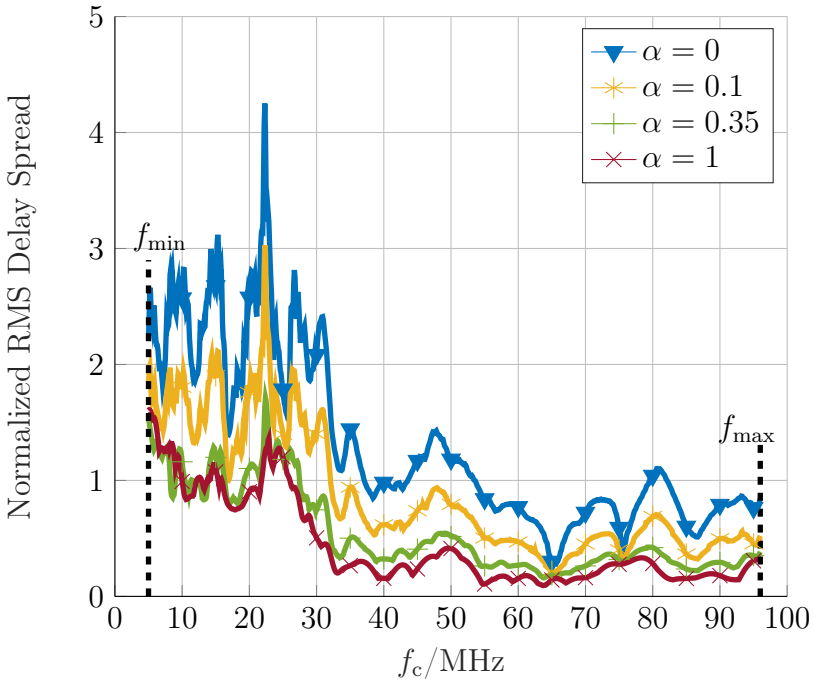

Figure 3.35: Maximum RMS delay spread, normalized to the symbol duration ($R_s = 4\,\text{MBaud}$)

bandwidth. Thus, different frequencies are differently affected by the fading. The frequency selectivity of the PLC channel can be characterized, using the RMS delay spread τ_{rms}, which is equal to the second central moment of the channel power delay profile [53]. In case of a discrete channel, τ_{rms} is given by

$$\tau_{\text{rms}} = \sqrt{\frac{\sum_{i=0}^{l-1}(\tau_i - \tau_a)^2 a_i^2}{\sum_{i=0}^{l-1} a_i^2}}, \quad \text{with} \quad \tau_a = \frac{\sum_{i=0}^{l-1} \tau_i a_i^2}{\sum_{i=0}^{l-1} a_i^2}, \tag{3.61}$$

where τ_a is the mean channel delay, a_i are the channel coefficients and τ_i are the channel tap delays with $i \in \{0, 1, \cdots, (l-1)\}$. The ratio of the RMS delay spread to the symbol duration can be used to roughly estimate the strength of the ISI and, thus, determine the complexity of the equalizer required at the receiver. Typically, when the symbol time period is greater than 10 times the RMS delay spread, no ISI equalizer is needed in the receiver [53].

In general, the choice of the roll-off factor of the RC filter depends on the available channel bandwidth in relation to the target symbol rate. In this section, we study another aspect related to the choice of the roll-off factor which is the channel frequency selectivity. For this purpose, we calculate the

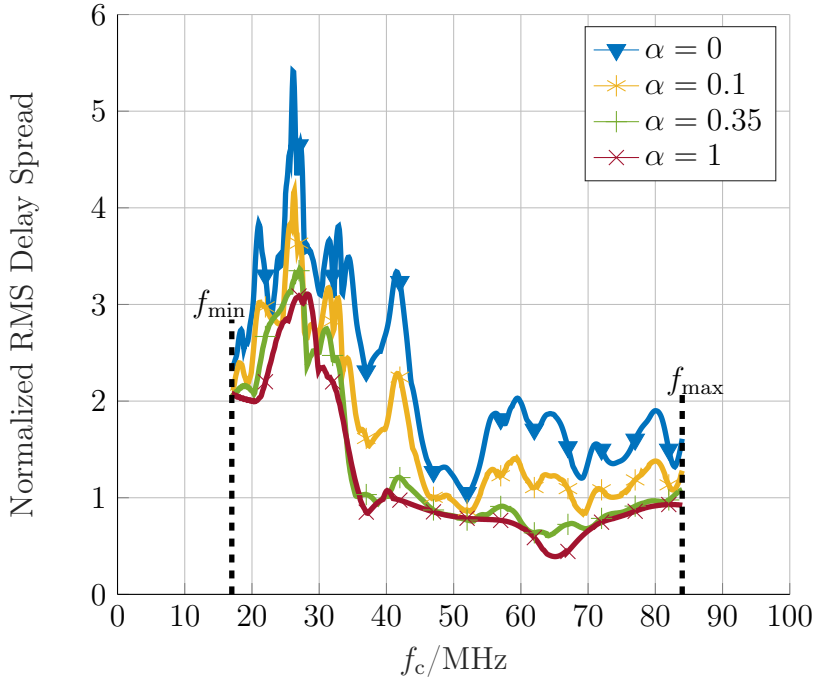

Figure 3.36: Maximum RMS delay spread normalized to the symbol duration ($R_s = 16\,\text{MBaud}$)

maximum RMS delay spread as a function of the carrier frequency f_c, the roll-off factor α and the target symbol rate R_s for the PLC channels of battery cells 1 to 48. The results obtained with $R_s = 4\,\text{MBaud}$ and $R_s = 16\,\text{MBaud}$ are shown in Figures 3.35 and 3.36, respectively. As can be seen, the RMS delay spread increases when α becomes smaller than 0.35, independently of the symbol rate. On the other hand, there is no significant change in the RMS delay spread for $\alpha \geq 0.35$. From these results, it can be concluded that 0.35 is an adequate value for the roll-off-factor. The RMS delay spread is not only smaller for $\alpha = 0.35$, compared with lower α values, but also a good spectral efficiency can be achieved in comparison with higher values of α.

ISI occurs when the RMS delay spread of a frequency-selective channel becomes an appreciable fraction of the symbol duration. In order to investigate the relationship between ISI and the symbol rate, we calculate the RMS delay spread as a function of the carrier frequency for different symbol rates. Some of the results are shown in Figure 3.37, where it can be seen that τ_{rms} increases at higher symbol rates. At frequencies below 32 MHz, τ_{rms} exceeds $0.8T_s$ and reaches a maximum value of $1.7T_s$, $2T_s$, $2.6T_s$, $3.4T_s$ and $4T_s$, when the symbol

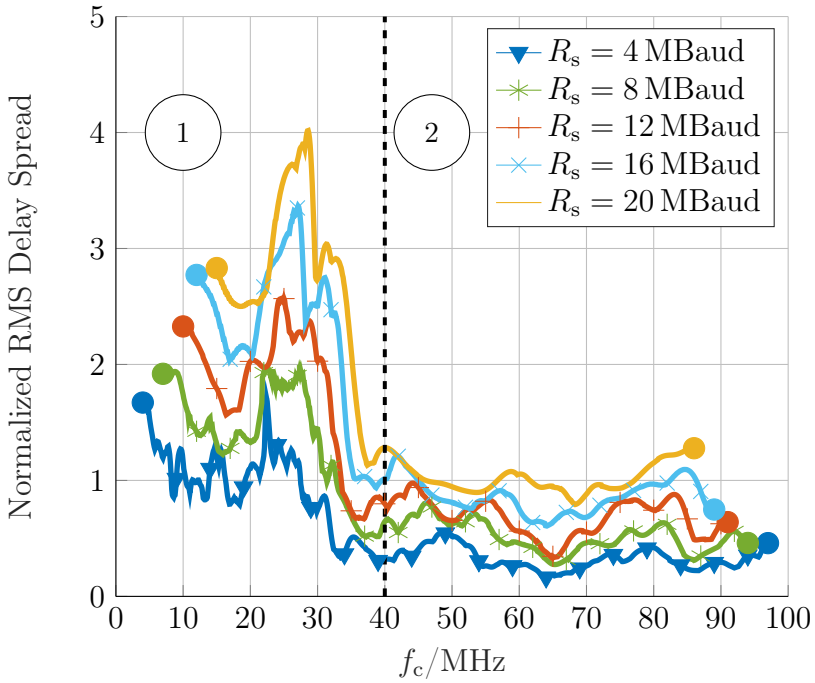

Figure 3.37: Maximum RMS delay spread normalized to the symbol duration with $\alpha = 0.35$: (1) moderate to strong ISI, (2) weak to moderate ISI

rate goes from 4 MBaud to 20 MBaud in steps of 4 MBaud. In the frequency range between 32 MHz and 40 MHz, the RMS delay spread decreases as the frequency increases. At higher frequencies, we obtain values between $0.2T_s$ and $1.3T_s$, which suggests that less ISI is expected to occur at frequencies above 40 MHz.

3.5 Physical layer performance analysis

In this section, we analyze the physical layer performance using single- and multi-carrier modulation, channel equalization and channel coding. We shed light on the relation between the choice of the modulation scheme and the target spectral efficiency, the target BER and the power efficiency. We also discuss the choice of the carrier frequency and elaborate on how to improve the power efficiency of the PLC system. Furthermore, we compare the performance and complexity of the MMSE equalization and the DFE. As for channel coding, both block and convolutional codes are discussed and evaluated.

Since the channel noise is assumed to be AWGN, the BER performance is

determined by E_b/N_0. The BER results are useful for the evaluation of the physical layer performance. In addition, they can be used as a good starting point for setting the requirements for the RF/analog part of the receiver. The BER curves can be interpreted as the lower bound for the required SNR to be delivered by the RF/analog part. In practice, the co-optimization of the analog receiver front end circuit and the digital baseband processing can enable receiver designs with efficient power consumption.

3.5.1 Channel capacity

Based on Shannon's second theorem, the channel capacity is the maximum rate at which information can be reliably transmitted over the channel. This suggests that at any rate less than the capacity, the information can be transferred with an arbitrarily small probability of error. Conversely, if data is transmitted at a rate higher than the capacity, then the probability of error is bounded away from zero [33, 54]. Let X and Y be two discrete random variables taking values in $\mathscr{X}$ and $\mathscr{Y}$, respectively. The channel capacity is then obtained by maximizing the mutual information of X and Y with respect to the probability mass function of X, i.e.

$$C = \frac{1}{T_\mathrm{s}} \max_{P_X} I(X;Y), \tag{3.62}$$

where T_s is the symbol duration and $I(X;Y)$ is given by

$$I(X;Y) = \sum_{x\in\mathscr{X}} \sum_{y\in\mathscr{Y}} P[x,y] \cdot \log_2 \left(\frac{P[x|y]}{P[x]} \right). \tag{3.63}$$

According to [33], $I(X;Y)$ is equivalently defined using the entropy function $H(.)$ as

$$I(X;Y) = H(X) - H(X|Y), \tag{3.64}$$

where $H(X)$ represents the entropy of the random variable X given by

$$H(X) = -\sum_{x\in\mathscr{X}} P[x] \cdot \log_2(P[x]), \tag{3.65}$$

while $H(X|Y)$ represents the conditional entropy of X given Y, which is according to [33] defined as

$$H(X|Y) = -\sum_{x\in\mathscr{X}} \sum_{y\in\mathscr{Y}} P[x,y] \cdot \log_2(P[x|y]). \tag{3.66}$$

3.5.1.1 Modulation-constrained capacity

Let $\boldsymbol{X} = (X_1, X_2, \cdots)$ and $\boldsymbol{Y} = (X_1, X_2, \cdots)$ be two infinite sequences of i.i.d. random variables, denoting the input and output of the channel. The first k elements of these sequences are represented by $\boldsymbol{X}_1^k = (X_1, X_2, \cdots, X_\mathrm{k})$ and $\boldsymbol{Y}_1^k = (Y_1, Y_2, \cdots, Y_\mathrm{k})$. The entropy of the stochastic process $\boldsymbol{X}$ is defined as

$$H(\boldsymbol{X}) = \lim_{k\to\infty} \frac{1}{k} H\left(\boldsymbol{X}_1^k\right). \tag{3.67}$$

The conditional entropy $H(\boldsymbol{X}|\boldsymbol{Y})$ is defined similarly, and the mutual information can be expressed as

$$\begin{aligned} I(\boldsymbol{X};\boldsymbol{Y}) &= \lim_{k\to\infty} \frac{1}{k} I\left(\boldsymbol{X}_1^k;\boldsymbol{Y}_1^k\right) \\ &= \lim_{k\to\infty} \frac{1}{k}\left(H\left(\boldsymbol{X}_1^k\right) - H\left(\boldsymbol{X}_1^k|\boldsymbol{Y}_1^k\right)\right). \end{aligned} \tag{3.68}$$

From (3.62) and (3.68), it can be inferred that

$$\begin{aligned} C &= \frac{1}{T_\mathrm{s}} I(\boldsymbol{X};\boldsymbol{Y}) \\ &= \frac{1}{T_\mathrm{s}} \lim_{k\to\infty} \frac{1}{k}\left(H\left(\boldsymbol{X}_1^k\right) - H\left(\boldsymbol{X}_1^k|\boldsymbol{Y}_1^k\right)\right). \end{aligned} \tag{3.69}$$

According to [33], given i.i.d. random variables, we have

$$H\left(\boldsymbol{X}_1^k\right) = kH(X_i), \quad \text{for} \quad 1 \le i \le k \tag{3.70}$$

where in case of M-ary modulation $H(X_i) = \log_2(M)$. Hence, the channel capacity given in (3.69) can be simpilified to

$$C = \frac{1}{T_\mathrm{s}}\left[\log_2(M) - \lim_{k\to\infty} \frac{1}{k} H\left(\boldsymbol{X}_1^k|\boldsymbol{Y}_1^k\right)\right]. \tag{3.71}$$

Taking a closer look at $H\left(\boldsymbol{X}_1^k|\boldsymbol{Y}_1^k\right)$ and assuming i.i.d. random variables, we can derive the following:

$$\begin{aligned} H\left(\boldsymbol{X}_1^k|\boldsymbol{Y}_1^k\right) &= -\sum_{\boldsymbol{x}_1^k,\boldsymbol{y}_1^k} P\left[\boldsymbol{x}_1^k,\boldsymbol{y}_1^k\right] \cdot \log_2\left(P\left[\boldsymbol{x}_1^k|\boldsymbol{y}_1^k\right]\right) \\ &= -\sum_{\boldsymbol{x}_1^k,\boldsymbol{y}_1^k} P\left[\boldsymbol{x}_1^k,\boldsymbol{y}_1^k\right] \cdot \log_2\left(\prod_{i=1}^{k} P\left[x_i|\boldsymbol{y}_1^k\right]\right) \\ &= -\sum_{i=1}^{k}\sum_{\boldsymbol{x}_1^k,\boldsymbol{y}_1^k} P\left[\boldsymbol{x}_1^k,\boldsymbol{y}_1^k\right] \cdot \log_2\left(P\left[x_i|\boldsymbol{y}_1^k\right]\right) \\ &= -\sum_{i=1}^{k}\sum_{x_i,\boldsymbol{y}_1^k} P\left[x_i,\boldsymbol{y}_1^k\right] \cdot \log_2\left(P\left[x_i|\boldsymbol{y}_1^k\right]\right). \end{aligned} \tag{3.72}$$

Thus, $H\left(\boldsymbol{X}_1^k|\boldsymbol{Y}_1^k\right)$ given in (3.72) reduces to

$$H\left(\boldsymbol{X}_1^k|\boldsymbol{Y}_1^k\right) = \sum_{i=1}^{k} H\left(x_i|\boldsymbol{y}_1^k\right) \overset{\text{i.i.d.}}{=} kH\left(x|\boldsymbol{y}_1^k\right). \tag{3.73}$$

By substituting $H\left(\boldsymbol{X}_1^k|\boldsymbol{Y}_1^k\right)$ in (3.71) with its expression given in (3.73), we obtain for the channel capacity

$$C = \frac{1}{T_\mathrm{s}}\left[\log_2(M) - \lim_{k\to\infty} H\left(x|\boldsymbol{y}_1^k\right)\right]. \tag{3.74}$$

In Section 3.4, we showed that the PLC channel can be modeled as an LTI filter with AWGN. Such a channel model can be interpreted as a finite state machine, where the states are determined by the content of a tapped delay line, used to represent the filter [55]. Each input symbol causes a state transition and the output is equal to the sample taken from the received signal in the corresponding time instance. Thus, a given input data sequence is uniquely associated with a channel state sequence [55]. This justifies that the hidden Markov model (HMM) can be used to model the PLC channel, where the states are unobservable (hidden) and can be indirectly inferred by analyzing the sequence of observed outputs [55]. We exploit the structure of the Markov chain to determine the a posteriori probabilities of the transmit symbols, conditioned on the observation of a noisy version of $\boldsymbol{y}_1^k$. In the simulation, we transmit long symbol sequences over the PLC channel and use the Bahl-Cocke-Jelinek-Raviv (BCJR) algorithm to process the received symbols. The BCJR algorithm is a symbol-by-symbol maximum a posteriori decoding algorithm, typically used in combination with convolutional channel coding [33]. We opt for this algorithm, because it produces the a posteriori probabilities needed to calculate the modulation-constrained channel capacity.

3.5.1.2 Capacity results

We calculate the modulation-constrained channel capacity as a function of E_b/N_0. As shown by Algorithm 1, we iterate over all the PLC channels, i.e. over the battery cells 1 to 48, and the carrier frequency in the range 10 MHz to 90 MHz. We take different symbol rates into consideration. Some of the results are represented in Figure 3.38, where we take the example of the battery cell №43, choose the carrier frequency to be equal to 52 MHz, and assume a symbol

rate of 4 MBaud. Both the unconstrained and the modulation-constrained channel capacities are given as a function of E_b/N_0. The modulation schemes used are BPSK and QPSK. Another example is shown in Figure 3.39 for the PLC channel of the same battery cell with the same carrier frequency and twice the symbol rate. As expected, the capacity curves show that BPSK and QPSK have the same power efficiency when the symbol rate is the same. Doubling the symbol rate causes a degradation in the power efficiency, as E_b/N_0 increases (by up to 2 dB).

Algorithm 1 used to determine the minimum $\gamma = E_\mathrm{b}/N_0$, required to reach the maximum channel capacity, using M-ary modulation schemes

```
for n ← 1 to 48 do                                   ▷ n denotes the cell position
    for R_s ← 1 MBaud to 20 MBaud do
        calculate f_c,min using R_s as given in (3.54)
        calculate f_c,max using R_s as given in (3.54)
        for f_c ← f_c,min to f_c,max do
            found ← false
            for γ ← 10 dB to 50 dB do
                calculate the capacity C̃ using the BCJR algorithm
                C(n, f_c, R_s, γ) ← C̃
                if found ≠ true and C̃ = log2(M) R_s then
                    γ(n, f_c, R_s) ← γ                ▷ maximum channel capacity
                    found ← true
                end if
            end for
        end for
    end for
end for
```

Note that the channel model used in the simulation is based on a complex-input complex-output channel with circular complex Gaussian noise. For this reason, the capacity of the unconstrained bandlimited PLC channel (obtained with Gaussian distributed input) can be calculated according to [56] as

$$C = \int_{-B/2}^{B/2} \log_2 \left(1 + \frac{S_\mathrm{rr}(f)}{S_\mathrm{nn}(f)} \right) \mathrm{d}f, \tag{3.75}$$

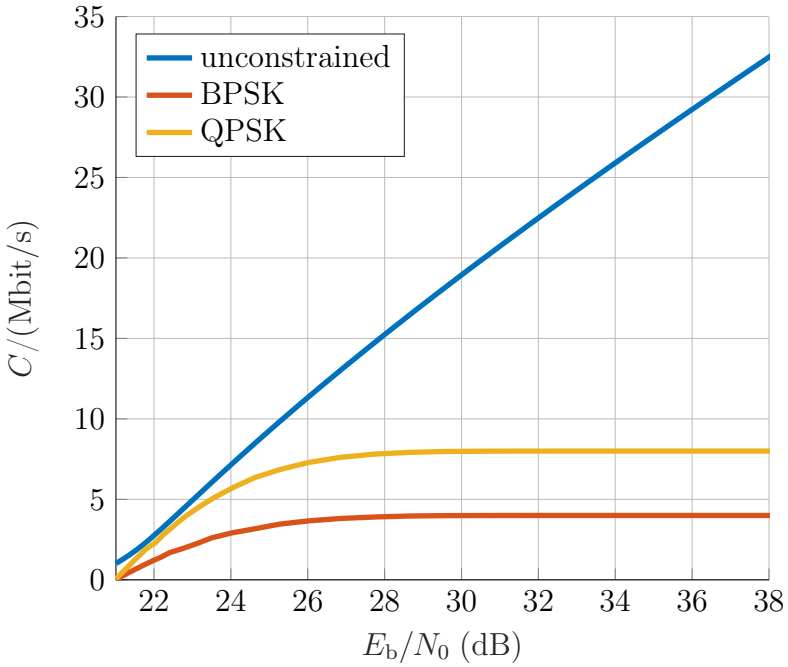

Figure 3.38: Channel capacity (cell №43, $f_c = 52\,\text{MHz}$ and $R_s = 4\,\text{MBaud}$)

where $S_{rr}(f)$ is the power spectral density of the received signal and $S_{nn}(f)$ is the noise power spectral density. $S_{rr}(f)$ can be obtained from the power spectral density of the transmit signal $S_{tt}(f)$ and the channel frequency response $C(f)$ as follows [56]:

$$S_{rr}(f) = S_{tt}(f) \cdot |C(f)|^2. \tag{3.76}$$

3.5.2 Choice of the modulation scheme

The choice of the digital modulation scheme significantly affects the characteristics, performance and in general the physical realization of a communication system. Digital modulation schemes can be classified into single- and multi-carrier schemes. Multi-carrier modulation is a method of dividing the transmit data into different data streams to be transmitted over narrowband subchannels at different carrier frequencies. As the name suggests, OFDM is a multi-carrier modulation technique using orthogonal subcarriers. An orthogonal channel partition allows for contiguous subchannels which turns out to be bandwidth efficient. The number of subchannels is chosen such that the symbol time on each subchannel is much greater than the delay spread of the channel or,

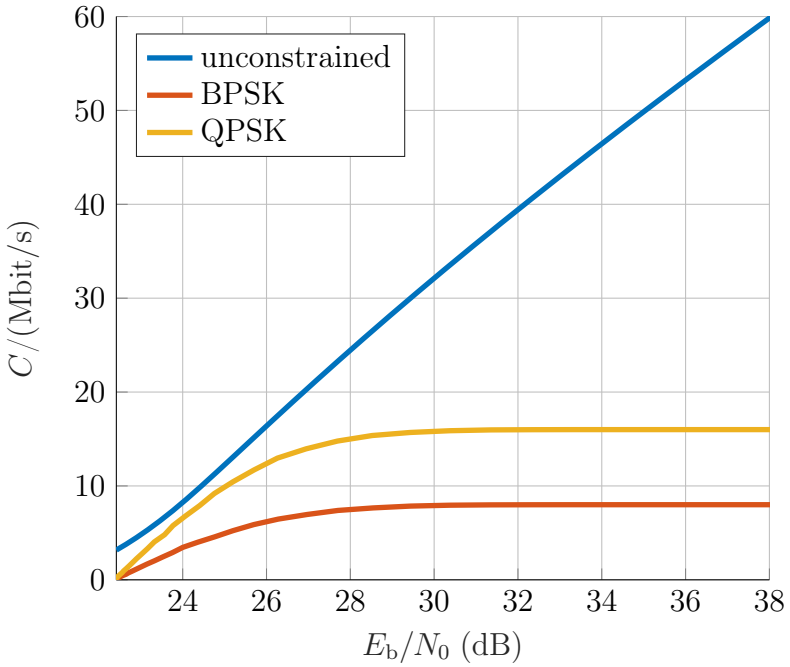

Figure 3.39: Channel capacity (cell Nº43, $f_c = 52\,\text{MHz}$ and $R_s = 8\,\text{MBaud}$)

equivalently, the subchannel bandwidth is smaller than the channel coherence bandwidth. This ensures that the subchannels experience a relatively flat fading, so that in each subchannel the ISI is very small and low-complexity algorithms can be used at the receiver for channel equalization [35].

In general, multi-carrier systems have a higher complexity than single-carrier systems. They typically suffer from a relatively high peak-to-average power ratio (PAPR), in addition to subcarrier fading and intercarrier interference (ICI). A high PAPR forces the transmit power amplifier to have a huge back-off, in order to ensure linear amplification of the signal. It also requires the use of a high-resolution A/D converter at the receiver, as a relatively wide dynamic range is usually required. This, in turn, places a complexity and power burden on the receiver front-end.

Bandwidth and energy efficiency are key factors in the choice of the modulation scheme. The bandwidth efficiency describes how efficient the utilization of the available channel bandwidth is in terms of data rate, whereas the energy efficiency is measured by the E_b/N_0, required to achieve a specific error rate. Very often there is a trade-off between bandwidth and power efficiency. For instance, a frequency-modulated signal has a constant envelope and is, therefore, less

susceptible to nonlinear amplification, which allows the use of energy efficient transmitters. However, in case of frequency modulation, the allocated channel bandwidth increases with the modulation order. In comparison, systems based on amplitude and/or phase modulation have a better bandwidth efficiency, but require the use of linear amplifiers at the receiver and are typically less power efficient. Therefore, frequency modulation is typically used for power limited systems with a sufficiently large bandwidth, while linear modulation is suitable for bandlimited communication system with a sufficiently high SNR.

Higher order linear modulation is less resilient to noise and interference than binary modulation. However, it offers faster data rates and higher levels of spectral efficiency. Many communication systems use dynamic adaptive modulation techniques to sense the channel conditions and adapt the modulation scheme accordingly, especially in the case of time-variant channels. The use of adaptive modulation allows to achieve the highest possible data rate under the given conditions, however, at the cost of higher complexity. Since we assumed that the PLC channel is time-invariant, there is no need for adaptive modulation. Very often complexity is traded off against performance. For instance, a low-complexity receiver can be used in the case of differential modulation, where the detection is non-coherent. However, the SNR required to reach a specific BER is typically higher than the SNR required in the case of non-differential modulation with coherent detection.

3.5.3 Choice of the carrier frequency

In this section we show that the power efficiency of the PLC system depends on the choice of the carrier frequency and whether a fixed or a flexible power allocation is adopted. Using the example of channel equalization, we also explain how the system complexity can be reduced by choosing the appropriate carrier frequency.

3.5.3.1 Power efficiency

The power efficiency of the physical layer depends on the power allocation scheme used by the CMUs. Two types of power allocation are discussed here, namely, the equal and the flexible power allocation. If the power allocation is

fixed and equal, all CMUs would have the same transmit power. If, however, the power allocation is flexible, the transmit power can be adapted to the channel, which helps to optimize the power consumption. In Section 3.5.1.2, the minimum $\gamma = E_\mathrm{b}/N_0$ required to reach the maximum channel capacity was calculated as a function of the cell position in the pack, the carrier frequency and the symbol rate using M-ary modulation schemes. As shown by Algorithm 2, we calculate the minimum and maximum values (taken over all the battery cells) of the required minimum γ and denote them by γ_min and γ_max, respectively. Both are determined as a function of the carrier frequency and the symbol rate.

Algorithm 2 used to determine the minimum and maximum values (taken over all the battery cells) of the minimum $\gamma = E_\mathrm{b}/N_0$, required to achieve maximum channel capacity, using M-ary modulation schemes

Requirement: the minimum required γ to reach maximum channel capacity as a function of the cell position, the carrier frequency and the symbol rate.
Requirement: $\gamma_\mathrm{min}(f_\mathrm{c}, R_\mathrm{s}) = \gamma_\mathrm{max}(f_\mathrm{c}, R_\mathrm{s}) = 0 \; \forall (f_\mathrm{c}, R_\mathrm{s})$
for $n \leftarrow 1$ to 48 **do** ▷ n denotes the cell position
  for $R_\mathrm{s} \leftarrow 1\,\mathrm{MBaud}$ to $20\,\mathrm{MBaud}$ **do**
    calculate $f_\mathrm{c,min}$ and $f_\mathrm{c,max}$ using R_s (see (3.54) and (3.54))
    for $f_\mathrm{c} \leftarrow f_\mathrm{c,min}$ to $f_\mathrm{c,max}$ **do**
      $\tilde{\gamma} \leftarrow \gamma(n, f_\mathrm{c}, R_\mathrm{s})$
      if $\gamma_\mathrm{min}(f_\mathrm{c}, R_\mathrm{s}) = 0$ **and** $\gamma_\mathrm{max}(f_\mathrm{c}, R_\mathrm{s}) = 0$ **then**
        $\gamma_\mathrm{min}(f_\mathrm{c}, R_\mathrm{s}), \gamma_\mathrm{max}(f_\mathrm{c}, R_\mathrm{s}) \leftarrow \tilde{\gamma}$
      end if
      if $\tilde{\gamma} < \gamma_\mathrm{min}(f_\mathrm{c}, R_\mathrm{s})$ **then**
        $\gamma_\mathrm{min}(f_\mathrm{c}, R_\mathrm{s}) \leftarrow \tilde{\gamma}$
      end if
      if $\tilde{\gamma} > \gamma_\mathrm{max}(f_\mathrm{c}, R_\mathrm{s})$ **then**
        $\gamma_\mathrm{max}(f_\mathrm{c}, R_\mathrm{s}) \leftarrow \tilde{\gamma}$
      end if
    end for
  end for
end for

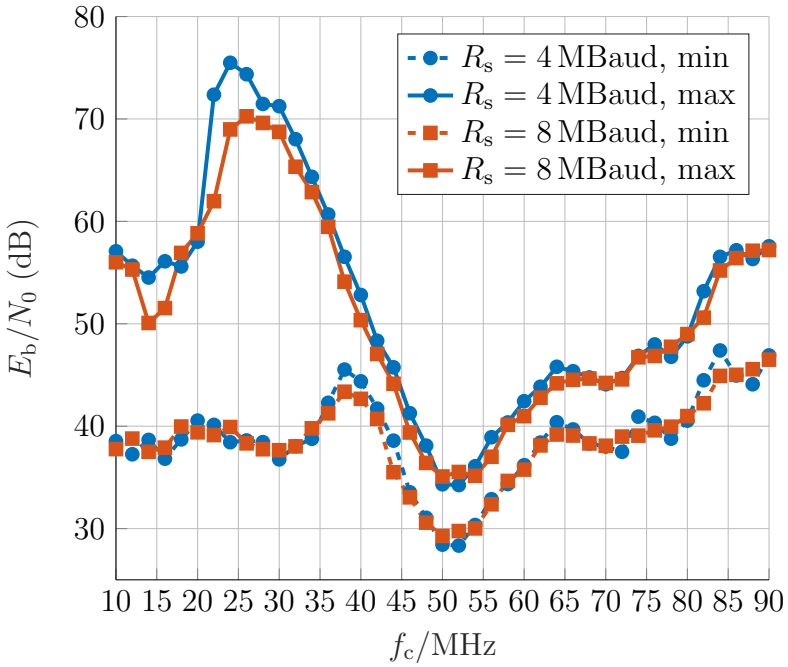

Figure 3.40: Minimum and maximum values (taken over all the battery cells) of the minimum E_b/N_0 required to (theoretically) reach maximum capacity using BPSK at $R_s = 4$ MBaud and $R_s = 8$ MBaud

Figure 3.40 shows the results obtained using BPSK modulation and symbol rates equal to 4 MBaud and 8 MBaud. The power efficiency of the PLC system can be improved by choosing a frequency range in which γ_{max} is low. In addition, it would be an advantage, if the difference between γ_{max} and γ_{min} is small in the selected frequency range because then strong transmit power variations can be avoided, particularly in case of flexible power allocation, and the complexity can be kept low. In Section 3.3, it is shown that, based on the channel and noise measurements, the frequency range from 40 MHz to 70 MHz is more suitable for a robust and power efficient data transmission than other frequency ranges. Furthermore, Section 3.4 shows that less ISI is expected to occur at frequencies above 40 MHz. Now that we have calculated the modulation-constrained channel capacity and determined thereupon the minimum and maximum values of the required minimum γ (taking all the battery cells into account), the carrier frequency selection becomes easier. For instance, the frequency range from 47.5 MHz to 56 MHz seems to best meet the aforementioned frequency selection criteria with a maximum of 35 dB for

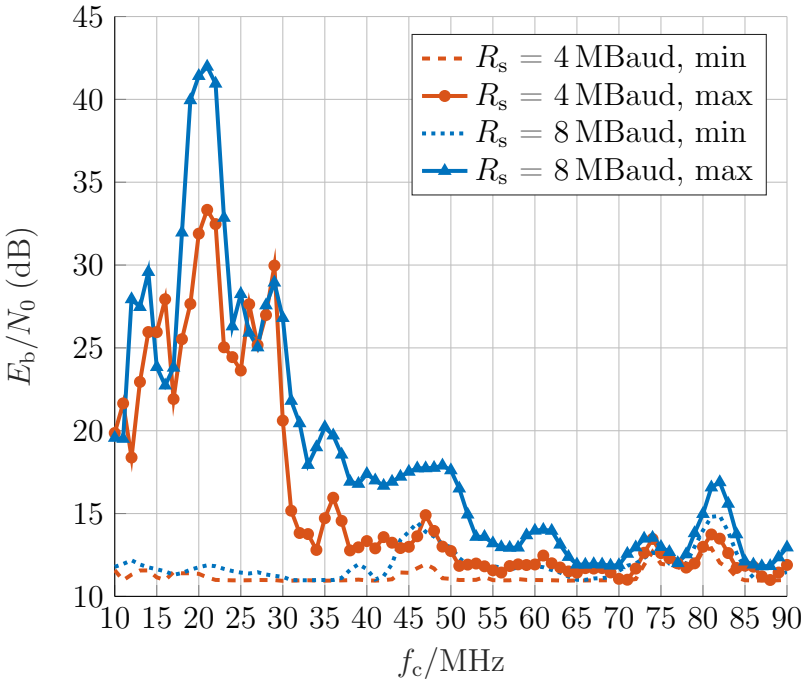

Figure 3.41: Minimum and maximum E_b/N_0 obtained with battery cells 1 to 48 at BER = 10^{-6}, R_s = 4 MBaud and R_s = 8 MBaud, using normalized channel impulse responses, BPSK and a 50-taps MMSE equalizer

γ_{max} and approximately 7 dB difference between γ_{max} and γ_{min}.

3.5.3.2 System complexity

The system complexity is another important aspect to take into account when designing a communications system. In Section 3.4, it is shown that the ISI strongly depends on the choice of the carrier frequency. Low-complexity channel equalization algorithms can be used without any loss in performance in case of channels with moderate frequency selectivity. If, however, the channel is highly frequency-selective, the complexity of the equalizer is expected to be high. In order to investigate how much ISI remains after equalization, we normalize the channel impulse response of the PLC channels to have unity gain and use BPSK/QPSK modulation along with a 50-tap MMSE equalizer.

Figures 3.41 and 3.42 display the E_b/N_0 obtained at BER = 10^{-6} with the symbol rates 4 MBaud and 16 MBaud. The frequency selectivity of the channel is expected to be higher at carrier frequencies with more residual ISI. From

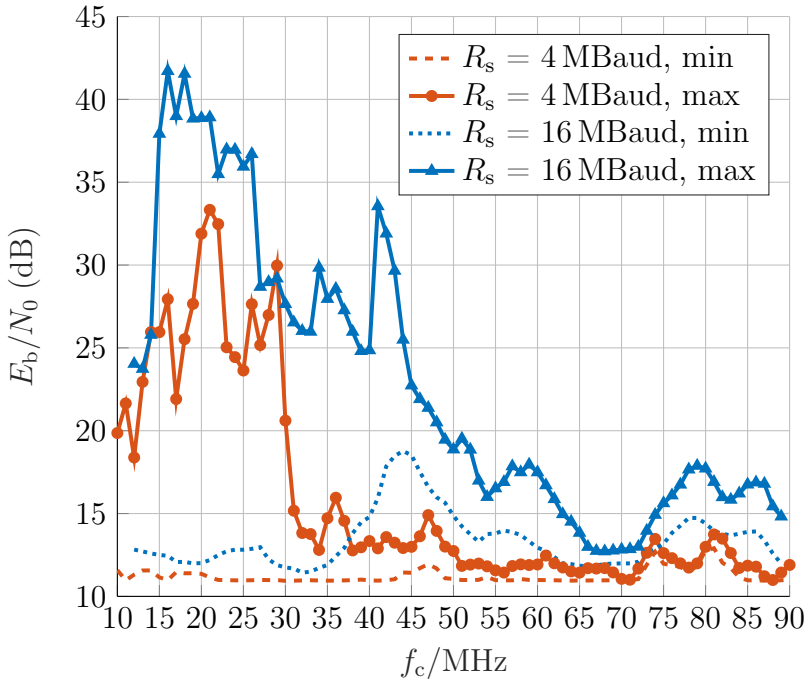

Figure 3.42: Minimum and maximum E_b/N_0 obtained with battery cells 1 to 48 at BER = 10^{-6} with R_s = 4 MBaud and R_s = 16 MBaud, using normalized channel impulse responses, BPSK and a 50-taps MMSE equalizer

the figures, it is clear that the PLC channel becomes less frequency-selective at higher carrier frequencies ($f_c \geq 50$ MHz). In addition, increasing the channel bandwidth causes the ISI to increase. Let γ_{ref} be the E_b/N_0 required to achieve a BER of 10^{-6} in an AWGN channel using BPSK modulation (γ_{ref} = 10.5 dB).

Table 3.5 includes the results obtained for the power loss relative to γ_{ref} in the frequency range 47.5 MHz to 56 MHz. The power loss is calculated for different symbol rates using the normalized impulse response of the PLC channels of battery cells 1 to 48. Also included is the maximum RMS delay spread taken over all the channels. From the table we can see that with R_s = 4 MBaud and $\tau_{rms} \leq 0.5T_s$, the residual ISI causes up to 4.5 dB power loss. It is also clear that with twice the symbol rate the power loss increases by at least 2 dB. A further increase in the symbol rate is accompanied with an increase of the RMS delay spread, which suggests that more residual ISI may exist. For instance, with a RMS delay spread of approximately $0.9T_s$ the residual ISI causes up to 11 dB power loss.

Symbol Rate	Power Loss	RMS Dealy Spread
4 MBaud	0.5 dB – 4.5 dB	$0.3T_s$ – $0.5T_s$
8 MBaud	2 dB – 7.5 dB	$0.6T_s$ – $0.8T_s$
16 MBaud	5.5 dB – 11 dB	$0.75T_s$ – $0.9T_s$

Table 3.5: Maximum power loss caused by the residual ISI in the frequency range 47.5 MHz to 56 MHz at BER = 10^{-6}, using BPSK and MMSE equalization (50-taps equalizer), compared to an AWGN channel

3.5.4 Single-carrier system

Different single-carrier modulation schemes are used to assess the physical layer performance of the PLC system. The BER simulations are performed assuming perfect carrier and symbol synchronization. For the channel equalization and channel coding, perfect channel knowledge is assumed. This is justified by the time-invariance of the PLC channel, which enables accurate channel estimation.

3.5.4.1 Channel equalization

The computational complexity of the equalization can be determined with respect to the number of floating-point operations (FLOPs) required by the selected algorithm. For instance, a linear MMSE equalizer with n_e taps requires $(2n_e - 1)$ FLOPs per symbol. A decision feedback equalizer, however, executes $(2n_f + 2n_b - 1)$ FLOPs per symbol, where n_f and n_b represent the length of the feedforward and the feedback filters, respectively. In the simulation, the length of the linear MMSE equalizer is chosen such that $\min\{F_{MSE}\} \leq 10^{-5}$ (refer to (2.23)). In case of the decision feedback equalizer, the feedforward filter is used to obtain a minimum-phase channel impulse response with zeros inside the unit circle. In other terms, all the zeros outside the unit circle are canceled in the feedforward path, while the zeros inside the unit circle are equalized by the feedback filter. As a result, the length of the feedback filter is determined by the number of zeros inside the unit circle and is, therefore, fixed. The length of the feedforward filter, however, should be determined iteratively by, for instance, applying the following method: we assume that the noise variance is equal to 0. In the first iteration ($k = 1$), n_f is set to 1. In each

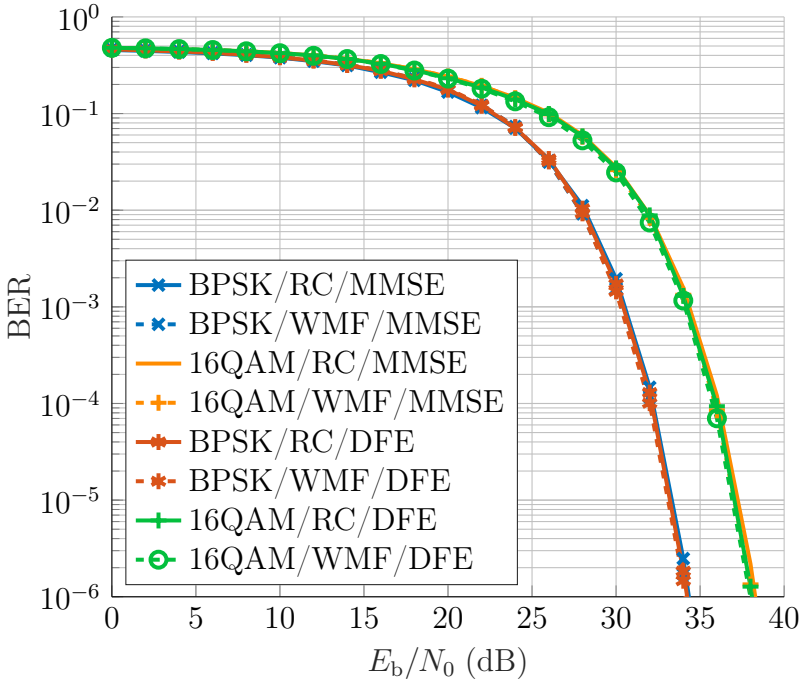

Figure 3.43: BER curves of battery cell №43 ($f_c = 52\,\text{MHz}$, $R_s = 4\,\text{MBaud}$) using single-carrier modulation, different filtering techniques and channel equalization (see Table 3.6)

iteration, n_f is incremented by a constant number of taps, while $\mathbf{e}$ and $\mathbf{b}$ are estimated as given in (2.27) and (2.28). The signal-to-interference ratio (SIR) is a function of $\mathbf{b}$ and can be calculated as follows:

$$\text{SIR}_k = 10\log_{10}\left(\frac{1}{\sum_{i=1}^{n_{b,k}} b_{i,k}}\right), \quad \text{with} \quad k \geq 1. \tag{3.77}$$

No more iterations are required once the condition $\text{SIR}_{k+1} - \text{SIR}_k = 0$ is satisfied. In Section 3.4, we have seen that the WMF decorrelates the colored noise and maximizes the SNR at the receiver. Therefore, the performance obtained with a WMF represents an upper bound on the performance of the filtering techniques used in the receiver. In comparison, the RC filter is suboptimal in terms of SNR maximization. In order to evaluate the physical layer performance in case of suboptimal filtering, we calculate the BER as a function of E_b/N_0, using single-carrier modulation and channel equalization. BPSK, QPSK and 16QAM are used for modulation. The results obtained with QPSK are the same as those obtained with BPSK. As can be seen in Figure 3.43, in the case of relatively good channels, RC filtering does not degrade the performance compared to the

Filtering	**Equalization Algorithm**	**Equalizer**
RC	MMSE	$n_\mathrm{e} = 15$
WMF	MMSE	$n_\mathrm{e} = 5$
RC	DFE	$n_\mathrm{f} = 6$, $n_\mathrm{b} = 2$
WMF	DFE	$n_\mathrm{f} = 1$, $n_\mathrm{b} = 1$

Table 3.6: Filtering techniques and channel equalization algorithms used to assess the BER performance of the physical layer (see Figure 3.43)

WMF. The results also show that from a complexity point of view it is better to use DFE than MMSE equalization. In addition, it is obvious that, when a WMF is used, the complexity of the decision feedback equalizer is reduced as illustrated in Table 3.6.

The performance of the MMSE equalization and the DFE depends on the distortion severity of the channel. We use different PLC channels and different single-carrier modulation schemes for the BER-simulations. In the remainder of this section, channel (1) refers to the PLC channel of cell Nº43 at the carrier frequency $f_\mathrm{c} = 52\,\mathrm{MHz}$. This channel is taken as an example of good channels with moderate ISI and attenuation (independently of the allocated bandwidth). On the other hand, channel (2) refers to the PLC channel of cell Nº6 at the carrier frequency $f_\mathrm{c} = 15\,\mathrm{MHz}$ and is one of the bad channels with high ISI and attenuation. Symbol rates between 4 MBaud and 20 MBaud are considered. Figure 3.44 shows the BER performance obtained in case of the good channel using BPSK modulation and RC filtering. QPSK provides the same results. It can be seen that in most of the cases DFE provides a similar or better performance than MMSE equalization at a significantly lower complexity. The same conclusion can be drawn from the BER results obtained with 16QAM and shown in Figure 3.45.

Finally, Figures 3.46 and 3.47 show that the communication over channel (1) requires 5 dB less E_b/N_0 compared to channel (2) in order to reach a BER of 10^{-6}.

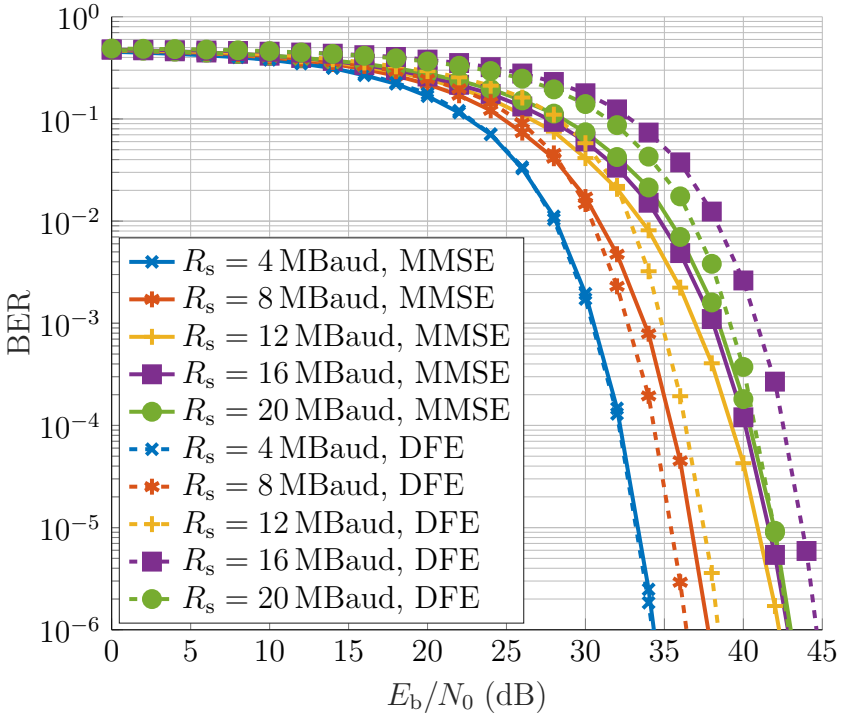

Figure 3.44: BER curves of battery cell Nº43 at 52 MHz using BPSK, RC filtering, MMSE/DFE equalization and different symbol rates (see Table 3.7)

Symbol Rate	**Equalization Algorithm**	**Equalizer**
4 MBaud	MMSE	$n_e = 15$
8 MBaud	MMSE	$n_e = 50$
12 MBaud	MMSE	$n_e = 125$
16 MBaud	MMSE	$n_e = 105$
20 MBaud	MMSE	$n_e = 50$
4 MBaud	DFE	$n_f = 6$, $n_b = 2$
8 MBaud	DFE	$n_f = 6$, $n_b = 4$
12 MBaud	DFE	$n_f = 6$, $n_b = 5$
16 MBaud	DFE	$n_f = 31$, $n_b = 5$
20 MBaud	DFE	$n_f = 16$, $n_b = 6$

Table 3.7: Channel equalizers used for the single-carrier implementation of the physical layer (see Figures 3.44 and 3.45)

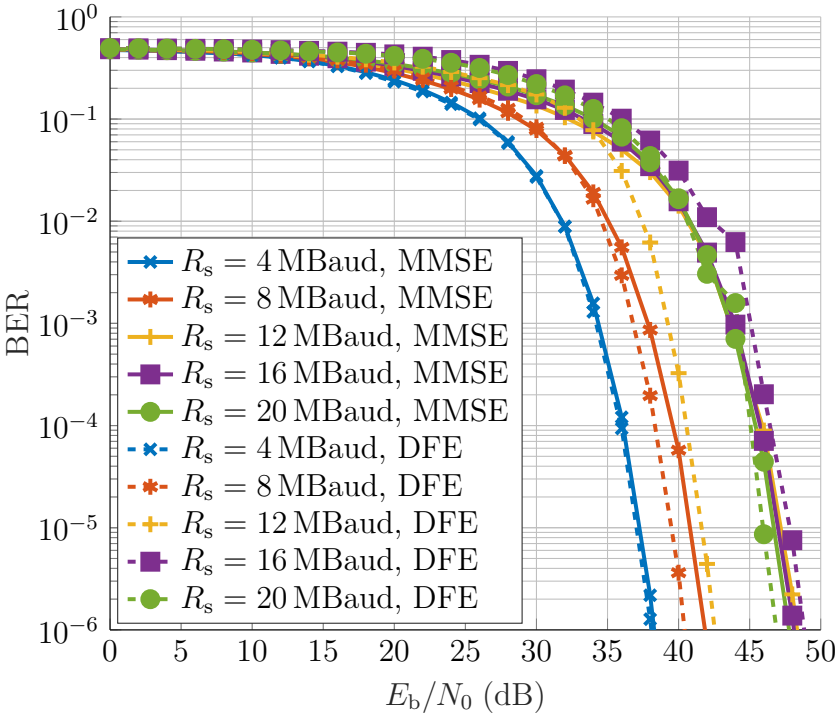

Figure 3.45: BER curves of battery cell №43 at 52 MHz using 16QAM, RC filtering, MMSE/DFE equalization and different symbol rates (see Table 3.7)

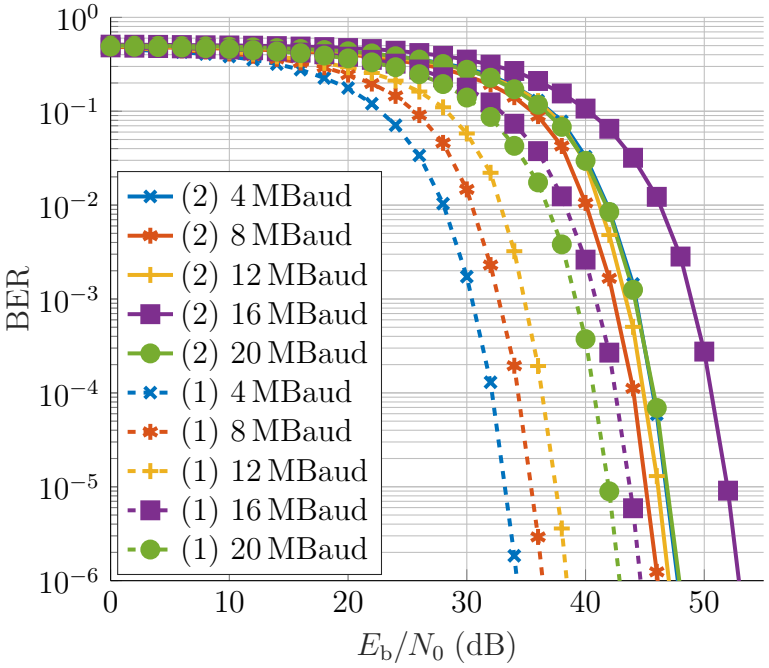

Figure 3.46: BER curves of channel (1) and channel (2) using BPSK, RC filtering, DFE and different symbol rates (see Table 3.8)

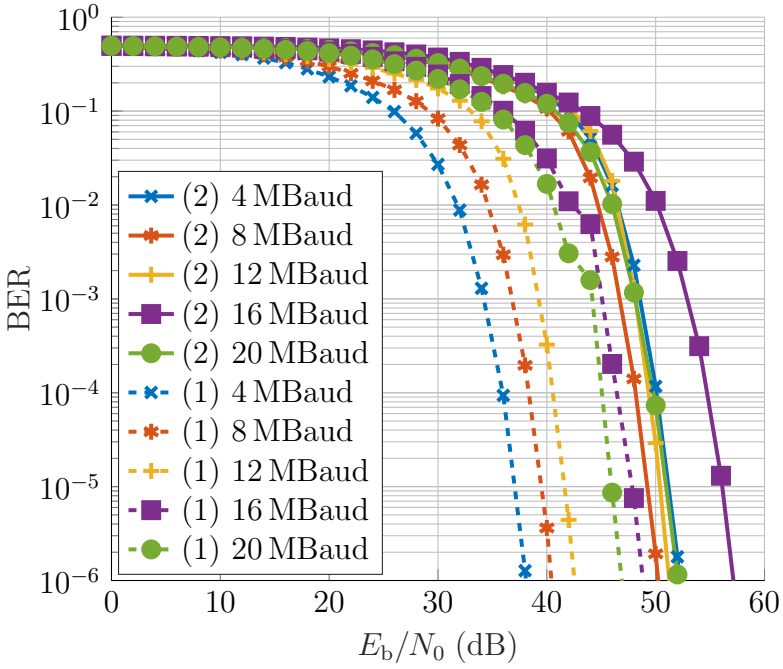

Figure 3.47: BER curves of channel (1) and channel (2) using 16QAM, RC filtering, DFE and different symbol rates (see Table 3.8)

PLC Channel	**Symbol Rate**	**DFE Equalizer**
(1)	4 MBaud	$n_f = 6$, $n_b = 2$
(1)	8 MBaud	$n_f = 6$, $n_b = 4$
(1)	12 MBaud	$n_f = 6$, $n_b = 5$
(1)	16 MBaud	$n_f = 31$, $n_b = 5$
(1)	20 MBaud	$n_f = 16$, $n_b = 6$
(2)	4 MBaud	$n_f = 6$, $n_b = 5$
(2)	8 MBaud	$n_f = 16$, $n_b = 11$
(2)	12 MBaud	$n_f = 11$, $n_b = 13$
(2)	16 MBaud	$n_f = 46$, $n_b = 13$
(2)	20 MBaud	$n_f = 11$, $n_b = 13$

Table 3.8: Decision feedback equalization in the case of channel (1) and channel (2), using different symbol rates

PLC Channel	Modulation Scheme	Equalizer	
		n_f	n_b
(1)	BPSK	31	5
(1)	QPSK	6	4
(1)	16QAM	6	2
(2)	BPSK	46	13
(2)	QPSK	16	11
(2)	16QAM	6	5

Table 3.9: Decision feedback equalizers in the case of channel (1) and channel (2), using different modulation schemes at 16 Mbit/s

3.5.4.2 Higher order modulation

In order to be able to compare the performance of different linear modulation schemes, we assume a fixed target data rate. When the modulation order increases, the symbol rate becomes smaller and less bandwidth needs to be allocated for data transmission. Figure 3.48 shows, using the example of the PLC channels (1) and (2), that higher order modulation schemes outperform BPSK and are, in addition, more bandwidth and energy efficient. Furthermore, based on Table 3.9, it is obvious that the complexity of DFE is reduced when the channel becomes narrower or more precisely, when less ISI needs to be mitigated.

QPSK outperforms BPSK by at least 5 dB at BER = 10^{-6}. QPSK also outperforms 16QAM by approximately 5 dB in case of channel (2) and by 2 dB in case of channel (1). Based on these results, it can be concluded that in terms of BER performance QPSK is the best choice. In case, however, the bandwidth efficiency is a major concern, it is possible to use 16QAM instead of QPSK. On the other hand, the results reveal that decision feedback equalizers with relatively low complexity allow to obtain a good performance, even in case of high symbol rates (up to 20 MBaud). Consequently, a low-complexity single-carrier implementation can be used for PLC without compromising the performance.

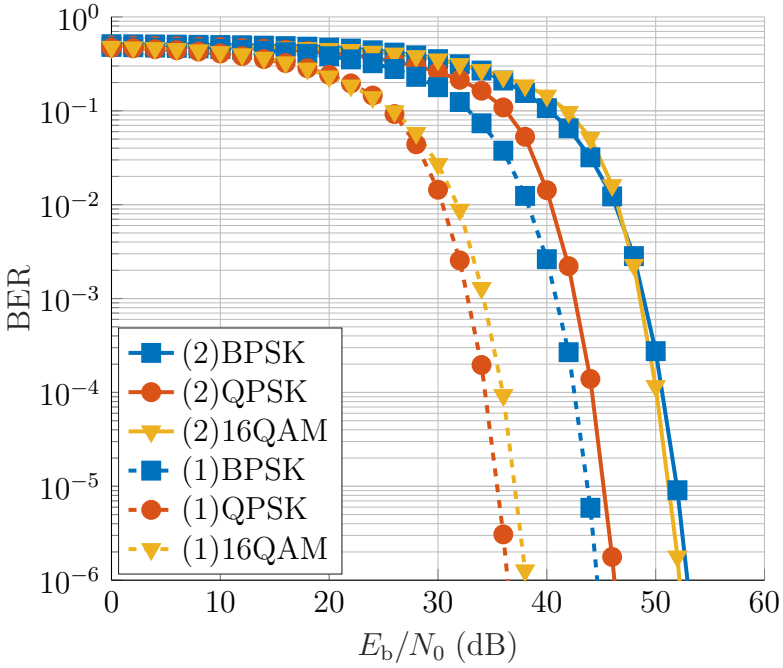

Figure 3.48: BER curves of channel (1) and channel (2) using different linear modulation schemes and DFE at 16 Mbit/s (see Table 3.9)

3.5.4.3 Channel coding

In channel coding, the key design parameters are coding gain, rate penalty and bandwidth expansion. The coding gain describes the difference in the SNR between the coded and the uncoded systems at the same BER. At low SNRs some codes have negative coding gain. Block, convolutional and concatenated codes allow to improve the effective SNR at the cost of bandwidth expansion or data rate reduction (in case of fixed channel bandwidth). Assuming R_c is the code rate. Then the bandwidth expansion ratio is given by

$$\frac{W_{\text{coded}}}{W_{\text{uncoded}}} = \frac{1}{R_c}, \quad \text{with} \quad R_c = \frac{k}{n}. \tag{3.78}$$

Let E_b be the information bit energy, required in the uncoded case to reach a specific target BER, and $E_{b,c}$ be the information bit energy, required in the coded case to reach the same BER. When channel coding is used, less energy would be required to achieve a specific BER and the coding gain can be expressed as

$$G_c = 10\log(\lambda), \quad \text{with} \quad \lambda = \frac{E_b}{E_{b,c}}. \tag{3.79}$$

In order to determine the coding gain, we have to calculate λ. Let E_c be the energy per codebit. Then E_c can be expressed as

$$E_\mathrm{c} = R_\mathrm{c} E_\mathrm{b,c} \overset{(3.79)}{=} R_\mathrm{c} \frac{E_\mathrm{b}}{\lambda}. \tag{3.80}$$

A small code rate reduces the energy per codeword bit, which results in an increase of the error probability. Nevertheless, the error correction capability of channel codes typically compensates for this reduction, especially at high SNRs [35].

3.5.4.3.1 Block codes The error probability achieved with an (n, k) linear block code depends on the minimum Hamming distance d_min, upperbounded by $(n - k + 1)$, where n is the length of the codeword in bits and k is the number of information bits. A codeword is decoded to the correct word if the contained number of errors t satisfied the following condition [56]:

$$t \leq \left\lfloor \tilde{t} \right\rfloor, \quad \text{with} \quad \tilde{t} = 0.5\,(d_\mathrm{min} - 1) \tag{3.81}$$

where $\lfloor \tilde{t} \rfloor$ denotes the largest integer less than or equal to $\tilde{t}$. Cyclic codes are a subclass of linear block codes, where all codewords in a given code are cyclic shifts of one another. Cyclic codes are advantageous when it comes to the encoding and decoding techniques, as explained in [56]. Bose-Chaudhuri-Hocquenghem (BCH) codes are a subclass of cyclic codes, using a particularly efficient decoding algorithm, the so called Berlekamp-Massey algorithm. It can be shown that for any positive integers m and t, there exists a BCH code with the following parameters [56]:

$$n = 2^m - 1, \qquad (n - k) \leq mt \qquad \text{and} \qquad d_\mathrm{min} = 2t + 1. \tag{3.82}$$

The codeword error probability P_e is the probability that a transmitted codeword is decoded erroneously and depends on whether the decoder uses soft or hard decision. P_e is upperbounded by the probability that more than t errors occur. Since the bit errors in a codeword occur independently in an AWGN channel, this probability is given according to [35] by:

$$P_\mathrm{e} \leq \sum_{j=t+1}^{n} \binom{n}{j} p^j \,(1-p)^{n-j}\,, \tag{3.83}$$

Code	Rate	t	Coding Gain (in dB)								
			$\mathbf{BER = 10^{-3}}$			$\mathbf{BER = 10^{-4}}$			$\mathbf{BER = 10^{-6}}$		
			BPSK	8PSK	16QAM	BPSK	8PSK	16QAM	BPSK	8PSK	16QAM
(31,26)	0.84	1	1.04	1.21	1.16	1.39	1.54	1.49	1.74	1.85	1.81
(31,21)	0.68	2	1.32	1.65	1.54	1.79	2.08	1.99	2.29	2.51	2.45
(31,16)	0.52	3	1.1	1.59	1.44	1.63	2.05	1.92	2.21	2.53	2.43
(63,57)	0.9	1	0.97	1.1	1.06	1.4	1.52	1.48	1.84	1.94	1.91
(63,51)	0.81	2	1.42	1.66	1.58	2.01	2.23	2.16	2.66	2.84	2.79
(63,45)	0.71	3	1.61	1.95	1.84	2.28	2.6	2.5	3.04	3.31	3.23
(63,39)	0.62	4	1.61	2.05	1.91	2.33	2.73	2.61	3.16	3.5	3.39
(63,36)	0.57	5	1.82	2.36	2.19	2.57	3.06	2.91	3.44	3.85	3.72
(127,120)	0.94	1	0.81	0.9	0.87	1.29	1.39	1.36	1.82	1.91	1.88
(127,113)	0.89	2	1.27	1.44	1.38	1.94	2.11	2.06	2.7	2.86	2.81
(127,106)	0.83	3	1.56	1.79	1.72	2.32	2.57	2.49	3.22	3.44	3.38
(127,99)	0.78	4	1.74	2.04	1.94	2.56	2.87	2.77	3.55	3.82	3.74
(127,92)	0.72	5	1.84	2.2	2.09	2.7	3.07	2.95	3.75	4.08	3.98
(127,85)	0.67	6	1.87	2.29	2.16	2.77	3.18	3.05	3.85	4.23	4.11
(127,78)	0.61	7	1.84	2.33	2.17	2.76	3.23	3.09	3.88	4.3	4.17
(127,71)	0.56	8	1.76	2.3	2.13	2.69	3.22	3.05	3.83	4.3	4.16
(127,64)	0.5	9	1.61	2.21	2.02	2.55	3.14	2.95	3.71	4.23	4.07

Table 3.10: Numerically calculated coding gain of selected BCH codes with different linear modulation schemes and at different BERs in an AWGN channel

where p is the codebit error probability at the input of the decoder.

Block codes are random error-correcting codes. The assumption of independently generated errors is valid in AWGN channels. In some other physical channels, however, errors might not be random. Deep fades for example cause a large number of errors in sequence. Interleaving can be used to distribute the burst errors over many codewords, so that a small number of errors appears in each block, resulting in a smaller codeword error probability. In the following, we assume hard decision decoding. As shown in [35], the Chernoff bound provides a tight upper bound on the codeword error probability, given as

$$P_{\mathrm{e}} \leq \left(2^k - 1\right) \left[4p(1-p)\right]^{d_{\min}/2}. \tag{3.84}$$

At high SNRs, we can assume that one codeword error corresponds to a single bit error. We can, thus, substitute P_{e} in (3.84) with kP_{b} [35]. p is a function of E_{c}. For instance in case of coherent BPSK, p is equal to $Q\left(\sqrt{2E_{\mathrm{c}}/N_0}\right)$ as shown in (2.5) in Section 2.4. Thus, E_{c} can be determined as a function of R_{c}, P_{b} and $E_{\mathrm{b,c}}$. The latter can be taken from the BER curve of the modulation scheme under consideration in an AWGN channel. From the expression obtained for E_{c} we can derive the coding gain as shown in (3.79) and (3.80). We choose BCH codes with different error correction capabilities and different code rates and calculate the coding gain at different BERs, using different modulation schemes (BPSK/QPSK, 8PSK and 16QAM). Table 3.10 shows the results obtained using some of the BCH codes defined in [57]. The coding gain varies by less than 0.5 dB between the different modulation schemes at the same BER. The smaller the BER, the higher the coding gain in the considered range. Using the (63, 45) BCH code, an SNR gain of approximately 3 dB is achieved at BER $= 10^{-6}$. With $t = 3$ and $R_{\mathrm{c}} = 0.71$, the (63, 45) BCH code provides a good compromise between performance, complexity and bandwidth expansion.

In a next step, we perform BER simulations for the PLC channel using channel equalization and channel coding and compare the coding gain results with those obtained in an AWGN channel. Using QPSK and a symbol rate of 8 MBaud, we obtain the BER curves shown in Figure 3.49 for channel (2), where DFE ($n_{\mathrm{f}} = 11$, $n_{\mathrm{b}} = 6$), and different BCH codes are used. As can be seen, up to 3 dB coding gain can be achieved at BER $= 10^{-6}$. These results are quite close to those of the AWGN channel. As shown in Section 3.5.4.1,

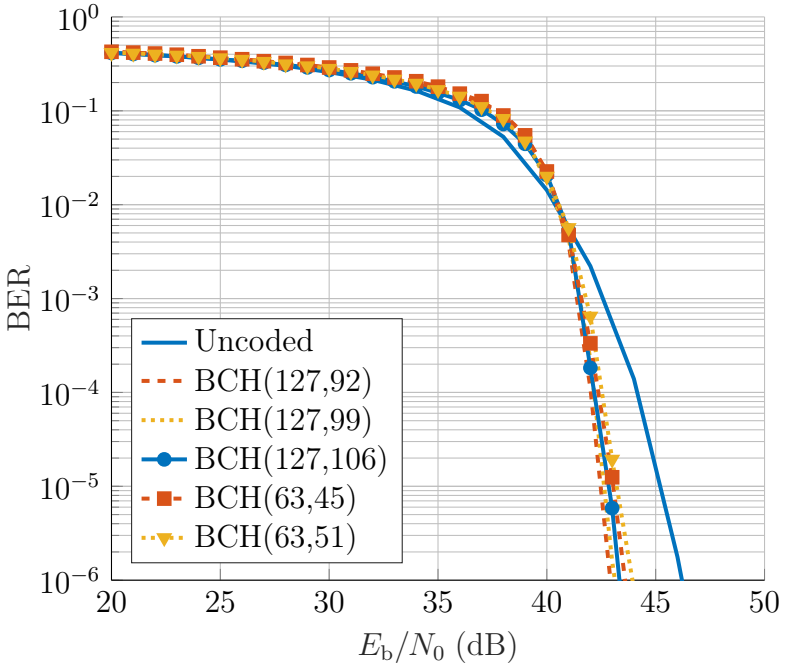

Figure 3.49: BER curves of channel (2), using QPSK and DFE ($n_f = 11$, $n_b = 6$) and different BCH codes at 8 MBaud

channel (2) is an example of bad channels in terms of ISI and attenuation. In the case of good channels, we obtain comparable results with regard to the coding gain.

3.5.4.3.2 Convolutional codes In convolutional codes, linear shift registers are used to produce codewords. In this work, we focus on $1/n$-rate convolutional codes, where n is the number of codebits. The encoder consists of a cascade of L shift registers. The n output bits are obtained by XOR-ing the contents of some of the L shift registers as defined by the generator polynomial. The Viterbi algorithm provides maximum-likelihood (ML) decoding for convolutional codes. The complexity of the algorithm increases exponentially with the constraint length $K = L + 1$. Thus, it can be applied only to codes with a low constraint length. Otherwise, the decoding delay and the amount of memory required would be practically infeasible [56]. In practice, path-memory truncation is applied to reduce complexity. For a 1/2-rate code, a traceback depth of five times the memory of a convolutional code is sufficient to obtain good results. For an arbitrary code rate, a more accurate rule of thumb is

K	Rate 2/3	Rate 3/4	Rate 4/5	Rate 5/6	Rate 6/7	Rate 7/8
3	10	101	1011	10111	101111	1011111
	11	110	1100	11000	110000	1100000
4	11	110	1011	10100	100011	1000010
	10	101	1100	11011	111100	1111101
5	11	101	1010	10111	101010	1010011
	10	110	1101	11000	110101	1101100

Table 3.11: Puncturing matrices used to produce punctured convolutional codes with different constraint lengths and code rates between 2/3 and 7/8 from a 1/2-rate mother code [33]

$2.5m/(1 - R_c)$, where the code memory m is equal to the number of shift registers. For a punctured code, the same rule applies, where m is the memory of the mother code and R_c is the rate of the punctured code [58]. Puncturing allows to vary the code rate without changing the entire encoder structure. It is typically used to increase the data rate by dropping some of the codebits at the output of the encoder. Table 3.11 shows some of the puncturing patterns, used to produce punctured convolutional codes with different constraint lengths and code rates between 2/3 and 7/8, from a 1/2-rate code. We use the same patterns to calculate the coding gain in an AWGN channel. Figure 3.50 shows the coding gain results of some convolutional codes as a function of the code rate. The generator polynomials are given in octal representation and the traceback depth is chosen equal to $5m/(1 - R_c)$. As expected, the coding gain becomes smaller as the code rate increases. At the same time, increasing the constraint length allows to achieve a higher coding gain at the expense of an increased complexity. In conclusion, we can say that, with respect to complexity and performance, block codes are preferred, especially because of the bursty data transmission.

3.5.5 Multi-carrier system

OFDM divides the channel bandwidth into multiple flat fading subchannels. ISI is avoided using a guard interval between the symbols. The guard interval

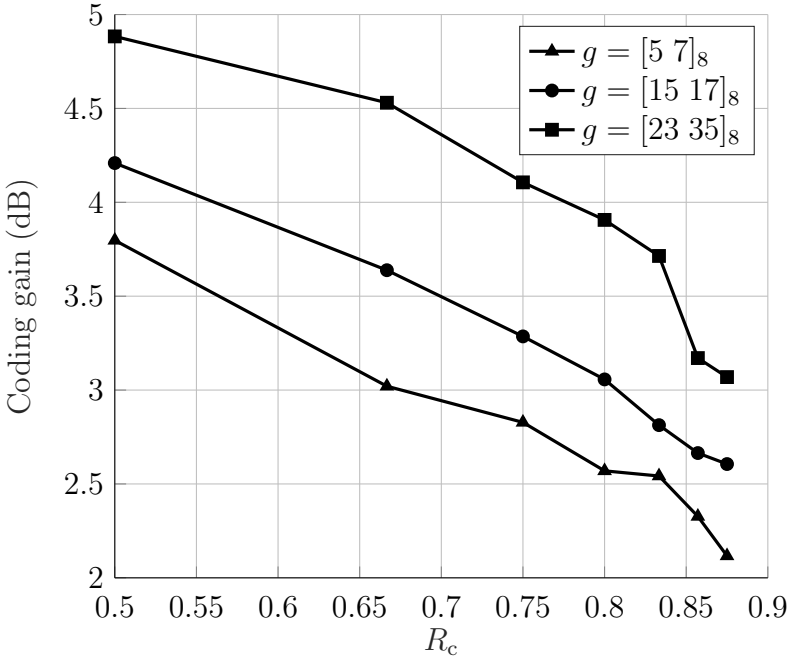

Figure 3.50: Coding gain of selected convolutional codes with puncturing (1/2-rate mother code) using BPSK in an AWGN channel (BER = 10^{-5})

is filled up with a cyclic prefix (CP). As long as the CP length is greater than the channel delay spread, the ISI is completely eliminated. On the downside, the use of cyclic prefix entails data rate and power losses [42].

Using the example of channel (2), Figure 3.51 shows a comparison between the BER performance of QPSK with DFE ($n_\mathrm{f} = 11$, $n_\mathrm{b} = 6$) and that of OFDM with QPSK modulation and MMSE equalization, where the number N_c of subchannels is equal to 256 and the guard interval N_G is equal to 1/8 of the OFDM symbol duration. The single-carrier implementation uses BCH (127, 64) for channel coding, while the multi-carrier implementation uses frequency interleaving and a concatenated code, consisting of a convolutional 2/3-rate inner code ($g_1 = [23\ 35\ 0]_8, g_2 = [0\ 5\ 13]_8$), and a (32, 24) Reed-Solomon (RS) outer code. RS codes are non-binary BCH codes, suitable for use in conjunction with M-ary modulation and useful for channels with burst errors. An (N, K) RS code maps K M-ary symbols into N M-ary symbols such that $N = 2^k - 1$, $K \in \{1, 3, \cdots, N-2\}$ and $R_\mathrm{c} = K/N$. According to [35], the code is capable of correcting up to

$$t = \frac{D_\mathrm{min} - 1}{2} \tag{3.85}$$

symbol errors, where $D_{\min} = N - K + 1$. Concatenated codes typically achieve very low error probability with less complexity compared to a single code with the same error probability performance. The inner and outer codes are separated by an interleaver to distribute burst errors and reduce the symbol errors. The ML decoder for a concatenated code performs joint decoding and is typically highly complex. A suboptimal technique for decoding consists in decoding the concatenated code in two stages, first the inner code followed by the outer code decoding [35].

As can be seen in Figure 3.51, interleaving and channel coding improve the performance of OFDM by approximately 10 dB at BER = 10^{-6}. Nevertheless, uncoded BPSK outperforms coded OFDM by at least 2 dB. This result can be explained as follows: in a time-invariant and frequency-selective channel, such as the PLC channel, the BER performance of uncoded single-carrier modulation is driven by the average channel attenuation. For example, assuming there are no severe notches in the CFR, if BPSK is used the BER can be approximated by

$$P_{\mathrm{b}} \approx Q\left(\sqrt{\frac{2E_{\mathrm{b}}}{N_0} \cdot \alpha_{\mathrm{h}}}\right), \tag{3.86}$$

where α_{h} is the average attenuation of the channel calculated as

$$\alpha_{\mathrm{h}} = \frac{1}{B} \int_{-B/2}^{B/2} |C(f)|^2 \, \mathrm{d}f. \tag{3.87}$$

However, in the case of OFDM, the BER can be approximated by the average over the BERs of the subchannels. Using for instance BPSK for subcarrier modulation, we obtain

$$P_{\mathrm{b}} \approx \frac{1}{N_{\mathrm{c}}} \sum_{i=1}^{N_{\mathrm{c}}} Q\left(\sqrt{\frac{2E_{\mathrm{b}}}{N_0} \cdot \alpha_{\mathrm{h},i}}\right), \tag{3.88}$$

where $\alpha_{\mathrm{h},i}$ denotes the attenuation of the i-th subchannel. This causes the average bit error rate of an OFDM system in a frequency-selective channel to be dominated by the subchannels with high attenuation. Interleaving and channel coding allow to mitigate this effect by distributing the information across all subcarriers. Nevertheless, in our case, coded OFDM does not seem to provide a better BER performance than single-carrier. In addition, OFDM causes a

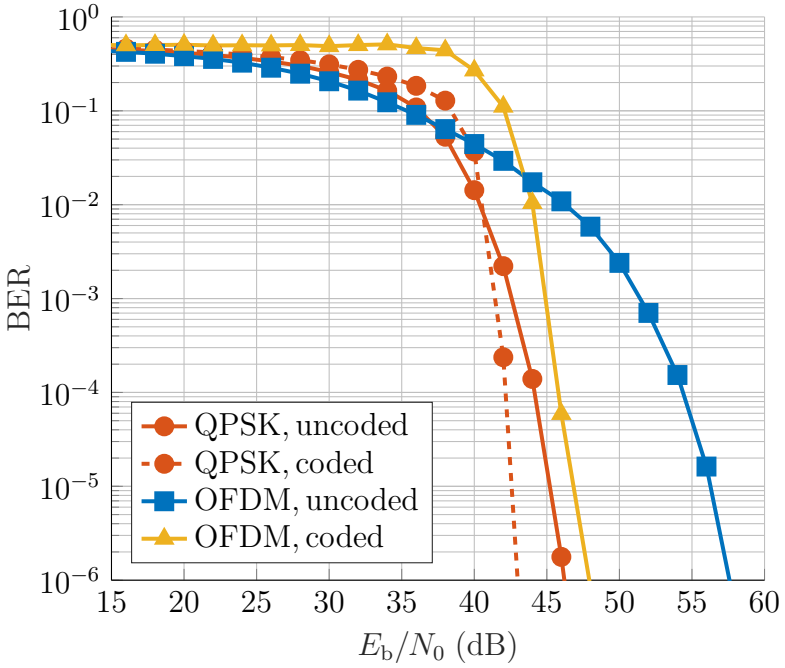

Figure 3.51: BER curves of of channel (2), using single- and multi-carrier modulation schemes with $R_s = 8\,\text{MBaud}$, $N_c = 256$ and $N_G = 1/8$

higher latency for data processing at the receiver, and the cyclic prefix leads to an increase of the SNR required to achieved a specific BER. For these reasons, a single-carrier system seems to be the better choice for our PLC system.

Chapter 4

Conclusion

Most studies related to automotive PLC deal with the electrical power supply system of the automobile and very few of them address the use of PLC in other automotive applications. This thesis focuses on a new application field of PLC and investigates the suitability of PLC for battery management in large-scale lithium-ion traction batteries. PLC enables the use of the existing battery powerlines for data communication. Thus, it reduces the wiring harness and saves space, weight and cost.

In order to keep up with the constantly evolving battery technologies, BMSs need to use highly accurate condition monitoring algorithms. In addition, a large amount of data needs to be continuously collected and processed with high reliability in order to accurately monitor a large battery with up to 100 cells. In other terms, a high-speed communication is required between the central battery pack control unit and the cell monitoring and control units, especially when the BMS has a master-slave architecture and the battery cells have to be constantly supervised and individually controlled.

The main goal of this thesis was to figure out how robust a data communication over the battery powerline is and whether high data rates can be achieved using state-of-the-art techniques for digital data transmission, channel equalization and channel coding. Under the assumption of a bursty data transmission, we showed that TDMA is the preferred channel access scheme for our application and that a half-duplex PLC system is the best choice in case of asymmetric data traffic in the up- and downlinks. Half-duplexing can be realized using TDD and has the advantage of an effective power control in

reciprocal channels. Using TDMA, a deterministic data communication with time-triggered control and periodic signal transmission is possible. TDMA also benefits from the implicit frequency diversity of the frequency-selective PLC channels.

In this thesis, we introduced an approach on how to calculate the minimum required transmission data rate as a function of the number of battery cells, the update rates of the cell measurements and the cell data length. The update rates of the different cell measurements (voltage, temperature and pressure) can be either equal or different. We considered these two cases to determine the minimum required data rate. We showed that in case of equal measurement update rates, data rates above 7 Mbit/s are required only if the update period is shorter than 1 ms, assuming a battery pack with 100 cells, a channel code rate equal to 2/3, a 20% data overhead and a cell data length above 40 bits (without overhead). With an update period of 1 ms, every additional 10 bits of the cell data result in an increase of the data rate by 2 Mbit/s, in case of a battery with 100 cells. Furthermore, the data rate increases by 75 kbit/s per additional cell, in case the cell data length is equal to 40 bits. In case, however, the cell data length is equal to 100 bits, the expected increase of the data rate equals 200 kbit/s per additional cell. A much smaller data rate is required in case the measurement updates take longer than 5 ms. In fact, a data rate between 1.5 Mbit/s and 4 Mbit/s seems to be sufficient. With an update period of 5 ms, the data rate increases by 50 kbit/s with each additional battery cell, assuming the cell data length is equal to 100 bits. We also considered the case of different measurement update rates and showed that the minimum required data rate is below 2.5 Mbit/s, when the data updates take place within time periods longer than 5 ms. In case, however, one of the measurement updates happens once every 1 ms, a data rate between 4 Mbit/s and 6 Mbit/s is expected. Based on the obtained results, we could show that the need for high data rates can be attributed to high measurement update rates, in addition to the large amount of data to be exchanged. We also showed that depending on the system requirements and whether or not, the measurement update rates are equal, there are different possibilities for designing the TDMA schedule such that the channel utilization is optimized and the data rate is kept as low as possible.

Following the data rate derivation, we focused on the transfer characteristics

of the PLC channel in the HF range. We first investigated the RF properties of 40 Ah and 60 Ah battery cells by measuring the AC-impedance of dummy prismatic cells and their individual components such as the top cap, the current collectors and the cell case. We created lumped circuit models for the different cell components and used them to model single cells, where the circuit parameters were obtained by means of semi-empirical data fitting. We showed that single battery cells have an equivalent inductance value between 20 nH and 30 nH. We also measured the impedance of a series-connection of up to six cells and showed how challenging modeling large scale battery can be as the impedance does not increase proportionally with the number of cells. In a next step, we measured the channel transfer characteristics in the frequency domain and analyzed the channel frequency selectivity as a function of the carrier frequency and the allocated channel bandwidth. We considered channel bandwidths up to 20 MHz. The results obtained for the RMS delay spread of the PLC channel suggest that less ISI is expected at frequencies above 40 MHz. Furthermore, we defined some of the driving scenarios, for which noise measurements were conducted. The measurement results showed that the noise is impulsive and can be classified into periodic and aperiodic noise, depending on the driving scenario. In addition, we provided a statistical noise model by calculating the arithmetic mean and the standard deviation of the pulse width, the inter-arrival time and the pulse energy. We compared the measured noise signals to those obtained using the model, both in the time and frequency domains. The comparison showed a good match between the measurements and the model.

Based on the channel measurements, we created an equivalent baseband channel model, where the channel was assumed to be time-invariant and the noise was assumed to be AWGN. The AWGN assumption is based on the fact that the power spectral density of the impulsive noise is significantly below the noise floor at frequencies above 40 MHz. We showed that the HMM can be used to model the frequency-selective and time-invariant PLC channel and that the structure of the Markov chain can be exploited to determine the a posteriori probabilities of the transmit symbols conditioned on the observation of a noisy version of the received symbols. With the help of the BCJR algorithm, we were able to numerically calculate the a posteriori probabilities and use them

to estimate the modulation-constrained channel capacity as a function of the position of the battery cell in the pack, the carrier frequency, the allocated channel bandwidth and the bit energy to noise density ratio E_b/N_0. From the capacity results, we could determine the required minimum E_b/N_0 to reach the maximum channel capacity. Thereupon, we showed that the power efficiency of the PLC system depends on the choice of the carrier frequency and whether a fixed or a flexible power allocation is adopted. If the power allocation is fixed and equal, all CMUs would have the same transmit power. If, however, the power allocation is flexible, the transmit power can be adapted to the channel, which helps to optimize the power consumption of the CMUs. The capacity results showed that the smallest required E_b/N_0, which would allow to reach the maximum channel capacity, is obtained in the frequency range 47.5 MHz to 56 MHz. From the physical layer simulations performed with single-carrier modulation and channel equalization, we could also observe that the PLC channel suffers less from ISI in the aforementioned frequency range. For these reasons, we considered this frequency range to be best suited for a robust data transmission.

After having dealt with the question of how to choose the carrier frequency, we discussed the relation between the choice of the modulation scheme, the spectral efficiency and the BER performance. We highlighted the advantages single-carrier schemes such as PSK and QAM have over multi-carrier schemes, in the case of PLC channels with moderate frequency selectivity. We used the example of OFDM, where the use of cyclic prefix entails data rate and power losses, in addition to the relatively high PAPR and the sensitivity to subcarrier fading and ICI. Furthermore, we compared the performance and complexity of DFE and MMSE equalization, using different single-carrier modulation schemes, different symbol rates and PLC channels of different battery cells. We showed how to estimate the coefficients of a linear MMSE filter assuming perfect channel knowledge. We also showed how to determine the coefficients of the feedforward and feedback filters of decision feedback equalizers. In order to evaluate the computational complexity of the equalization, we used the number of FLOPs, which can be calculated from the number of coefficients of the equalizer filter(s). We showed that, depending on the carrier frequency and the channel bandwidth, DFE provides a similar or better performance

than MMSE at a significantly lower complexity. The results also revealed that DFE equalizers with relatively low complexity allow to achieve a BER of 10^{-6} with an E_b/N_0 value between 35 dB and 45 dB, when the symbol rate varies between 4 MBaud and 20 MBaud in the frequency range from 47.5 MHz to 56 MHz. Consequently, we could conclude that a low-complexity single-carrier system can be used for PLC for symbol rates up to 20 MBaud.

In a further step, we numerically calculated the coding gain of BCH codes in an AWGN channel at different BERs. We compared the results and chose some of the codes to perform the BER simulations using the PLC channel. Similarly, we calculated the coding gain of selected convolutional codes with puncturing in an AWGN channel and showed that, with respect to complexity and performance, block codes are the better choice, especially because of the bursty data transmission. Finally, we presented the BER results of single- and multi-carrier modulation with equalization and channel coding and showed that coded OFDM does not seem to provide a better BER performance than single-carrier implementations. Therefore, we could conclude that a single-carrier-based physical layer implementation with DFE and block code-based channel coding is well-suited for PLC in automotive BMSs.

In this thesis, we assumed that the PLC channel is time-invariant. Thus, we did not consider adaptive digital modulation techniques, nor did we deal with adaptive channel equalization. Furthermore, the results of the thesis primarily apply to the battery pack which was used for the channel measurements. Therefore, similar investigations can be performed using other battery models in order to develop a better understanding of the impact of the battery design on the PLC channel. 3D-battery models and FEM-based simulations can also be used to measure the channel attenuation, if real world channel measurements are difficult to perform or reproduce. Based on the results presented in this thesis, a demonstrator can be developed in order to conduct in-vehicle testing and assess the performance of the physical layer algorithms, under real world conditions and at different symbol rates and carrier frequencies. The test results can be used to optimize the physical layer. In a next step, the MAC protocol can be implemented in order to test how well the data communication works in both up- and downlink directions, using multiple channel access.

Bibliography

[1] **Fotouhi, A., Auger, D.J., Propp, K., Longo, S. and Wild, M.** *A review on electric vehicle battery modelling. Renewable and Sustainable Energy Reviews*, 56:1008–1021, 2016.

[2] **Hariharan, K.S., Tagade, P. and Ramachandran, S.** *Mathematical Modeling of Lithium Batteries: From Electrochemical Models to State Estimator Algorithms.* Green Energy and Technology. Springer International Publishing, 2017.

[3] **Schneider, M., Ilgin, S., Jegenhorst, N., Kube, R., Puttjer, S., Riemschneider, K. and Vollmer, J.** *Automotive battery monitoring by wireless cell sensors. Conference Record - IEEE Instrumentation and Measurement Technology Conference*, 2012.

[4] **Alonso, D., Opalko, O., Sigle, M. and Dostert, K.** *Towards a Wireless Battery Management System: Evaluation of Antennas and Radio Channel Measurements Inside a Battery Emulator.* In *2014 IEEE 80th Vehicular Technology Conference (VTC2014-Fall)*, pages 1–5, 2014.

[5] **Alonso, D., Opalko, O. and Dostert, K.** *Physical layer performance analysis of a wireless data transmission approach for automotive lithium-ion batteries.* In *2015 IEEE Vehicular Networking Conference (VNC)*, pages 235–242, 2015.

[6] **Alonso, D., Opalko, O. and Dostert, K.** *Channel Measurements and Simulations with Planar Inverted F-Antennas in an Enhanced Testbed for a Wireless Battery Management System.* In *WSA 2015 19th International ITG Workshop on Smart Antennas*, pages 1–8, 2015.

[7] **Alonso, D., Winkler, C., Opalko, O. and Dostert, K.** *Prototyping of the physical and MAC layers of a wireless battery management system.* In *2015 IEEE Vehicular Networking Conference (VNC)*, pages 267–270, 2015.

[8] **Lee, M., Lee, J., Lee, I., Lee, J. and Chon, A.** *Wireless battery management system.* In *2013 World Electric Vehicle Symposium and Exhibition (EVS27)*, pages 1–5, 2013.

[9] **Wenger, M.M., Filimon, R., Lorentz, V.R.H. and März, M.** *A robust contactless capacitive communication link for high power battery systems.* In *2014 IEEE 23rd International Symposium on Industrial Electronics (ISIE)*, pages 1766–1772, 2014.

[10] **Opalko, O.** *Powerline-Kommunikation für Batteriemanagement-Systeme in Elektro- und Hybridfahrzeugen (German).* Forschungsberichte Institut für Industrielle Informationstechnik (IIIT). Karlsruher Institut für Technologie, 2017.

[11] **Warner, J.T.** *The Handbook of Lithium-Ion Battery Pack Design: Chemistry, Components, Types and Terminology.* Elsevier Science, 2015.

[12] **Scrosati, B., Garche, J. and Tillmetz, W.** *Advances in Battery Technologies for Electric Vehicles.* Woodhead Publishing Series in Energy. Elsevier Science, 2015.

[13] **Weicker, P.** *A Systems Approach to Lithium-Ion Battery Management.* Power Engineering. Artech House, 2013.

[14] **Meyer, G.** *Advanced Microsystems for Automotive Applications 2012: Smart Systems for Safe, Sustainable and Networked Vehicles.* Springer Berlin Heidelberg, 2012.

[15] **Andrea, D.** *Battery Management Systems for Large Lithium Ion Battery Packs.* EBL-Schweitzer. Artech House, 2010.

[16] **Muñoz Alvarez, J., Sachenbacher, M., Ostermeier, D., Stadlbauer, H., Hummitzsch, U. and Alexeev, A.** *Electric Vehicle En-*

hanced Range, Lifetime And Safety Through INGenious battery management: D6.1–Analysis of the state of the art on BMS, 2017.

[17] **Yu, Q.Q., Xiong, R., Wang, L.Y. and Lin, C.** *A Comparative Study on Open Circuit Voltage Models for Lithium-ion Batteries. Chinese Journal of Mechanical Engineering*, 31(1):65, 2018.

[18] **Analog Devices**. *isoSPI Isolated Communications Interface.* URL `https://www.analog.com/media/en/technical-documentation/data-sheets/6820fb.pdf`.

[19] **Ferreira, H.C., Lampe, L., Newbury, J. and Swart, T.G.** *Power Line Communications: Theory and Applications for Narrowband and Broadband Communications over Power Lines.* Wiley, 2011.

[20] **Dostert, K.** *Powerline Communications.* Prentice Hall communications engineering and emerging technologies series. Prentice Hall PTR, 2001.

[21] **Huck, T., Schirmer, J., Hogenmuller, T. and Dostert, K.** *Tutorial about the implementation of a vehicular high speed communication system.* In *International Symposium on Power Line Communications and Its Applications*, pages 162–166, 2005.

[22] **Huck, T.** *Integrierte Informations- und Energieübertragung zur Realisierung zeitgesteuerter Bussysteme auf konditionierten Kfz-Bordnetzen (Berichte aus der Kommunikationstechnik (German).* Shaker Verlag, 2006.

[23] **Graf, A.** *The New Automotive 42V PowerNet.* Haus der Technik. Expert-Verlag, 2001.

[24] **Amirshahi, P., Cañete, C., Francisco, J., Dostert, K., Galli, S., Katayama, M. and Kavehrad, M**. *Channel Characterization. Power Line Communications: Theory and Applications for Narrowband and Broadband Communications over Power Lines*, pages 7–126, 2010.

[25] **Dostert, K. and Galli, S.** *Keynote II: modeling of electrical power supply systems as communication channels.* page 137, 2005.

[26] **Gotz, M., Rapp, M. and Dostert, K.** *Power line channel characteristics and their effect on communication system design. Communications Magazine, IEEE*, 42:78–86, 2004.

[27] **Hrasnica, H., Haidine, A. and Lehnert, R.** *Broadband Powerline Communications: Network Design.* Wiley, 2005.

[28] **Ribeiro, M., Lampe, L., Dostert, K. and Hrasnica, H.** *Advanced Signal Processing and Computational Intelligence Techniques for Power Line Communications. EURASIP J. Adv. Sig. Proc.*, 2007, 2007.

[29] **Ardakani, M., Colavolpe, G., Dostert, K., Ferreira, H., Fertonani, D., Swart, T., Tonello, A., Umehara, D. and Vinck, J.** *Digital Transmission Techniques*, pages 195–310. 2010.

[30] **Dostert, K, Girotto, M, Lampe, L., Raheli, R, Rieken, D, Swart, T., Tonello, A., Vinck, J. and Weiss, S.** *Digital Transmission Techniques*, pages 261–385. 2016.

[31] **Hoch, M.** *Comparison of PLC G3 and PRIME.* In *2011 IEEE International Symposium on Power Line Communications and Its Applications (ISPLC)*, pages 165–169, 2011.

[32] **Latchman, H.A., Katar, S., Yonge, L. and Gavette, S.** *Homeplug AV and IEEE 1901: A Handbook for PLC Designers and Users.* Wiley-IEEE Press, 2013.

[33] **Proakis, J.G. and Salehi, M.** *Digital Communications.* McGraw-Hill International Edition. McGraw-Hill, 2008.

[34] **Gallager, R.G.** *Principles of digital Communication.* Cambridge University Press, 2009.

[35] **Goldsmith, A.** *Wireless Communications.* Cambridge University Press, 2005.

[36] **Niknejad, A.M.** *Power Amplifiers for Communications.* URL `http://rfic.eecs.berkeley.edu/ee242/pdf/Module_6_1_PA_Sys.pdf`.

[37] **Tri, T. Ha**. *Theory and Design of Digital Communication Systems*. Cambridge University Press, 2011.

[38] **Michael, R.** *Digital Communications: A Discrete-Time Approach*.

[39] **Kammeyer, K.D.** *Nachrichtenübertragung (German)*. B.G. Teubner Verlag, 2013.

[40] **Mathuranathan, V.** *Simulation of Digital Communication Systems Using Matlab*. eBook, 2013.

[41] **Simon, M.K. and Alouini M.S.** *Digital Communication over Fading Channels A Unified Approach to Performance Analysis*. John Wiley and Sons, 2000.

[42] **Cho, Y.S., Kim, J., Yang, W.Y. and Kang, C.G.** *MIMO-OFDM Wireless Communications with MATLAB*. Wiley, 2010.

[43] **Oppenheim, A.V. and Verghese, G.C.** *Signals, Systems and Inference: Class Notes for 6.011, Introduction to Communication, Control and Signal Processing*. 2010.

[44] **Paret, D.** *FlexRay and its Applications: Real Time Multiplexed Network*. Wiley, 2012.

[45] **IEEE Standards Association**. *IEEE 802.11-2016 - IEEE Standard for Information technology–Telecommunications and information exchange between systems Local and metropolitan area networks–Specific requirements - Part 11: Wireless LAN Medium Access Control (MAC) and Physical Layer (PHY) Specifications*, . URL `http://standards.ieee.org/standard/802_11-2016.html`.

[46] **IEEE Standards Association**. *IEEE 802.11n-2009 - IEEE Standard for Information technology– Local and metropolitan area networks– Specific requirements– Part 11: Wireless LAN Medium Access Control (MAC) and Physical Layer (PHY) Specifications Amendment 5: Enhancements for Higher Throughput*, . URL `http://standards.ieee.org/standard/802_11n-2009.html`.

[47] **Keysight Technologies**. *Impedance Measurement Handbook, A Guide to Measurement Technology and Techniques, 6th Edition - Application Note*. 2016.

[48] **Paul, C.R.** *Introduction to Electromagnetic Compatibility*. Wiley Series in Microwave and Optical Engineering. Wiley, 2006.

[49] **Orfanidis, S.J.** *Electromagnetic Waves and Antennas*. ECE Department Rutgers University, 2016.

[50] **Frickey, D.A.** *Conversions between S, Z, Y, H, ABCD, and T parameters which are valid for complex source and load impedances. IEEE Transactions on Microwave Theory and Techniques*, 42(2):205–211, 1994.

[51] **Smith, J.O.** *Introduction to Digital Filters: With Audio Applications*. Music signal processing series. W3K, 2007.

[52] **Jeffrey, A. and Zwillinger, D.** *18-The z-transform*. In *Table of Integrals, Series, and Products (6th Edition)*, pages 1127–1132. Academic Press, San Diego, 2000.

[53] **Viswanathan, M. and Mathuranathan, V.** *Wireless Communication Systems in MATLAB*. Independently Published, 2018.

[54] **Fiche, G. and Hebuterne, G.** *Mathematics for Engineers*. Wiley, 2008.

[55] **Wesolowski, K.** *Introduction to Digital Communication Systems*. Wiley, 2009.

[56] **Proakis, J.G. and Salehi, M.** *Fundamentals of Communication Systems*. Pearson Education, 2013.

[57] **Herbig, P. and Friedrichs, B.** *Kanalcodierung: Grundlagen und Anwendungen in modernen Kommunikationssystemen (German)*. Information und Kommunikation. Springer Berlin Heidelberg, 2013.

[58] **Moision, B.** *A truncation depth rule of thumb for convolutional codes*. In *2008 Information Theory and Applications Workshop*, pages 555–557, 2008.

Published work

- **Ouannes, I., Nickel, P. and Dostert, K.** *Cell-wise monitoring of Lithium-ion batteries for automotive traction applications by using power line communication: battery modeling and channel characterization.* In *2014 IEEE 18th International Symposium on Power Line Communications and Its Applications*, pages 24–29, 2014.

- **Ouannes, I., Nickel, P., Bernius, J. and Dostert, K.** *Physical Layer Performance Analysis of Power Line Communication (PLC) applied for Cell-Wise Monitoring of Automotive Lithium-Ion Batteries.* In *18th International OFDM Workshop 2014 (InOWo'14)*, pages 1–8. VDE-Verlag, 2014.

- **Ouannes, I., Opalko, O. , Nickel, P. and Dostert, K.** *Monitoring of Lithium-Ion batteries in electric/hybrid vehicles using power line communication.* In *AmE 2015 - Automotive meets Electronics*, pages 24–29. VDE-Verlag, 2014.

Supervised master's theses

- **Bernius, J.** *Evaluation of Orthogonal Frequency Division Multiplexing for Powerline Communication in Lithium-Ion Traction Batteries.* Karlsruhe Institute of Technology (KIT), 2013.

- **Ghobrial, A.** *Design and Implementation of a Software-defined Radio-based Single-Carrier Powerline Communication System for Automotive Battery Management using Matlab/Simulink.* Technical University of Ilmenau, 2015.